UNIVERSITY OF Southampton

University of Southampton Research Repository
ePrints Soton

Copyright © and Moral Rights for this thesis are retained by the author and/or other copyright owners. A copy can be downloaded for personal non-commercial research or study, without prior permission or charge. This thesis cannot be reproduced or quoted extensively from without first obtaining permission in writing from the copyright holder/s. The content must not be changed in any way or sold commercially in any format or medium without the formal permission of the copyright holders.

When referring to this work, full bibliographic details including the author, title, awarding institution and date of the thesis must be given e.g.

AUTHOR (year of submission) "Full thesis title", University of Southampton, name of the University School or Department, PhD Thesis, pagination

http://eprints.soton.ac.uk

UNIVERSITY OF SOUTHAMPTON

FACULTY OF ENGINEERING AND THE ENVIRONMENT

Sustainable Energy Research Group

Grid Generated Turbulence and Actuator Disc Representations of Tidal Turbines

by

Tom Blackmore

Thesis for the degree of Doctor of Philosophy

December 2013

UNIVERSITY OF SOUTHAMPTON

ABSTRACT

FACULTY OF ENGINEERING AND THE ENVIRONMENT
Sustainable Energy Research Group

Doctor of Philosophy

GRID GENERATED TURBULENCE AND ACTUATOR DISC REPRESENTATIONS OF TIDAL TURBINES

by Tom Blackmore

The tidal energy resource in the UK is one of the largest in Europe and can contribute to our ever increasing demand for low carbon energy. The technology is still in its infancy, complicated by the hash marine environment in which the turbines operate. Tidal flows are highly turbulent with a broad range of turbulent length scales and intensities of around 10 %. However, the effects of these highly turbulent flows on turbine performance and wake profile is unclear.

Turbines are commonly represented as actuator discs within numerical simulations and porous disc rotor simulators used to represent turbines in small scale laboratory experiments. This is partly due to the large costs involved with testing a turbine rotor. The aim of this work was to investigate the effects of turbulence on an actuator disc's thrust and wake, as a first step to understanding the interaction of turbulence with a turbine. Grid generated turbulence was used so the turbulence characteristics of the flow could be controlled so the effects of integral length scale and turbulence intensity on an actuator disc could be readily identified.

It was shown how actuator disc RANS simulations are sensitive to the assumed characteristic length scale of the turbulence source within the actuator disc. Due to the limitations of RANS simulations where the characteristic length scale simply changes the dissipation rate and the turbulent eddies are not resolved, further investigation was required to understand the effects of turbulent eddy size on actuator discs. An experimental investigation showed variations in the mean thrust of up to 20 % were possible where turbulence intensity acted to increase the thrust and a strong dependence on the integral length scale to disc diameter ratio was found.

New techniques have been developed to generate turbulence at the inlet and at the actuator disc for Large Eddy Simulations. These techniques are based on the principles of grid generated turbulence and allow the effects of ambient and device generated turbulence to be investigated. It was found that devices generating larger length scales and higher turbulence intensities resulted in a faster wake recovery, analogous to a turbine operating at a lower tip-speed ratio. The effects of ambient turbulence were found to have a significant effect on the wake of an actuator disc. The results show that increasing the turbulence intensity reduces the velocity deficit in the wake but has no effect on the wake width. However, increasing the integral length scale of the ambient flow increases the velocity deficit in the near wake, but results in a lower velocity deficit in the far wake. This is due to the increased mixing with the free stream flow causing the wake width to increase and a faster wake recovery.

This work demonstrates the sensitivity of actuator discs to turbulent inflow conditions highlighting the need to accurately characterise and reproduce the specific turbulence conditions of a site for accurate predictions to be made.

Contents

List of Figures

List of Tables

Declaration of Authorship

I, Tom Blackmore , declare that the thesis entitled *Grid Generated Turbulence and Actuator Disc Representations of Tidal Turbines* and the work presented in the thesis are both my own, and have been generated by me as the result of my own original research. I confirm that:

- this work was done wholly or mainly while in candidature for a research degree at this University;
- where any part of this thesis has previously been submitted for a degree or any other qualification at this University or any other institution, this has been clearly stated;
- where I have consulted the published work of others, this is always clearly attributed;
- where I have quoted from the work of others, the source is always given. With the exception of such quotations, this thesis is entirely my own work;
- I have acknowledged all main sources of help;
- where the thesis is based on work done by myself jointly with others, I have made clear exactly what was done by others and what I have contributed myself;
- parts of this work have been published as described on the following page.

Signed:

Date: 30^{th} September 2013

Publications

- The work in chapter 6 was presented and published in the proceedings of the 9th European Wave and Tidal Energy Conference (Blackmore et al. 2011).
- The work in chapter 7 has been published in the journal Experiments in Fluids (Blackmore, Batten, Műller & Bahaj 2013).
- The work in chapter 8 has been published in the International Journal of Computational Fluid Dynamics (Blackmore, Batten & Bahaj 2013*a*).
- The work in chapter 9 was presented and published in the proceedings of the 10th European Wave and Tidal Energy Conference (Blackmore, Batten & Bahaj 2013*b*).

Acknowledgements

First of all I would like to thank my supervisors Dr. William MJ Batten and Prof. AbuBakr S Bahaj for your guidance, support, inspiration, motivation, immense knowledge, and opportunities to develop my work over the last 3 years. Thanks should also be given to the EPSRC for funding this PhD to make it all possible and the opportunities to develop my knowledge, understanding, and present my research to the tidal engineering community.

A big thanks to Tom Lloyd for organising the 'FOAM parties' where OpenFOAM users at the university can meet and discuss problems, solutions, and all things OpenFOAM or CFD related.

A monumental thanks must go to the crew of building 22 for putting up with me and all the good times we've had together; Brad Keogh, Matt Harrison, Tim Daly, Sid Narayan, Caroline Stuiver, Letisha Rorke, Will Knock, Jim Kerr, Steve Haynes, Natasha Carpenter, Khilan Shah, Andy Stevens, Charles Brent LaFloret,... it's been epic!

And a final humongous thanks to my parents, brother and sister for being there, supporting me, and motivating me though all my studies.

Nomenclature

a	axial induction factor	
A	area	m^2
b	grid bar width	m
B_1	constant	
B_2	constant	
B_R	blockage ratio	
C_k	Kolmogorov universal constant	
C_o	Courant number	
C_P	coefficient of power	
C_{pr}	coefficient of pressure	
C_s	Smagorinsky coefficient	
C_T	coefficient of thrust	
C_μ	constant of proportionality	
d	channel depth	m
Δ	filter size	m
Δt	time step	s
Δx	cell size	m
E	energy	J
ϵ	rate of dissipation of turbulent kinetic energy	$m^2 s^{-3}$
η	Kolmogorov micro scale	m
F	force	N
F_B	momentum sink term	ms^{-2}
g	acceleration due to gravity	ms^{-2}
I	turbulence intensity	
I_R	turbulence intensity of resolved scales	
k	turbulent kinetic energy	m^2/s^2
k_R	resistance coefficient	
κ	wavenumber	m^{-1}
ℓ	integral length scale	m
ℓ_S	Smagorinsky lenghscale	m
L	characteristic length	m
L_s	characteristic length of turbulence source	m

M	grid bar spacing	m
m_a	mass	kg
n_m	growth rate of integral length scales	
n	decay exponent	
ν	kinematic viscosity	m^2/s
ν_R	eddy viscosity of residual motion	m^2/s
ν_T	turbulent viscosity	m^2/s
∇	gradient operator	
P	power	W
p	pressure	Pa
R	two-point correlation coefficient	
r	spacial offset	m
RE	Reynolds number	
RE_T	turbulent Reynolds number	
ρ	fluid density	kg/m^3
s	time offset	s
S_{ij}	rate of strain tensor	s^{-1}
S_t	sample period	s
t	time	s
T	thrust	N
τ	integral time scale	s
τ_{ij}	shear stress	Pa
τ_{ij}^R	shear stress of residual motion	Pa
θ	porosity, open area ratio	
$\dot{u}$	acceleration	m/s^2
u_i	velocity in the i^{th} direction as a function of space and time	m/s
U_i	time averaged velocity in the i^{th} direction as a function of space only	m/s
u_i'	fluctuation of u_i from U_i	m/s
U_D	velocity deficit	
V	volume	m^3
x_o	virtual origin	m
x	x cartesian co-ordinate	m
y	y cartesian co-ordinate	m
z	z cartesian co-ordinate	m
x_o	virtual origin	m
ω	frequency	Hz

Sub- and super-scripts

Φ'	fluctuation of Φ from the mean value
$\bar{\Phi}$	filtered value of Φ

Φ^*	residual component of Φ as a result of filtering
Φ_i	implies the summation of Φ over the co-ordinate directions $i = 1, 2, 3$ for a 3 dimensional case
Φ_∞	free stream value of Φ far upstream
Φ_t	turbine value of Φ
Φ_w	wake value of Φ

Abbreviations

ADCP	Acoustic Doppler Current Profiler
ADV	Acoustic Doppler Velocimeter
CFD	Computational Fluid Dynamics
DNS	Direct Numerical Simulation
LES	Large Eddy Simulation
PISO	Pressure Implicit with Split Operator
RANS	Reynolds Averaged Navier-Stokes
RMS	Root Mean Squared
SIMPLE	Semi-Implicit Pressure Linking Equations
TSR	Tip Speed Ratio

Chapter 1

Introduction

The global economy is reliant on fossil fuels for almost all industries; transportation, electricity generation, production of plastic polymers, heating, fertilisers, manufacture..., to name a few. However, the need for alternatives to fossil fuels can be broken down into three driving factors (MacKay 2009):

1. **Fossil fuels are a finite resource**. Predictions suggest that peak oil has been reached and that the cost of fossil fuels will continue to rise as the remaining resources are used up. This may occur in our lifetime or over a longer period, but the resource will run out one day.

2. **Security of supply**. While fossil fuel resources diminish the remaining reserves are owned by a reducing number of countries. Being reliant on a few sources of fossil fuels leads to uncertainties and huge risk as countries economies become solely dependent on imports.

3. **Climate change**. Although very difficult to prove, it is very likely that the burning of fossil fuels has increased the concentration of greenhouse gases in the atmosphere which is increasing global temperatures. It is estimated that around 74% of the global greenhouse-gas emissions are from the energy sector.

Whatever the motivation, it is clear that the global economy is reliant on fossil fuels and alternative means of energy supply are required. The European Union aims to provide 20% of its energy from renewable sources (wind, solar, hydro, tidal, geothermal and biomass) by 2020. However, most EU countries currently fall short of this target. Significant development is therefore required over the next decade to meet this target.

The UK has invested in offshore wind farms with projected capacity to supply 17% of the UK's electricity by 2020. This still falls short of the EU target and wind intermittency may be a problem.

The UK, being an island separating the North Sea from the Atlantic Ocean, has a raw tidal resource estimated to be $250GW$ (MacKay 2009) that rises and falls twice a day. This resource is substantial and predictable making it an ideal renewable energy supply for the UK. There are two options for harnessing this resource:

1. Tidal barrage - A tidal river or estuary is dammed so a head difference is generated between the high tide and low tide heights which is used for power generation. Tidal barrage projects often suffer from environmental considerations due to loss of habitat in the estuary by the dam.

2. Tidal stream turbines - turbines, similar to wind-turbines, are installed in tidal flows (around headlands or narrows between islands) and convert the kinetic energy of the flow into electrical energy. These devices have a lesser impact on the environment where they are installed.

Black and Veatch (2005) estimate the technically extractable tidal stream resource of the UK to be $\approx 18TWh/y$ which relates to 5% of the UK electricity demand and about half of the EU tidal resource. However, further device development is required before this resource can be exploited commercially. To date the tidal energy industry has only seen single demonstrator devices installed and the technology still in its infancy (Bahaj & Myers 2003, Bahaj 2011). Table 1.1 shows the details of some such devices.

Sites suitable for economical deployment of tidal stream turbines have high kinetic energy densities and hence high tidal velocities ($> 1ms^{-2}$ Bahaj (2013)). The Reynolds Numbers are large (3×10^8 in the Seymour Narrows, Canada (Grant et al. 1961)) resulting in extremely turbulent chaotic flows with a broad range of eddy sizes and intensities of around 10 % (see section 2.5). However, the effect these highly energetic turbulent flows have on the performance and wake of a tidal turbine is unclear.

Experimental investigations using model turbines are very expensive due to the high cost of one-off manufacture and large test facilities required. Numerical models with actuator discs are commonly used to represent turbines within simulations (Batten et al. 2013) to investigate turbine wakes at much reduced cost. An actuator disc accounts for the energy extraction of a turbine by applying a momentum sink to the governing flow equations within the volume occupied by a turbine rotor. This method allows simulations of single devices and multiple device arrays to be performed with modest computational requirements. However, the inflow of these simulations is often low or even zero turbulence (e.g. Masters et al. (2013)). Similarly, turbines are often simulated in small scale laboratory experiments using porous disc rotor simulators. A porous disc dissipates energy from the flow through the generation of small scale turbulence equivalent to the energy extracted by a turbine (Myers & Bahaj 2010). Good agreement is found between rotors and porous discs in the far wake. Experiments performed under

Table 1.1: Installed tidal stream devices

Tidal Device	**Power** (MW)	**Location**
MCT's Seagen	1.2	Strangford Lough since 2008
OpenHydro	0.25-1	250kW at EMEC since 2006; 1MW at FORCE in 2009; currently installing 4 devices with EDF in Brittany
Atlantis Resources Corporation's AR1000	1	At EMEC since 2010
Andritz Hydro Hammerfest's HS1000	1	At EMEC since 2011
ORPC's TidGen system	0.9 (5 devices)	Currently being installed in Maine
Scotrenewables' SR250	0.25	EMEC since 2011
Hyundai Heavy Industries	0.5	Uldolmok, Korea
Tidal Generation Ltd	0.5	EMEC since 2010
Verdant Power's RITE project	1 (30 devices)	Currently increasing from 6 to 30 devices, NY
Upcoming FORCE deployments:		MCT's Seagen U Atlantis' AR1000 (1MW) Alstom's Beluga 9 (1MW)
Upcoming EMEC deployments:		Voith Hydro (1MW) Kawasaki Heavy Industries Bluewater Energy Services

laboratory conditions will often have low levels of turbulence, which differ's from that of a tidal site (e.g. experiments performed in a towing tank have a zero turbulence inflow!) and the turbulence conditions are not often fully reported. It is therefore important to understand the influence of turbulence on the wake and thrust of an actuator disc to first identify if there is a sensitivity of the disc to turbulence characteristics, and secondly to understand these effects to improve the predictions and potential influence of turbulence on a turbine installed in a tidal flow. Initial review of the prior art suggests variations in drag force of bluff bodies up to 20 % are possible when installed in turbulent flows with different length scales and intensities (Bearman & Morel 1983). Significant discrepancies are therefore possible in predictions of turbine performance and wake profile when the turbulence characteristics are not considered. A 20 % variation in performance of an array could be the difference between economic success and failure of the project. This thesis is concerned with understanding the effects of turbulence intensity and integral length scale on the thrust loads and wake profile of an actuator disc using small scale laboratory experiments and numerical simulation.

1.1 Report structure

This report presents the background theory, literature review, and results for an investigation on the effects of turbulence on actuator discs. The work is a mixture of numerical simulations and small scale laboratory experiments. The report structure is as follows:

1. **Introduction** - General introduction to report topic.

2. **Turbulence and expected scales** - This chapter first presents some background theory required for the analysis and understanding of turbulent flows. The final two sections present a review of grid generated turbulence and the turbulent characteristics in a tidal flow.

3. **CFD techniques for modelling tidal turbines** - The first two sections of this chapter present some background theory on computational fluid dynamics (CFD) and turbulence models used. Methods for modelling turbine rotors in CFD simulations are presented and a review of the methods used to generate turbulence in Large Eddy Simulations (LES) and the current state-of-the-art rotor modelling within CFD is presented.

4. **Influence of turbulence on discs and rotors** - This chapter reviews the current state-of-the-art on the effects of turbulence on tidal stream turbine rotors, porous disc rotor simulators and solid discs. The effects on the mean thrust force are first discussed and then the effects of turbulence on the wake are considered.

5. **Problem statement** - This chapter defines the aims and objectives of this work with a brief summary of the review from the previous chapters.

6. **RANS modelling of actuator discs** - This chapter presents an investigation on the sensitivity of actuator disc RANS simulations to characteristic length scale assumptions. This work highlights the importance of turbulent scale as well as intensity and demonstrated the need for further work with LES models to resolve the structure of the turbulent eddies due to the limitations of RANS models.

7. **Influence of turbulence on the thrust of turbine simulators** - This chapter presents an experimental investigation on the effects of turbulence on the thrust of solid and porous discs. This work demonstrates that both turbulence intensity and integral length scale significantly affect the thrust of solid and porous discs with variations in thrust up to 20 %.

8. **Inlet grid generated turbulence for Large-Eddy Simulations** - This chapter presents the development of a new technique for generating turbulence in LES models based on grid generated turbulence and referred to as a *gridInlet*. Results are presented on the influence of mesh characteristics and domain boundaries on

the development of turbulence and comparisons made to grid generated turbulence in a flume from the previous chapter. This work demonstrates the ability of this newly developed method to generate approximately isotropic turbulence with different integral length scales and intensities.

9. **Turbulence generation in LES approximations of tidal turbines** - This chapter presents a new method of generating turbulence in actuator disc LES models to represent the turbulence generated by the device. It is an extension of the gridInlet technique so the turbulence characteristics of the generated turbulence may be controlled. It was shown that a device generating larger length scales and higher intensities results in a faster wake recovery, analogous to a turbine operating at a lower tip speed ratio (TSR).

10. **Influence of turbulence on the wake of an actuator disc** - This final results chapter combines the techniques developed in the previous two chapters to investigate the effects of grid generated turbulence with different turbulence intensities and integral length scales on the wake of an actuator disc. Comparisons were made to the experimental study of chapter 7 with anisotropic turbulence and against published experimental studies to demonstrate the effectiveness of the method.

11. **Overall conclusions and engineering application** - This chapter first summarises the new findings from the five results chapters, 6-10. The implications of these results are discussed in relation to their engineering application to the tidal energy industry. Future work is also considered that would lead on to further the understanding on the effects of turbulence on tidal turbines.

Chapter 2

Turbulence and expected scales

This chapter first presents the background theory required for the analysis of turbulent flows. Following this the method of generating turbulence with a grid for laboratory experiments and the turbulent characteristics of a tidal flow are discussed.

2.1 The Governing Equations of Fluid motion

This section presents the Navier-Stokes equation which governs almost all fluid flows. The derivation is based on the application of three physical principles and will be considered for incompressible flows. For further reading refer to Davidson (2004) and Pope (2000).

1. Newton's second law:

$$F = m\dot{u}. \tag{2.1}$$

   where F = force; m = mass; and $\dot{u}$ = acceleration.

2. Newton's law of viscosity:

$$\tau_{ij} = \rho\nu \left\{ \frac{\partial u_i}{\partial x_j} + \frac{\partial u_j}{\partial x_i} \right\}. \tag{2.2}$$

   where τ_{ij} = shear stress tensor; ρ = density; ν = kinematic viscosity; u_i = velocity in i^{th} direction; $x_i = i^{th}$ direction.

3. Mass conservation:

$$\frac{\partial u_i}{\partial x_i} = 0. \tag{2.3}$$

The resulting partial differential equation appears quite simple at first glance, but due to non-linearities results in complex phenomena and instabilities, that is turbulence. The chaotic nature of turbulence will be discussed later in this chapter.

2.1.1 The Navier-Stokes Equation

Application of Newtons second law (2.1) to a fluid element, as shown in figure 2.1, of volume δV results in the following expression,

$$(\rho \delta V)\frac{Du_i}{Dt} = -\left(\frac{\partial p}{\partial x_j}\right)\delta V + viscous forces. \tag{2.4}$$

Where δV = element volume; u_i = velocity in all directions; t = time; p = pressure;

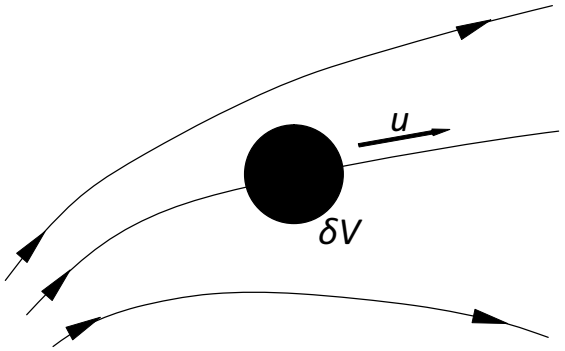

Figure 2.1: Fluid element of volume δV (Davidson 2004).

On the left hand side the element mass, $(m = \rho \delta V)$, multiplied by the particle acceleration, Du_i/Dt, is equal to the net force generated from the pressure plus any viscous forces acting on the element. The viscous forces arise from imbalances in shear between opposite sides of the element as shown in 2.2. The viscous forces, f_i, acting on the element are:

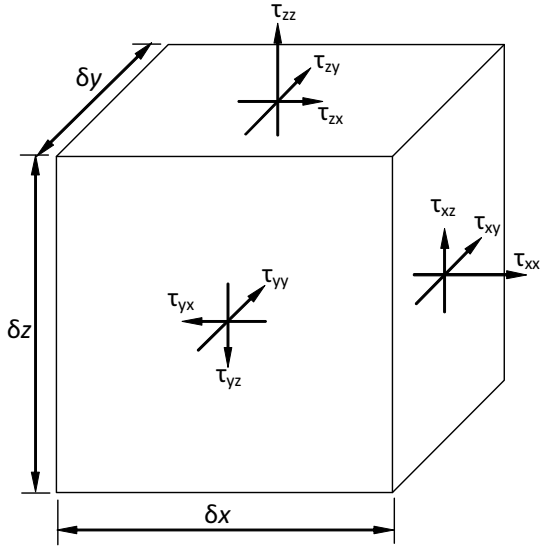

Figure 2.2: Stresses acting on a fluid element of volume δV (Davidson 2004).

$$f_i = \frac{\partial \tau_{ji}}{\partial x_j} \delta V. \tag{2.5}$$

Where f_i = viscous forces in i^{th} direction.

Substitution of equation (2.5) into equation 2.4 yields.

$$\rho \frac{Du_i}{Dt} = -\frac{\partial p}{\partial x_j} + \frac{\partial \tau_{ij}}{\partial x_j}. \tag{2.6}$$

It is now necessary to introduce Newtons law of viscosity (2.2), which is applicable to most fluids. This relates the stress tensor, τ_{ij}, to the rate of deformation of the fluid element. Introducing the strain-rate tensor, S_{ij}, as

$$S_{ij} = \frac{1}{2}\left[\frac{\partial u_i}{\partial x_j} + \frac{\partial u_j}{\partial x_i}\right], \tag{2.7}$$

yields a compact form of (2.2), $\tau_{ij} = 2\rho\nu S_{ij}$, which can be substituted into (2.6). After rearrangement yields

$$\frac{Du_i}{Dt} = -\frac{1}{\rho}\frac{\partial p}{\partial x_j} + \frac{\partial}{\partial x_j}\left(\nu \frac{\partial u_i}{\partial x_j}\right). \tag{2.8}$$

The acceleration term, Du_i/Dt, is also known as the convective derivative as is the rate of change of velocity of the fluid element as it moves through the domain. This is not the same as the partial derivative, $\partial/\partial t$, which is the rate of change at a fixed point in space. Application of the chain rule to the convective derivative yields an explicit expression for the acceleration term,

$$\frac{Du_i}{Dt} = \frac{\partial u_i}{\partial t} + u_j \frac{\partial u_i}{\partial x_j}. \tag{2.9}$$

Equating (2.9) with (2.8) yields the Navier-Stokes equation,

$$\underbrace{\frac{\partial u_i}{\partial t}}_{transient} + \underbrace{u_j \frac{\partial u_i}{\partial x_j}}_{convection} = \underbrace{-\frac{1}{\rho}\frac{\partial p}{\partial x_j}}_{pressure} + \underbrace{\frac{\partial}{\partial x_j}\left(\nu \frac{\partial u_i}{\partial x_j}\right)}_{viscosity}. \tag{2.10}$$

For an incompressible flow, as considered, it is the nonlinear *convective* term that introduces the complex phenomenon of turbulence, while the *viscous* term acts to diffuse momentum eventually destroying turbulence driven by the fluid viscosity. It is not currently possible to solve the Navier-Stokes equation exactly, but it is possible to obtain solutions using numerical finite element discretisation methods. These methods come

under the general name of Computational Fluid Dynamics (CFD) and are discussed in chapter 3.

2.2 Turbulence

The governing Navier-Stokes equation has been presented and the nonlinear *convective* term responsible for the complex chaotic behavior of turbulence identified. The following sections describe how turbulence manifests itself and how it effects the mean flow field complicating the design and performance of certain devices; sometimes beneficial, sometimes detrimental to performance.

2.2.1 The Basics

There are very few, if any, cases in nature where turbulence is not present in fluid flows. From the large scale meteorological movements of weather systems in the atmosphere to the smaller scale movements of the air we breathe, turbulence is present. Turbulence can be thought of as random fluctuations superimposed on a mean flow created through gradients in velocity, shear, and eventually dissipated as heat from molecular viscosity. Small changes or perturbations are amplified resulting in large changes to the fluid motion. Turbulence is therefore unpredictable, or chaotic, and is impossible to determine exact solutions for the fluid motion. However, the statistical properties of turbulence can be measured and repeated and their effects on a flow field analysed (Davidson 2004). Consider the flow over a cylinder where the velocity is measured as a function of time at a fixed location downstream as shown in figure 2.3. If the experiment is repeated and $u(x_o, t)$ measured a second time the two velocity traces will be different as can be seen in figure 2.4. $u(x_o, t)$ is unpredictable and chaotic due to the effects of turbulence. Any small change in initial conditions will be amplified and result in large differences between velocity traces of the two experiments. However, the time averaged velocity $U(x_o)$ and even $\langle u^2 \rangle$ for the two experiments will be the same, provided the sample period is sufficiently long. Therefore the statistical properties of a turbulent flow can be determined, and repeated, but not the exact fluid motion of a particle in a flow.

If the fluid viscosity is sufficiently high and the velocity low, the resulting flow tends to be smooth and regular. This is known as laminar flow. However, as the fluid speed increases or viscosity reduced the flow starts to become chaotic and is described as turbulent. In 1883 Reynold's investigated the flow along a smooth, straight pipe. He introduced the non-dimensional Reynolds number $Re = UL/\nu$, where U is the mean velocity down the pipe, L is the characteristic length (pipe diameter), and ν the kinematic fluid viscosity. This is essentially the ratio of inertial to viscous forces. For large Re the effects of viscous forces are low allowing turbulence to develop. For low Re the viscous forces

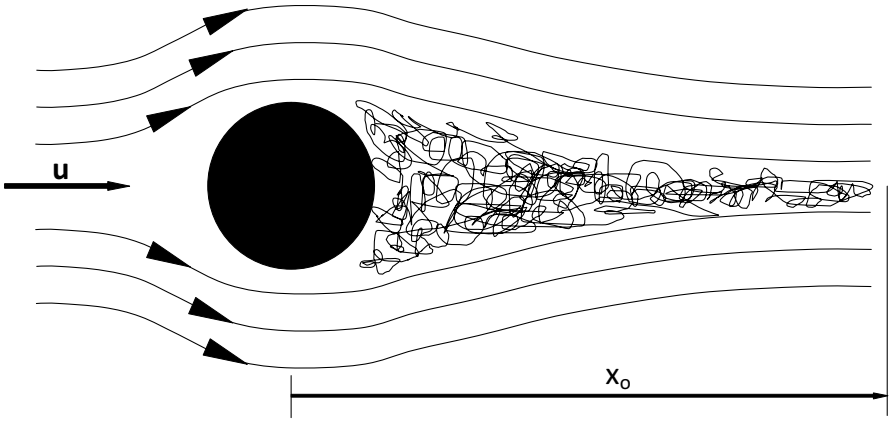

Figure 2.3: Flow over a cylinder adapted from Davidson (2004).

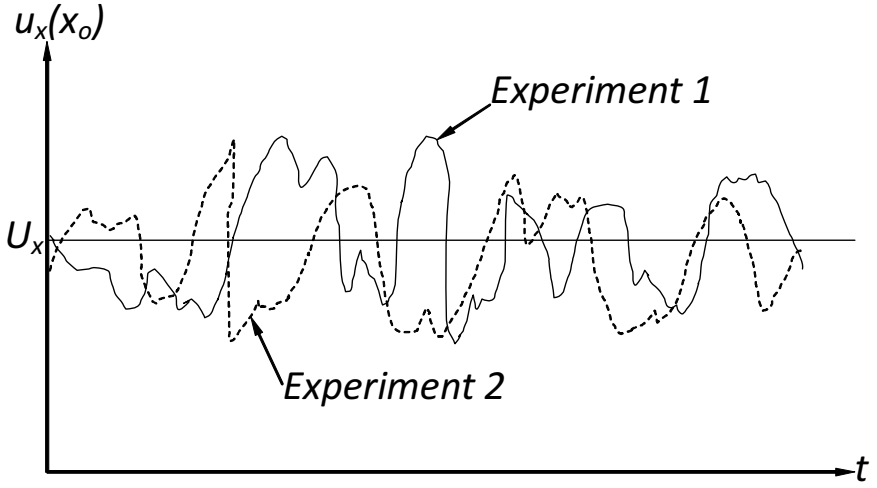

Figure 2.4: Comparison of two experiments measuring velocity on the turbulent wake behind a cylinder adapted from Davidson (2004).

are significant preventing the development of turbulence. Reynolds also found that by carefully controlling the inlet conditions to the pipe, minimising disturbances, laminar flow could be maintained at high Reynolds numbers where turbulence would normally occur.

Although Reynolds investigated pipe flow his findings relate to other external flows. He showed that turbulence is the norm for high Reynolds number flows where the influence of viscosity is small compared to inertia effects. He also showed that the inlet conditions have a significant effect on the flow that develops. This is particularly important for specifying inlet conditions to numerical simulations or the inlet conditions in laboratory tests of devices designed for deployment in natural flows. For almost all natural fluids, such as air and water, viscosity is very low making laminar flow the exception and turbulence the norm.

Due to the complexities and wide range of conditions that are considered to be *turbulent*, it is difficult to formulate a formal definition (Davidson 2004, Pope 2000). However,

turbulence is:

- Random fluctuations in time and highly disordered in space over a range of scales.
- Unpredictable and chaotic so that small perturbations to initial conditions are amplified resulting in large changes to the flow. i.e. It is impossible to find a deterministic prediction of a turbulent flow.
- Able to mix any transported quantity more rapidly than molecular diffusion alone - this includes momentum.

The first point mentions scales. Turbulence is not only a random fluctuation, but also has structure. The largest turbulent eddies will have a size comparable to a characteristic geometric length of the mean flow. For Reynolds experiments in a pipe this characteristic length is the pipe diameter. The turbulent flow will also contain many eddies smaller than this characteristic length right down to the smallest eddies that will be less than 1 mm in size. For fully developed turbulence the flow will contain a broad spectrum of scales. This idea leads to the concept of the *energy cascade* as shown graphically in figure 2.5.

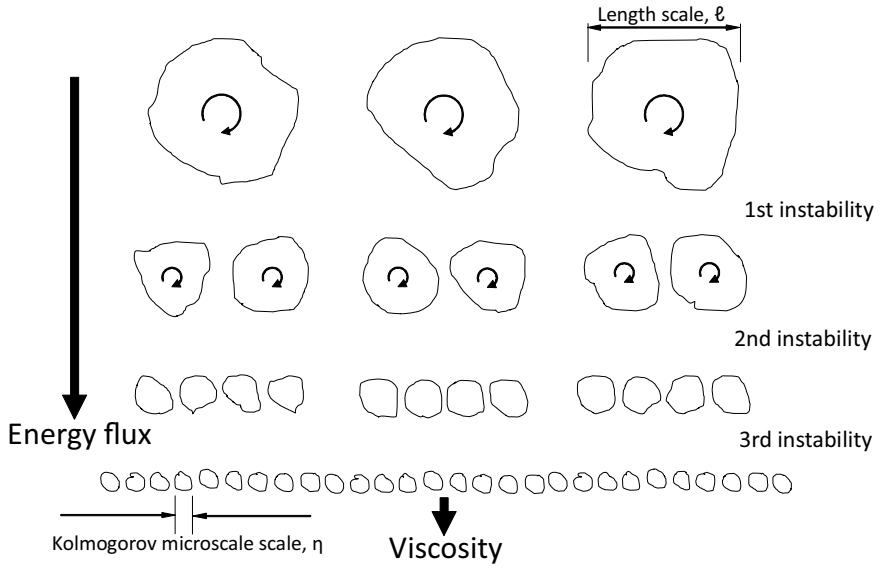

Figure 2.5: Cascade of energy from large scale structures to progressively smaller structures until the dissipation of energy from viscous effects (adapted from Davidson (2004)).

The time varying velocity measured at different locations in space may be split into the time-averaged component and the fluctuating component at each location, represented by U and u' respectively.

$$u(x,t) = U(x) + u'(x,t) \tag{2.11}$$

Here $U(x)$ is a smooth function of position, while $u'(x,t)$ contains the random fluctuations from a range of turbulent eddy sizes. Consider a turbulent flow where the turbulent Reynolds number is large; $Re_T = |u'|l/\nu$ where l the size of the turbulent eddy. The large-scale eddies are generated from instabilities in the mean flow, which themselves have instabilities breaking them down into smaller eddies, see figure 2.5. This process then repeats creating smaller and smaller eddies. As Re_T is large the viscous forces are small and this process is driven by inertial forces. However, when the eddies become sufficiently small such that $Re_T = |u'|l/\nu$ is of order unity, the viscous forces become significant. Dissipation of turbulent kinetic energy occurs through the creation of heat due to friction. Of particular interest is the rate at which turbulent energy is converted, or dissipated, as heat. Considering the fluid blob from earlier with shear stresses, τ_{ij}, acting on its sides, the rate of work done by these stresses on the fluid is:

$$\dot{W} = \int \frac{\partial}{\partial x_j} \left[u_i \tau_{ij}\right] dV. \tag{2.12}$$

Or per unit volume,

$$\frac{\partial}{\partial x_j} \left[u_i \tau_{ij}\right] = \frac{\partial \tau_{ij}}{\partial x_j} u_i + \tau_{ij} \frac{\partial u_i}{\partial x_j}. \tag{2.13}$$

The first term on the right hand side of this equation represents the rate of working of the net viscous forces acting on the element, or the change of turbulent kinetic energy of the fluid. The second term must therefore represent the change of internal, or thermal energy of the fluid. This term is known as the dissipation rate, ϵ, and may be simplified,

$$\tau_{ij} \frac{\partial u_i}{\partial x_j} = \frac{1}{2} \left[\tau_{ij} + \tau_{ji}\right] \frac{\partial u_i}{\partial x_j} = \frac{1}{2} \left[\tau_{ij} \frac{\partial u_i}{\partial x_j} + \tau_{ij} \frac{\partial u_j}{\partial x_i}\right] = \tau_{ij} S_{ij}. \tag{2.14}$$

The rate of dissipation per unit mass is therefore:

$$\epsilon = \frac{\tau_{ij} S_{ij}}{\rho} = 2\nu S_{ij} S_{ij}. \tag{2.15}$$

The dissipation will therefore be greatest where there are large gradients in velocity, and hence large shear stress. This is the basis behind the theory of the energy cascade that the dissipation of turbulent kinetic energy is predominantly at the smallest eddies driven by viscosity; while inertial forces are responsible for breaking up the larger eddies. Energy is therefore continually transferred from the largest to progressively smaller eddies until it is eventually dissipated as heat through the effects of viscosity. The smallest turbulent structures in a flow are known as the *Kolmogorov microscales* with length scale η, while the largest turbulent structures have length scale ℓ and known as

the integral length scale. It is worth noting that as the Re based on the integral length scale increases, the size of the Kolmogorov microscales decreases. This further broadens the spectrum of scales significantly increasing the computational cost of simulating high Re flows.

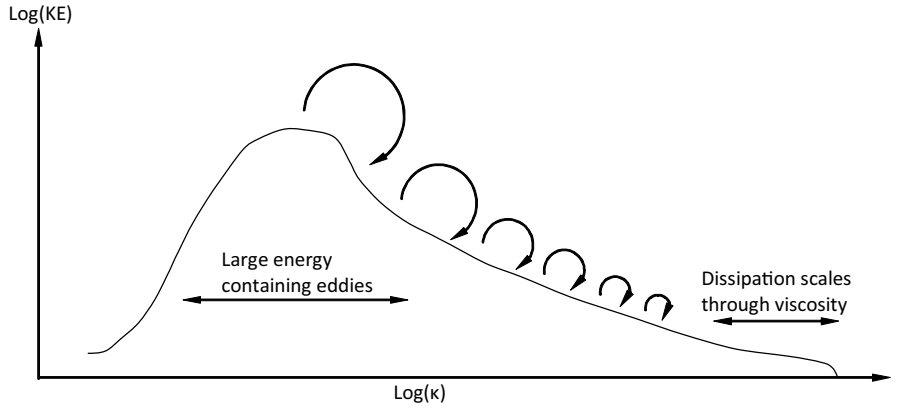

Figure 2.6: Cascade of energy from large to small scales (adapted from Pope (2000)).

Figure 2.6 shows a logarithmic plot of turbulent kinetic energy, k, against wavenumber, κ; where $k = 1/2\left\langle u'^2 \right\rangle$ and κ is proportional to the inverse of eddy size. This plot displays the distribution of energy for the range of scales present in a turbulent flow and its significance discussed in section 2.3.2. For further reading on turbulence refer to Pope (2000) and Davidson (2004).

2.2.2 The closure problem of turbulence

The governing Navier-Stokes equation and turbulence have been discussed. The question then arises, can the Navier-Stokes equation be used to analyse turbulence and predict flow fields for engineering applications? Physical experiments can be performed but at relatively high cost and time. With developments in computer performance it is becoming ever more attractive to run computer simulations which allow predictions to be made over a wide range of conditions at comparatively low cost. However, there is still a problem with how to solve the Navier-Stokes equation.

It is possible to obtain a solution for $u(x,t)$ through numerical integration but requires significant computational power, even for small problems. The method is known as direct numerical simulation (DNS), and the resulting data may be analysed to find other statistical properties such as $U(x)$ and $\left\langle u'(x)^2 \right\rangle$. It is these statistical properties that are important for the analysis of turbulence, as it is these properties are reproducible; unlike the chaotic nature of $u(x,t)$. However, forming equations of similar form to equation 2.10, but for $U(x)$, $\left\langle u'(x)^2 \right\rangle$, or other statistical properties introduces further unknown quantities. The resulting system of equations are therefore *not closed* and cannot be

solved as there are more unknowns than equations. This is known as the *closure problem of turbulence* and is caused by the nonlinear term in the Navier-Stokes equation (2.10). Different methodologies for modelling turbulence to obtain solutions for $u(x,t)$ using modest computational resource are discussed in chapter 3 and come under the general name of *Computational Fluid Dynamics* (CFD).

2.3 Turbulence intensities and scales

As the mean velocity fluctuations are repeatable for a turbulent flow, turbulence is often reported as a mean *turbulence intensity*.

Turbulence intensity is the ratio of the root-mean-square of the velocity fluctuations to the mean velocity. It is often expressed as a percentage fluctuation of the mean flow as shown in equation 2.16.

$$I \equiv \frac{\left\langle u'^2 \right\rangle}{U}. \tag{2.16}$$

where I = turbulence intensity; $\left\langle u^2 \right\rangle$ = root mean squared of velocity fluctuation; U = time averaged velocity.

While the turbulence intensity indicates the strength of turbulence in a flow it gives no indication of the structure or size of the turbulent eddies present. The following sections present statistical quantities that can be used to express the turbulent structure.

2.3.1 Two-point correlation and the integral length scale

As previously discussed turbulence has structure and contains a broad range of eddy sizes. To enable the comparison and analysis of turbulent flows it is necessary to provide information on these structures. One method of obtaining information on spatial structure is the two-point, one time autocovariance (Pope 2000),

$$R_{ii}(r) \equiv \left\langle u_i'(x) u_i'(x+r) \right\rangle. \tag{2.17}$$

Where $R_{ii}(r)$ = two point autocovariance; r = offset from $x = 0$.

From this it is possible to define the integral length scale, which can be thought of as the dominant eddy size containing the largest proportion of turbulent energy. The integral length scale is the integral of the normalised autocovariance,

$$\ell_i \equiv \frac{1}{R_{ii}(0)} \int_0^\infty R_{ii}(r)dr. \tag{2.18}$$

Where ℓ = integral length scale. The integral length scale is a commonly used to describe and compare the structure of turbulent flows. As mentioned before it is the large energy containing eddies that will have the largest effect on the flow, therefore this parameter is particularly important in assessing the effects of different turbulent flows.

2.3.2 Energy Spectra in wavenumber space

The integral length scale provides information on the dominant energy containing eddy size. However, there are a broad range of eddy sizes which make up a turbulent flow. Energy spectra are used to present information on the complete range of scales. For homogeneous turbulence the two-point correlation will be independent of position and can be re-expressed in terms of a *wavenumber spectrum* using Fourier analysis. Wavenumber, κ, can be related to eddy size using the relation $\ell = 2\pi/|\kappa|$.

The energy spectrum is defined as the Fourier transform of the autocorrelation function,

$$E_{ii}(\kappa) \equiv \frac{2}{\pi} \int_0^\infty R_{ii}(r)cos(\kappa r)dr, \tag{2.19}$$

with the corresponding inverse,

$$R_{ii}(r) \equiv \frac{1}{2} \int_0^\infty E_{ii}(\kappa)cos(\kappa r)d\kappa. \tag{2.20}$$

Integration over all wavenumbers yields the total turbulent kinetic energy,

$$\int_0^\infty E(\kappa, t)d\kappa = \frac{1}{2}R_{ii}(0) = \frac{1}{2}\left\langle u_i' u_i' \right\rangle = k. \tag{2.21}$$

The energy spectra therefore represents the contribution to the total turbulent kinetic energy from all modes κ (Pope 2000).

Kolmogorov

In 1941 Kolmogorov presented his theory of a *universal equilibrium range* which has been found to compare well with a wide range of experimental data. His theory applies to the range of eddies for which $r << \ell$ and hypothesised that in this range the eddies are *statistically isotropic* (known as local isotropy), in *statistical equilibrium*, and of *universal form*. Based on the idea of the energy cascade, eddies of size $r << \ell$ are offspring of

larger eddies, which in turn are the offspring of even larger eddies. It is plausible that the smaller eddies do not retain information from the largest eddies and unlikely to be effected by the instantaneous effects of the large scale structures as they would simply advect the smaller scales around. Also the timescale of these small eddies will be fast compared to the slowly evolving large scales.

In most *real* flows the large scales will be anisotropic and statistically unsteady. However, as eddies of size $r << \ell$ do not feel the effects of the large slowly evolving structures, he argued that the small scales do not feel the large-scale anisotropy or overall time-dependence of the flow. Therefore they are in approximate statistical equilibrium and approximately isotropic - this is what Kolmogorov termed locally isotropic and in statistical equilibrium. The range for which $r << \ell$ is known as the *universal equilibrium range*. He showed using dimensional arguments that the turbulent kinetic energy in this range was dependent only upon the rate of energy dissipation, ϵ, of the small scales and the wavenumber, κ (Pope 2000).

$$k(\kappa) = C_k \epsilon^{2/3} \kappa^{-5/3}. \tag{2.22}$$

where C_k is a universal constant. Equation (2.22) is known as Kolmogorov's five-thirds law which describes the range of turbulence which is independent of both the large scales and molecular viscosity.

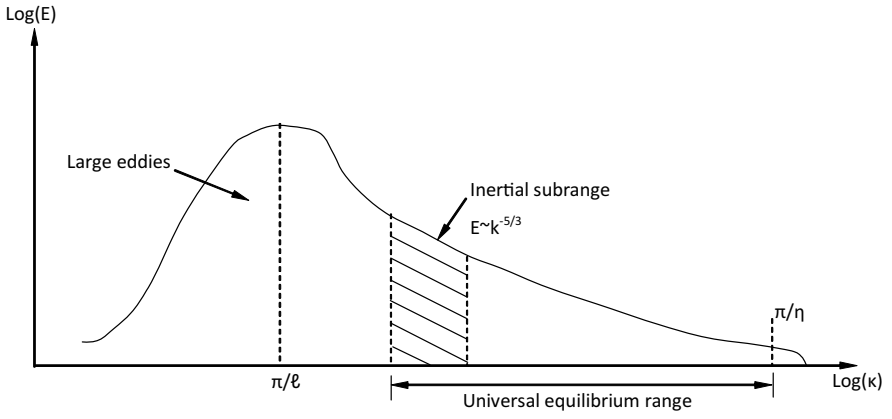

Figure 2.7: The energy spectrum - a logarithmic plot of turbulent kinetic energy against wavenumber (adapted from Davidson (2004)).

Figure 2.7 shows a typical energy spectrum which can be subdivided into three sections.

- The large energy containing, or integral scales. These eddies contain the largest proportion of turbulent kinetic energy and are generally the scales at which turbulent energy is introduced to the flow.

- The second section is known as the inertial subrange. These scales obey Kolmogorov's law so are independent of the large scales and molecular viscosity. Little turbulent kinetic energy is contained or transferred in these scales, they simply transfer energy from the large to the small scales.
- The final section is the dissipative range where the scales are so small that viscous effects dissipate the turbulent kinetic energy as heat. It is these scales where most of the dissipation occurs. The universal equilibrium range is the combination of the inertial subrange and dissipation range. Here the turbulence is considered to be fully developed and free from the influence of the large forcing scales.

Although figure 2.7 is considered a typical energy spectrum it is possible that the inertial subrange will not exist if energy is added at scales close to the dissipative scales, or Re is too low (Davidson 2004).

2.3.3 The frequency domain

It has previously been discussed how turbulence has structure and contains a broad spectrum of eddy sizes. The structures can be viewed experimentally using flow visualisation techniques, but these methods are usually difficult to implement and not practical for many flow scenarios, especially many engineering applications. It has also been discussed how two-point correlations can be used to extract spatial information. However, it is not feasible to obtain sufficiently high resolution, for all r, data experimentally. It is therefore common to measure a time series of velocity at a fixed position in space with hot wire anemometers, Acoustic Doppler Velocimeters, Laser Doppler Anemometry, ...etc, but the measurement method is not important. The main point to note is that $u(t)$ is obtained from which the mean velocity and mean fluctuation can be calculated and compared. However, these quantities do not provide any information on the structure of turbulence and when plotted the trace appears chaotic. Contained in the apparent chaos are a range of structures, each creating fluctuations of certain frequency relating to a certain wavenumber. It is therefore possible to extract information on the structure of turbulence from $u(t)$.

Similar to the two-point correlation, for a statistically stationary flow the autocovarience may be calculated as:

$$R(s) \equiv \left\langle u'(t)u'(t+s) \right\rangle , \tag{2.23}$$

which when normalised with $R(0)$ becomes the autocorrelation function

$$\rho(s) \equiv \frac{\langle u'(t)u'(t+s) \rangle}{\langle u'(t)u'(t) \rangle}, \tag{2.24}$$

where s is the lag time. It should be noted that the mean U, variance $\overline{u'^2}$, autocovarience $R(s)$, and autocorrelation $\rho(s)$ are all independent of time as the flow is statistically stationary. $\rho(s)$ is the correlation coefficient of $u(t)$ at times t and $t+s$. It therefore has the properties $\rho(0) = 1$, $|\rho(s)| \leq 1$ and is an even function. For turbulent flows the correlation usually decreases with increasing lag time s (Pope 2000). An *integral time scale* may be defined as

$$\tau \equiv \int_0^\infty \rho(s) ds. \tag{2.25}$$

The integral time scale may be related to the integral length scale using Taylors hypothesis (Pope 2000),

$$\ell \approx \tau.U. \tag{2.26}$$

This relation has been found to have good accuracy for $u'/U << 1$ and allows spatial information to be inferred from temporal data.

Similar to the wavenumber spectrum an energy frequency spectrum may be obtained using Fourier transforms. As the autocovarience is an even function this may be expressed as a cosine transform pair

$$E(\omega) \equiv \frac{2}{\pi} \int_0^\infty R(s) cos(\omega s) ds, \tag{2.27}$$

$$R(s) \equiv \frac{1}{2} \int_0^\infty E(\omega) cos(\omega s) d\omega. \tag{2.28}$$

Where ω = frequency. Taking the integral over the frequency range $\omega_a < \omega_b$ returns the contribution to the variance $\langle u'(t)u'(t) \rangle$ of all modes in the frequency range. The total variance, or twice the total turbulent kinetic energy, is therefore

$$R(0) = \langle u'(t)u'(t) \rangle = \int_0^\infty E(\omega) d\omega = 2k. \tag{2.29}$$

As seen for the energy spectra in wavenumber space, the energy spectrum in the frequency domain also contains a $-5/3$ slope in the inertial subrange, when plotted logarithmically (Pope 2000).

All energy spectra and integral length scales presented in the results section are calculated using time series data and plotted in the frequency domain.

2.4 Grid generated turbulence

To generate turbulence it is necessary to first generate vorticity by generating velocity gradients, or shear, through interaction with a solid. Experimentally this is most commonly achieved using a grid. Figure 2.8 shows a typical grid with parameters of bar width, b, and bar spacing, M, and porosity, θ defined by equation 2.30.

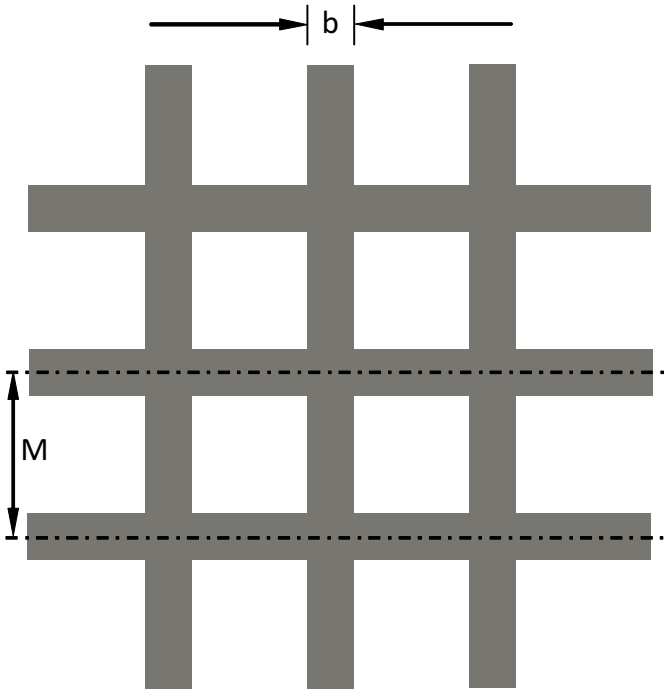

Figure 2.8: Grid structure for the generation of isotropic turbulence.

$$\theta = \frac{Open\ Area}{Total\ Area} = \frac{(M-b)^2}{M^2}. \tag{2.30}$$

Downstream of the grid a discrete set of vortices are shed from the grid bars which soon become turbulent and interact. Initially the turbulent energy will be contained in length scales proportional to the bar size. As the turbulence develops this energy is redistributed to smaller scales of turbulence through the energy cascade. At some distance downstream a field of fully developed turbulence is generated that contains the full range of scales down to the Kolmogorov microscale. As there is no further production of turbulence the turbulent kinetic energy decays, and is known as freely decaying turbulence. Hence, the turbulent intensity decreases with distance from the inlet as described by equation 2.31, (Mohamed & LaRue 1990).

$$I^2 = B_1 \left(\frac{x - x_o}{M} \right)^{-n}. \tag{2.31}$$

Table 2.1: Integral length scales 40 x/M downstream of grid.

M (mm)	ℓ/M	Author
40	0.60	Krogstad & Davidson (2009)
25.4	0.47	Mohamed & LaRue (1990)
50.8	0.53	Mohamed & LaRue (1990)
40	0.60	Krogstad & Davidson (2011)
37	0.64	Krogstad & Davidson (2011)
51	0.46	Krogstad & Davidson (2011)

Where B_1 = constant dependent on grid geometry and Reynolds number; x = distance downstream of grid; x_o = virtual origin used to account for the fact that the origin of turbulent velocity fluctuations may not coincide with the grid location; n = turbulence decay exponent. Mohamed & LaRue (1990) investigated the decay power law of grid generated turbulence through their own wind tunnel experiments and reviewing previous literature. They found that for most cases a value of $n = 1.3$ with $x_o = 0$ was found.

Krogstad & Davidson (2009) showed that the length scales generated by a grid grow with distance downstream of the grid with exponent $n_m = 0.36$.

$$\ell = B_2 \left(\frac{x - x_o}{M} \right)^{n_m} \tag{2.32}$$

where B_2 is a constant. Comparison of the length scale at 40 x/M from Mohamed & LaRue (1990), Krogstad & Davidson (2009), and Krogstad & Davidson (2011) show that the length scales developed varies between different grids as shown in table 2.1. However the average length scale to grid spacing was found to be $\ell/M = 0.549 \pm 0.09$. By $x/M = 200$, ℓ/M had grown to 1 (Krogstad & Davidson 2009). However, the turbulence intensity this far downstream is very low, less than 1 %, which is less than expected in a tidal flow. Close to the grid where the turbulence intensities are high it is likely that the length scales generated will be approximately half the grid spacing.

2.4.1 Summary

Turbulence can be generated behind a grid structure for experimental investigations. Turbulence with length scales proportional to the grid spacing can be developed that decay downstream of the grid. The length scales generated are approximately half the grid spacing and the turbulent kinetic energy decays with a power exponent of around 1.3.

By choosing a grid of specific size and a specific distance downstream, turbulence of specific length scale and turbulence intensity can be generated.

2.5 Turbulence in tidal flows

Due to the large Reynolds numbers (3×10^8 in the Seymour Narrows (Grant et al. 1961)) of tidal flows they are inherently turbulent. Turbulent structures are created from the rough sea bed and also from flows around headlands, or even islands. To maximise power output and hence improve the economic viability of an installed tidal device, or tidal array, they would be located in areas with maximum tidal resource and hence highest velocities. These locations are therefore likely to have some of the most extreme turbulent conditions. It is necessary to understand what these conditions are to enable robust design of devices and how these highly turbulent flows may impact on device performance.

One of the first investigations on the turbulence characteristics in a tidal flow was by Bowden & Fairbairn (1956) whose investigation was performed off Red Wharf bay, Anglesey, Wales with a mean depth of 16 m and a maximum flow velocity of 0.5 m/s. Measurements were made using an electromagnetic flow meter attached to a tripod that was secured to the sea bed. Measurements were made at heights of 0.75-1.75 m above the sea bed. Further measurements were made at this site and later published by Bowden (1962). The mean turbulence intensity was found to be 11 % with a turbulent length scale of 3.68 m. It was found that the turbulence intensity and length scales were roughly constant over the range of depths. However, these measurements were made very close to the sea bed so the turbulence characteristics may differ from those further away from the bed where tidal turbines would be installed.

Grant et al. (1961) towed a hot-film probe in the Discovery Passage on the west coast of Canada. The discovery passage is a channel of approximately 100 m depth and 1600 m width. The max velocity was 1.49 m/s and measurements were taken roughly on the centreline. The turbulence intensity was not recorded but the turbulent length scale was estimated to be around 50 m. One limitation of this study was towing the hot-film probe as maintaining the ships heading proved difficult due to low speeds required to hold the ship steady in the turbulent flow.

Bowden & Howe (1963) continued their earlier work taking measurements in the river Mersey with a mean depth of 8.5 m and maximum velocity of 2 m/s. Measurements were made at 5.5 m above the river bed using the electromagnetic flow meter used for their previous studies. Turbulence intensities were found to be 2.9 % while the length scale was found to be 12.7 m. This is in contrast to their earlier work where measurements were made close to the bed. Here the length scales are much larger yet the turbulence intensity is lower. It is likely that the length scales were constrained close to the bed, as found in their earlier work (Bowden 1962). As the depth increases the turbulent eddies can grow as the constraints imposed by the sea bed are further away. However, this river site is likely to differ from those chosen by tidal turbine developers.

Kawanisi & Yokosi (1994) investigated the turbulence characteristics of the Ota river estuary in Japan. The river is 5 m deep and 100 m wide with a max flow velocity of 0.4 m/s. Measurements were made using electromagnetic and ultrasonic current meters at a depth 1.2 m above the bed. They found large turbulence intensities of 60 % and length scales of 8 m. These results are in contrast with Bowden & Howe (1963) as the turbulence intensity seems very large. This may be due to the low mean velocity used to calculate the turbulence intensity.

Later, Lu et al. (2000) used an Acoustic Doppler Current Profiler (ADCP) to measure length scales of around 3 m in the Cordova channel, Canada. The channel is 30 m deep, 1000m wide with a mean velocity of 1 m/s measured 3.6 m above the bed. No turbulence intensity was presented.

One downside of these early studies is the relatively low velocities compared to those expected at tidal farm sites. More recent work by Milne et al. (2013), Thomson et al. (2012) has looked specifically at the turbulence characteristics of tidal turbine development sites. Milne et al. (2013) investigated the turbulence characteristics of a 55 m deep, 1000 m wide channel at the Sound of Islay, UK. The maximum flow speed was 2.5 m/s and measurements were made with an ADV rigidly mounted 5 m above the bed. Measurements were sampled over a 15 day period to capture both spring and neap tides. The average turbulence intensity was found to be 12.5 % with an average length scale of 12.5 m.

Thomson et al. (2012) investigated the turbulence characteristics at two sites off headlands in the Puget Sound, USA. At the first site, Nodule Point, an ADV was installed for 4.3 days and an ADCP for 17 days. The measurement location was approximately 650 m east of Marrowstone Island with a depth of 22 m and maximum velocity of 2 m/s measured 4.7 m above the bed. They recorded an average turbulence intensity of 9.9 % with a length scale of 76.5 m. This compares to their second site where two acoustic wave and current (AWAC) profilers were installed for 11 and 32 days approximately 1000 m off Admiralty Head. Here the depth is 56 m with a maximum velocity of 3.2 m/s measured 8.1 m above the bed. The average turbulence intensity was 10.7 % with a length scale of 158 m. In this study they also considered the contribution to turbulence intensity across the range of turbulent eddy sizes, termed *fractional turbulence intensity*. This showed that at Nodule Point the turbulent motions were as large as 200 m with the fractional turbulence intensity roughly constant at 2.5 % from 50-200 m. At Admiralty Head the largest turbulent structures were in excess of 600 m and the fractional turbulence intensity was roughly constant with scales above 50 m at approximately 2-2.5 %. Although for these two sites the dominant turbulent structures are around three times the depth, or 15 % of the distance off-shore there is a broad range of scales present.

Table 2.2: Integral length scales normalised by depth and distance to shore for different tidal study sites.

Location type	Velocity U (m/s)	Depth, d (m)	Distance to shore, d_s (m)	ℓ/d	ℓ/d_s	Author
Headland	0.5	16	2000	0.23	0.002	Bowden & Fairbairn (1956)
Channel	1.5	100	800	0.5	0.06	Grant et al. (1961)
Channel	2	8.5	-	1.5	-	Bowden & Howe (1963)
Channel	0.4	5	50	1.6	0.16	Kawanisi & Yokosi (1994)
Channel	1	30	500	0.1	0.006	Lu et al. (2000)
Channel	2.5	55	500	0.23	0.025	Milne et al. (2013)
Headland	2	22	650	3.48	0.18	Thomson et al. (2012)
Headland	3.2	56	1000	2.82	0.16	Thomson et al. (2012)

2.5.1 Discussion

For each of these investigations the length scale has been normalised by both depth and distance off-shore. Table 2.2 shows the normalised length scales from each study. It can be seen that there is large variation between the results with length scale over depth ratios from 0.1-3.5. It could be argued that the earlier studies by Bowden & Fairbairn (1956), Grant et al. (1961), Bowden & Howe (1963), Kawanisi & Yokosi (1994), Lu et al. (2000) performed at lower tidal velocities may not be totally representative of the sites suitable for tidal turbine installation. However, there are still large variations between the later work by Milne et al. (2013) who found a length scale to depth ratio of 0.25, but Thomson et al. (2012) found length scale to depth ratios of around 3. One possibility for this discrepancy is that Milne et al. (2013) studied a tidal channel whereas Thomson et al. (2012) studied sites located off headlands. These headlands could introduce large structures that could not form in a bounded channel, but in both cases the turbulence intensity was found to be around 10 %.

2.5.2 Summary

In summary, investigations on the turbulence characteristics in tidal flows suitable for tidal turbine installations are few. The studies that have been undertaken show that the turbulence intensity is around 10 %, but the turbulence length scale seems to be site specific, and probably depend upon bed roughness and proximity to headlands or other large features in the flow. They do however show that there is a broad spectrum of turbulent structures with the largest scales significantly larger than turbine diameter.

Chapter 3

CFD techniques for modelling tidal turbines

This chapter describes the methodology known as *Computational Fluid Dynamics (CFD)* used to simulate fluid flows. Later in the chapter (section 3.5) different rotor models used to represent tidal stream turbines in CFD models are presented and the current state-of-the-art discussed.

3.1 Introduction and general methodology

As discussed briefly in section 2.1 the Navier-Stokes equation can be solved numerically to obtain solutions for $u(t)$. There are a number of different methodologies but they all come under the generic name *Computational Fluid Dynamics* (CFD). This chapter outlines these different methodologies along with their advantages and disadvantages. For further reading refer to Versteeg & Malalasekera (1995).

- The simplest method provides solutions for the mean flow field only by solving the *Reynolds Averaged Navier-Stokes* (RANS) equations. The effect of Reynolds, or ensemble, averaging the Navier-Stokes equation introduces an extra stress term that must be modelled, approximated, to provide closure to the resulting set of equations. There are a number of turbulence models that may be used that vary in complexity and accuracy. These include the zero-equation mixing length model, two-equation models such as the $k - \epsilon$ model, to the more complicated Reynolds stress model. Details of these turbulence models are discussed in the next section. Overall, RANS simulations are relatively cheap to compute, agree well with a wide range of experimental data, but only resolve the mean flow field and hence do not provide any information on the turbulent structure.

- It is possible to obtain solutions to the Navier-Stokes equations without any modelling assumptions. This is known as *Direct Numerical Simulation* (DNS). This method fully resolves all scales of motion in the flow but at a huge computational cost. DNS are therefore only feasible for very simple geometries at low Re.

- In between these two methods are *Large Eddy Simulations* (LES) where the large scale structures are fully resolved but the smaller scale structures are modelled in a similar way to RANS simulations. This is achieved by applying spatial filters to the Navier-Stokes equations splitting them into the resolved, grid scale, component and the modelled, sub-grid scale, component. It has been argued that the largest energy containing eddies have the greatest effect on the flow field and therefore LES provides an increased level of accuracy over RANS without the huge computational cost of DNS.

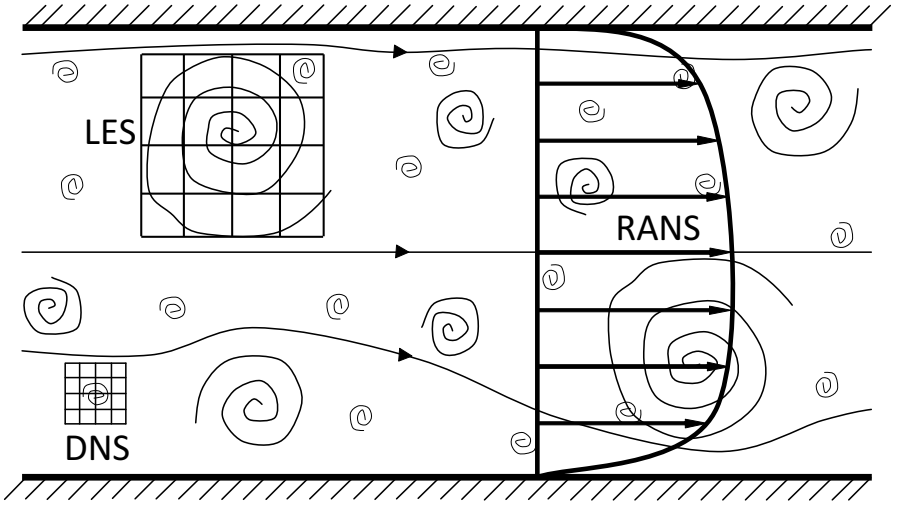

Figure 3.1: Comparison of RANS, LES and DNS simulation methods.

Figure 3.1 shows graphically the range of detail resolved by each of these methods. RANS can provide sufficient accuracy for a wide range of engineering applications but in certain cases where the flow is unsteady certain features and flow effects may not be captured. Therefore LES provides a more accurate representation of the flow field by resolving the larger eddies at a more modest computational cost when compared with DNS. Although there are significant differences in the level of detail resolved, the solution process remains the same for each case. Typically the finite volume method is used to solve a set of partial differential equations numerically. The solution process can be split into three distinct sections, pre-processing, solving, and post processing (Versteeg & Malalasekera 1995).

3.1.1 Pre-processing

Pre-processing contains all the tasks required to set up a problem before it can be solved. This includes:

- Defining the computational domain - the geometry through which the fluid will flow.
- Meshing - sub-dividing the computational domain into smaller control volumes, or cells.
- Definition of fluid properties.
- Assigning appropriate boundary conditions to the cells that touch the domain boundaries.
- Defining appropriate solution control parameters such as discretisation methods, time-steps, solution write control...etc.

One of the key tasks in pre-processing is the mesh generation. The resolution of the solution is dependent on the mesh as the solution quantities (velocity, pressure,...) are stored at the cell centres. Therefore if the mesh is too coarsely spaced then flow features may not be fully resolved. Solution accuracy therefore increases with the number of cells but at the expense of an increase in computational requirements. As quantities are solved at each cell centre, increasing the number of cells increases the number of equations to be solved. Before any conclusions can be drawn from the results of a CFD simulation a mesh independence study must be performed to show that the solution is not unduly influenced by the mesh.

3.1.2 Solving

The solution time steps and cell size are linked through the Courant number as shown in equation 3.1. For $C_o > 1$ this implies that the transported quantity has travelled further than the cell size in one time step which can lead to instabilities and cause the solution to diverge.

$$C_o = \frac{u\Delta t}{\Delta x}. \tag{3.1}$$

Where u = velocity across cell; Δt = time step; Δx = cell size.

The finite volume method was developed as a special finite difference formulation. Finite difference formulations approximate the derivative of a variable at a specific location

based on the values at neighbouring locations (Versteeg & Malalasekera 1995). The formulations are usually generated using a truncated Taylor series expansion and therefore introduce an error, or residual, to the final solution. The steps required for the finite volume method are:

Integration of the governing equations over all control volumes (cells). Refer to appendix A.1 for details of the volume integration.

Discretisation - substitution of finite-difference approximations into the integrated equation creating a set of algebraic equations. Refer to appendix A.2 for details of discretisation schemes based on Taylors series expansion.

Solution of the equations using an iterative method. Generally the velocity and pressure fields are unknown, but both fields are linked. For steady-state RANS simulations the Semi-Implicit Method for Pressure Linked Equations (SIMPLE) algorithm is used. The pressure field is guessed and a correction applied to the momentum and pressure equations. The process then iterates until the solutions converge. A relaxation factor is applied to the correction to avoid the solution diverging. However, if the relaxation factor is too small then the simulation time will become large. Because of the relaxation step the SIMPLE algorithm is slow to run but is more stable allowing larger time steps with Courant numbers greater than 1. For transient simulations (i.e. LES) the Pressure Implicit with Splitting Operators (PISO) algorithm can be used. This is a similar process to the SIMPLE algorithm but two pressure corrections are applied. The PISO algorithm is fast to run as there is no relaxation but is unstable for Courant numbers greater than 1, potentially introducing time step errors. A third option is the PIMPLE algorithm for transient simulations which is a merged PISO and SIMPLE method offering increased stability for larger Courant numbers (OpenCFD 2012).

3.1.3 Post-processing

CFD methods solve flow quantities at each cell in the solution domain. Therefore significant amounts of data are generated that describe the entire flow field, far more data than could be feasibly recorded experimentally. Processing this data can be challenging and still require significant computational resources. However, it is possible to obtain the following:

- Flow visualisation.
- Solution domain and mesh display.
- 2D and 3D surface plots.

- Line plots.
- Animations.
- Probes - output $u(t)$ at a fixed location giving the same data as would be recorded experimentally.
- Particle tracking, view streamlines...

The possibilities are almost endless but care must be taken to ensure something meaningful is obtained. The use of probes allows direct comparison with comparable data that would be recorded experimentally and are therefore used extensively in this work. Also surface plots and flow visualisation methods provide an extra insight to the flow that would be difficult to obtain experimentally.

3.2 Software selection and computer hardware

There are many CFD packages available for solving fluid flow problems. Table 3.1 lists just a few such packages, some are freely available while others are commercially owned. Simulations were run on the iridis3 high performance computer cluster at the University of Southampton with over 11500 processor cores and a user limit of 512. If using commercial software the number of cores available to use is limited by the number of software licenses available. This may mean the simulation run time would be unacceptable for larger LES models. Therefore an open source code was required where no license limit exists. Another benefit of open source software is that the solvers can be modified as required by the user. This would allow different turbine models (as discussed in section 3.5) to be implemented as required.

OpenFOAM® (Open Field Operation and Manipulation) was chosen as it has a large user base across a wide range of engineering and scientific industries - both commercial and academic. The code is written in c++ and is modular in structure allowing solvers to be edited and modified as required. There are also pre-processing tools for mesh generation and post-processing tools for analysing results (OpenCFD 2012).

3.3 Turbulence modelling

This section describes the three different turbulence models used with CFD. The first, *Direct Numerical Simulation (DNS)* makes no assumptions and resolves all scales of motion.

Next *Reynolds Average Navier-Stokes (RANS)* turbulence models are discussed where the solutions are steady state requiring modelling assumptions to be made.

Table 3.1: CFD software packages

Software	Details	Software type
OpenFOAM®	General purpose	Open source
Phoenics	General purpose	Commercial / old versions freeware
ISAAC	Turbulence model testing	Open source
Ansys CFX	General purpose	Commercial
Fluent	General purpose	Commercial
Star-CCM+	General purpose	Commercial
Channelflow	Specific for channel flows	Open source
Typhon	General purpose	Open source

Finally *Large Eddy Simulations (LES)* are discussed where the largest turbulent structures are resolved and the smaller scales are modelled. Large eddy simulations (LES) are therefore somewhere between Direct numerical simulation (DNS) and Reynolds Averaged Navier-Stokes (RANS) models in terms of the level of detail resolved and modelling assumptions made.

3.3.1 DNS

Direct Numerical Simulations (DNS) resolve all scales of motion and therefore no modelling assumptions are made. The results can therefore be thought of as numerical experiments providing information on the whole flow field that would be difficult to obtain experimentally. However, the computational cost is enormous. The smallest scales of motion are less than 1 mm requiring a very fine mesh to capture. Therefore DNS is only really feasible for simple geometries at low Reynolds numbers. It is commonly used to perform fundamental research on turbulence.

3.3.2 RANS

The RANS equation (3.2) is obtained by Reynolds averaging the Navier-Stokes equation (equation 2.10). Solving numerically returns the steady-state time average velocity and turbulence fields.

$$\frac{\partial U_i}{\partial t} + \frac{\partial (U_i U_j)}{\partial x_j} = -\frac{1}{\rho}\frac{\partial p}{\partial x_j} + \frac{\partial}{\partial x_j}\left[\nu\left(\frac{\partial U_i}{\partial x_j} + \frac{\partial U_j}{\partial x_i}\right)\right] + \frac{1}{\rho}\frac{\partial}{\partial x_j}\left(-\rho\overline{u_i u_j}\right). \tag{3.2}$$

The term $(-\rho\overline{u_i u_j})$ is the Reynolds stress introduced as a result of averaging. The Boussinesq *turbulent-viscosity hypothesis* is used to relate the Reynolds stress to the mean rate of strain (Pope 2000), as shown in equation 3.3.

Table 3.2: RANS turbulence models

Turbulence Model	Equations to Solve	Turbulent structure in 3 dimensions	Computational Expense
Spalart-Allmaras	1 algebraic	Isotropic	Cheap
$k-\epsilon$	2 PDE's	Isotropic	Low
$k-\Omega\ SST$	2 PDE's	Isotropic	Low
Algebraic stress model	2 PDE's + 6 algebraic	Anisotropic	Modest
Reynolds stress model	7 PDE's	Anisotropic	Expensive

$$(-\rho\overline{u_i u_j}) + \frac{2}{3}\rho k\delta_{ij} = \rho\nu_T\left(\frac{\partial U_i}{\partial x_j} + \frac{\partial U_j}{\partial x_i}\right). \tag{3.3}$$

Where the coefficient of proportionality ν_T is the *turbulent viscosity*. This term must be resolved using a turbulence model. Table 3.2 gives some details on computational expense of some of the common models.

While the two stress models are capable of resolving secondary currents found in channel flows (Nezu 2005) their computational cost is large when compared to the simpler two equation models. Harrison (2011) compared the $k-\epsilon$ and $k-\Omega\ SST$ for modelling the wakes of tidal stream turbines. It was found that the $k-\epsilon$ turbulence model provided a small improvement over the $k-\Omega\ SST$ model resulting in improved agreement with experimental data. The $k-\epsilon$ model is also one of the most widely validated models and therefore commonly used for engineering applications (Versteeg & Malalasekera 1995). This model was therefore chosen due to its computational efficiency and proven agreement with experimental data for the simulation of tidal stream turbines.

$k-\epsilon$ turbulence model

The turbulent kinetic energy, k, and the turbulence dissipation, ϵ, are solved as transported quantities in the flow (Versteeg & Malalasekera 1995) and the turbulent-viscosity calculated using the following relation.

$$\nu_T = C_\mu\frac{k^2}{\epsilon}. \tag{3.4}$$

Where $C_\mu = 0.09$ is a constant of proportionality.

Inlet boundary conditions for $k-\epsilon$ RANS simulations can be specified as mean flow quantities as they are steady-state. The inlet velocity can be set as a mean velocity profile, either obtained experimentally or using some other shape such as a power or log profile.

The turbulent kinetic energy can be calculated using the mean velocity and turbulence intensity as shown in equation 3.5.

$$k = \frac{3}{2} I^2 U^2. \tag{3.5}$$

The turbulent dissipation can be calculated using equation 3.6 where L is the characteristic length scale of the turbulent eddies in the flow.

$$\epsilon = C_\mu^{3/4} \frac{k^{3/2}}{L}. \tag{3.6}$$

Assumptions

The assumptions and limitations made for the $k - \epsilon$ RANS model are as follows.

- Turbulence is assumed isotropic.
- Only mean statistics can be computed as steady-state.
- A single length scale must be used, whose value could affect the results.

For most industrial applications RANS simulations perform well due to their simplicity and low computational cost. The $k - \epsilon$ turbulence model has also been widely validated against experimental data. However, there are still many situations where RANS simulations do not perform well. These situations include rotating/swirling flows with large strains, fully developed flows in non-circular ducts (as secondary currents cannot form due to the assumption of isotropy Nezu (2005)), and flows that are inherently unsteady. For these situations a more advanced simulation technique is required where fewer assumptions about the turbulent structure are made, such as LES.

3.3.3 LES

The LES equation 3.7 is obtained by filtering the Navier-Stokes equation (Pope 2000). This splits the velocity into a filtered or resolved component, $\overline{u}$, and a residual component that is modelled, u^*. Hence, $u = \overline{u} + u^*$. This is similar to the effect of Reynolds averaging but here $\overline{u}$ is not the mean velocity, it is the mean plus the large scale resolved structures.

$$\frac{\partial \overline{u}_i}{\partial t} + \frac{\partial}{\partial x_j}(\overline{u}_i \overline{u}_j) = -\frac{1}{\rho}\frac{\partial \overline{p}}{\partial x_j} + \frac{1}{\rho}\frac{\partial \tau_{ij}^R}{\partial x_j} + \nu \frac{\partial^2 \overline{u_i}}{\partial x_j^2}. \tag{3.7}$$

The residual stress τ_{ij}^R is introduced as an effect of filtering, similar to the Reynolds stress introduced by Reynolds averaging for the RANS equation. The filtered equations contain turbulent scales of size L and above and should lie in the inertial sub-range as shown in figure 3.2. For this investigation the filter size was taken as the cubic root of the cell volume, which for a uniform hexahedral mesh is equivalent to the cell size, hence $L = \Delta$.

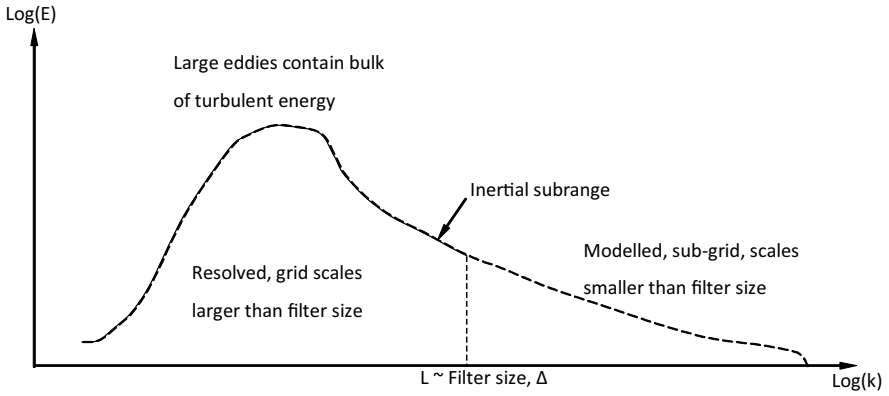

Figure 3.2: Resolved and modelled LES components on an energy spectra (adapted from Pope (2000)).

To provide closure to the filtered equations the residual stress is modelled in a similar way to the Reynolds stresses in the RANS equation, and known as the sub-grid scale turbulence model.

3.3.4 Sub-grid scale (SGS) turbulence models

There are many different sub-grid scale (SGS) turbulence models available for LES, most of them analogous to RANS turbulence models. Table 3.3 compares some of the common SGS turbulence models. While the more advanced SGS models provide increased levels of realism through reduced assumptions their computational cost increases. However, unlike RANS where the turbulence model is employed to account for all turbulence, the SGS model is only required to model the turbulent structures smaller than the filter size that lie within the inertial sub-range. Here the turbulence can be assumed isotropic and dependent only upon the rate of dissipation, as argued by Kolmogorov in his universal equilibrium theory (section 2.3.2). It is the influence of the large turbulent structures, that are fully resolved in LES, on the flow field that is of interest in this study. Therefore it is likely that any differences between the SGS models used will have a small effect on the results. In some studies no SGS model is used based on the argument that the energy contained in the smallest resolved eddies is insignificant when compared to the largest scales (Johnstone & Coleman 2012). It was therefore decided to use the Smagorinsky model based on its computational efficiency while still providing some information on the sub-grid scales if required.

Table 3.3: LES Sub grid scale turbulence models.

SGS Model	Details	Computational Expense
Smagorinsky - Mixing length	SGS stress calculated using filter size and Smagorinsky coefficient which is uniform throughout the domain.	Cheap
Dynamic Smagorinsky	Same as for the Smagorinsky model but the Smagorisnky coefficient is calculated locally from the resolved scales for each time step.	Low
	Transport Models:	
One equation	SGS stress is calculated as a transported quantity.	Low
Two equation	SGS stress calculated from two transported quantities such as kinetic energy and turbulence dissipation ($k-\epsilon$).	Modest
Reynolds stress models	SGS stress calculated from transported Reynolds stresses.	High

The Smagorinsky SGS turbulence model

A Bousinesq hypothesis is first assumed to relate the residual stress to the filtered rate of strain tensor $\overline{S_{ij}}$ (Pope 2000).

$$\overline{S_{ij}} = \frac{1}{2}\left(\frac{\partial \overline{u_i}}{\partial x_j} + \frac{\partial \overline{u_j}}{\partial x_i}\right). \tag{3.8}$$

$$\tau_{ij}^R = -2\rho\nu_R\overline{S_{ij}}. \tag{3.9}$$

where the constant of proportionality ν_R is the eddy viscosity of the residual motion, otherwise known as the sub-grid scale viscosity. The sub-grid scale viscosity is then modelled as

$$\nu_R = \ell_S^2\overline{S_{ij}} = (C_S\Delta)^2\overline{S_{ij}}. \tag{3.10}$$

where ℓ_S is the Smagorinsky length scale which is assumed proportional to the filter width Δ, with Smagorinsky constant of proportionality C_S. This is supposed only if Δ lies within the inertial subrange, Pope (2000).

3.4 Modelling inflow conditions for LES

One difficulty of using LES is specifying realistic inlet turbulence to the computational domain. In RANS simulations the average turbulence intensity can be measured experimentally and set as the inlet value. However, as LES simulations are transient this is not possible and the fluctuations also need to be correlated spatially and temporally. The different methods of generating turbulence for LES can be assigned to one of two methods: allow turbulence to develop in the computational domain (i.e. drive turbulence from a boundary layer flow), or apply synthetic turbulence fluctuations on the inlet boundary. The following sections discus these methods in more detail and propose a new method of generating turbulence in LES simulations where the turbulence intensity and integral length scale can be controlled.

3.4.1 Pre-computation

Pre-computation methods use stream wise periodic boundaries in the domain to cycle the flow over a boundary. This develops turbulence from the shear generated by the wall and produces a library of time data to apply to the inlet of further simulations. This method is inefficient due to the time taken and storage of the turbulence inlet data set. Chung & Sung (1997) proposed a method of using a shorter pre-computation which was then cycled on the inlet. Phase or amplitude jitter was then introduced to avoid fictitious periodicity that would be introduced from cycling a short time period on the inlet. However it was found that a considerable inlet length to the simulation was required to allow the flow to evolve into 'real' turbulence following the phase jittering method. A more efficient method in terms of time and data storage was described by de Villiers (2006) where an internal mapping plane is used that recycles the flow upstream of the main solution domain. The advantage of this method is that no pre-computation is required. In both of these methods the turbulence develops naturally and there are no assumptions in its structure. However it does mean that it is almost impossible to generate specific length scales and turbulence intensities as the turbulence is driven by the boundary layer of the domain.

3.4.2 Synthetic inlet

The simplest form uses random noise where a random fluctuation is superimposed on a mean flow. However these fluctuations are not correlated and therefore do not have any turbulent structure. As a result they are rapidly dissipated (Tabor & Baba-Ahmadi 2010). Work has been carried out by Smirnov et al. (2001) to manipulate the random field to satisfy continuity to produce a more realistic representation of turbulence.

While this does improve the turbulence generated it does still not satisfy the momentum equations and therefore offers poor control at generating 'real' turbulence. More advanced synthetic inlet methods such as that described by Fathali et al. (2008) first filter a random field to satisfy pre-specified correlations and then combine with appropriate coefficients to generate a turbulent field with specified spectra, length scales and intensities. Kornev et al. (2009) used a turbulence spot method to further improve the accuracy of synthetic inlets to prescribed second order statistics (integral length scale, integral time scale, two-point spatial and one-point temporal autocorrelations and one-point cross correlations between fluctuation components). Here the flow is thought of as motions of turbulent spots arising from random positions at random times. Each spot has an inner velocity distribution that satisfies the specified statistical quantities.

3.4.3 Discussion

Comparisons of synthetic and pre-computation methods performed by Tabor & Baba-Ahmadi (2010) showed that a reasonable inlet length was still required to allow synthetic turbulence to develop into 'real' turbulence. They concluded that the internal mapping method was still the most efficient for generating turbulence in LES, which is in agreement with de Villiers (2006). However, there are still situations where one may want to run simulations with prescribed integral length scales and turbulence intensities to understand the effects of these quantities on a particular device. An alternative method of generating turbulence in LES is therefore required. The proposed technique, as implemented in chapter 8, is based on the idea of grid generated turbulence. The turbulence intensity can be controlled by varying the distance to the inlet and the integral length scale can be controlled by changing the size of the grid. Refer to section 2.4 for further details on grid generated turbulence.

Grid generated turbulence is seldom used to generate turbulence for LES models. Reese et al. (2007) used a grid in their solution domain to generate turbulence for the investigation of noise in a low pressure fan encountering highly turbulent flow. They found the grid generated turbulence compared well with experimental data. However their grid was placed downstream of their inlet which would increase the cell count and hence computational time. Using a grid pattern on the inlet boundary minimises the number of cells in the domain but allows turbulence to develop naturally in the simulation. This technique has not been used before and its implementation discussed in chapter 8.

3.5 Rotor modelling in CFD

A turbine extracts kinetic energy from a fluid flow. The approaching flow slows down as it approaches the turbine so it is already lower than the free-stream velocity as it

reaches the turbine. As the fluid slows the stream-tube must expand, to maintain mass continuity, and the static pressure rises as no work has been done. When flow passes through the turbine kinetic energy is extracted reducing the flow velocity with a corresponding drop in static pressure to below the atmospheric level. Downstream of the turbine the flow inside the stream-tube has reduced velocity and static pressure. This region is known as the *wake*. As the distance downstream increases the static pressure rises until it reaches the atmospheric level and equilibrium is achieved. Therefore there is no change in static pressure between the far upstream and downstream, but a reduction in kinetic energy (Burton et al. 2001).

There are a number of viable possibilities for modelling a turbine rotor within CFD simulations (Sanderse et al. 2011). However, the different methods fall into two categories. Either the turbine blades are fully resolved in the computational domain; or a momentum sink body force is applied to the governing equations to represent the effects the turbine has on the surrounding flow. These are listed below and shown illustrated in figure 3.3.

a) Uniform actuator disc - the average force exerted on the flow by the turbine is applied uniformly over the same swept volume as occupied by the rotor - No blade data is required, just the turbine C_T. This is a uniform actuator disc.

b) BEM actuator disc - sectional blade forces can be calculated using blade element momentum theory (BEM) and smeared over an annulus. This results in a non-uniformly loaded actuator disc where rotational forces are also applied. Sectional lift and drag data is required for the turbine blades and corrections applied to account for tip-losses.

c) Actuator line - an extension of the non-uniformly loaded actuator disc where instead of smearing the blade forces they are applied over a line representing the location of the turbine blade. The line rotates as a turbine blade would and tip vortices are resolved.

d) Full turbine rotor model - the turbine blades can be solved directly by including them in the computational domain.

While it is possible to model a complete tidal turbine rotor, eliminating any assumptions when using an actuator disc representation, the computational cost is huge. Sezer-uzol & Long (2006) modelled a single NREL Phase VI wind turbine using an LES turbulence model. While this model is capable of capturing complex flow features, such as tip vortices, the simulation required 90,000 iterations per rotor revolution (0.83s). This equated to a wall time of almost 2 days when run on a computer cluster with 128 cores, or up to 42 days when run on a cluster with 16 cores! This level of detail and computational expense may be acceptable for the design of a specific device, but becomes

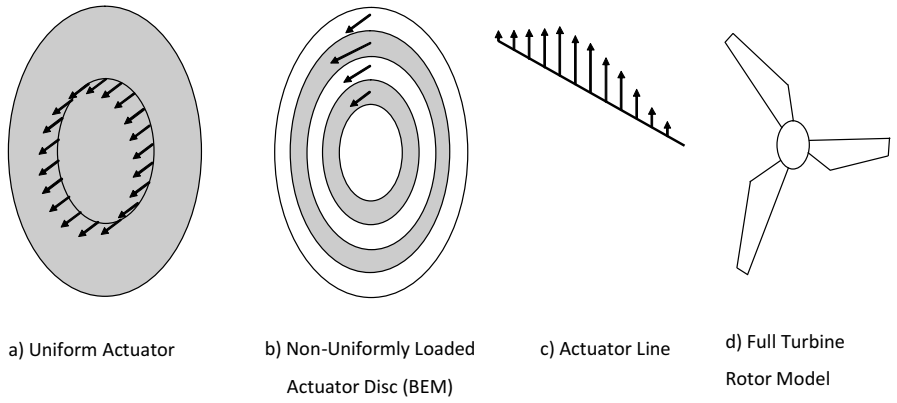

Figure 3.3: Graphical representation of the different turbine models for use with CFD (adapted from Sanderse et al. (2011)).

unfeasible when considering a farm with multiple devices, or where a large sample size is required to calculate turbulence statistics. Therefore a simpler uniform actuator disc may be required. The next section presents the uniform actuator disc theory before a review of the current state-of-the-art RANS and LES modelling of turbines.

3.5.1 Actuator Disc Theory

It is possible to analyse the hydrodynamic behaviour, without specific consideration of a turbine design, by considering the energy extraction process. This is known as an *actuator disc* and shown in figure 3.4. The actuator disc assumes forces applied to the surrounding flow field by the turbine are applied uniformly over the same swept volume as occupied by the rotor. A useful quantity that describes how much the free-stream has slowed across the disc is the axial induction factor.

$$a = \frac{U_\infty - U_t}{U_\infty}. \tag{3.11}$$

Where ∞ = conditions far upstream; t = conditions at the turbine (actuator disc); w = conditions in the far wake. Rearranging, the velocity at the actuator disc is:

$$U_t = U_\infty(1 - a). \tag{3.12}$$

The performance of a turbine, or actuator disc, is commonly reported as non-dimensional quantities of power and thrust. The power and thrust coefficients are defined as:

$$C_P = \frac{P}{0.5\rho U_\infty^3 A}. \tag{3.13}$$

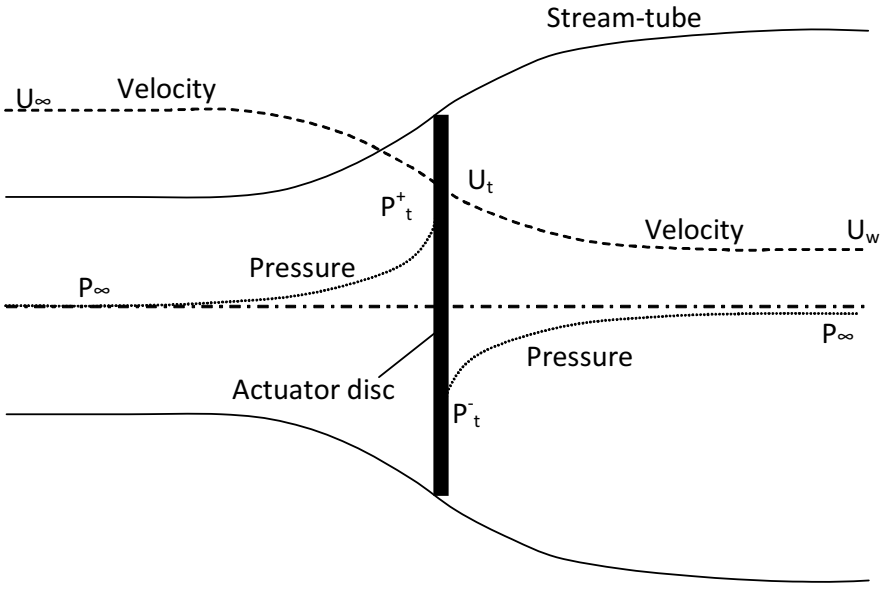

Figure 3.4: Actuator disc stream-tube with velocity and pressure profiles across the disc (adapted from Burton et al. (2001)).

$$C_T = \frac{T}{0.5\rho U_\infty^2 A}. \tag{3.14}$$

Where T = thrust; P = power; U_∞ =free-stream velocity; A = swept area of turbine; and ρ = fluid density.

Through application of Newton's second law of motion, the conservation of mass, and Bernoulli's equation, an expression relating the power coefficient to the axial induction factor may be determined (equation 3.15). Refer to Burton et al. (2001) for the full derivation.

$$C_P = 4a(1-a)^2. \tag{3.15}$$

Similarly the thrust coefficient may be determined from:

$$C_T = 4a(1-a). \tag{3.16}$$

By differentiating equation 3.15 with respect to a and setting equal to zero the maximum value of C_P can be found. This occurs at an axial induction factor of $a = 1/3$ with $C_{P_{max}} = 16/27 = 0.593$ and $C_{T_{max}} = 8/9 = 0.889$. This was first shown by Albert Betz and has become known as the Betz limit as no design has exceeded this value.

It can be seen, by comparison of equations 3.15 and 3.16, that the power and thrust of a turbine are related by a factor $(1 - a)$. Therefore measurements of turbine thrust can be used to infer trends in turbine power output.

Turbine wake deficit

A turbine converts kinetic energy of a fluid flow into electrical energy. As kinetic energy is removed from the flow the velocity downstream of the turbine is lower than the upstream value. This region of reduced velocity is known as the wake. As the distance downstream of the turbine increases the wake velocity gradually increases as turbulent mixing transports higher momentum fluid from the free stream flow into the wake region. At some point downstream the wake recovers and a uniform velocity profile develops, similar to the upstream profile but with lower overall momentum due to the energy extraction. A parameter commonly used to quantify the wake and its recovery is the velocity deficit, given by:

$$U_D = 1 - \frac{U_w}{U_\infty}. \tag{3.17}$$

Wake regions

The wake behind a turbine or actuator disc may be characterised into two regions (Vermeer et al. 2003, Crespo & Hernandez 1996, Sanderse 2009). Refer to figure 3.5 for a schematic of the wake profile.

Near wake generally assumed to be $1D - 3D$ downstream, an annular shear layer separates the inner core of the wake from the ambient flow (Crespo & Hernandez 1996). Within the shear layer turbulent mixing occurs while the flow characteristics of the inner core are driven by the turbine geometry (Sanderse 2009).

Far wake beyond the near wake region, after the shear layers meet at the centreline, the far wake begins. In the far wake region the specific turbine geometry is not important as any large scale turbulent structures have been broken up though mixing in the shear layer, and the wake profile may be assumed to be axisymmetric with a Gausian profile (Sanderse 2009). In this region wake interaction between other turbines, flow boundaries, and turbulence is of greater importance for wake modelling (Vermeer et al. 2003).

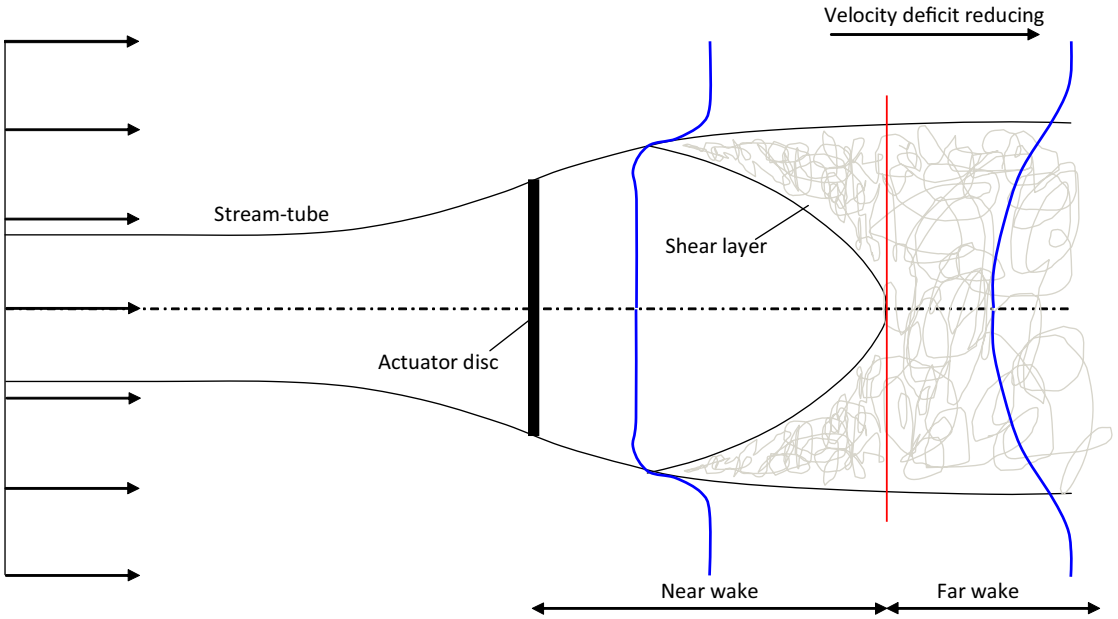

Figure 3.5: The wake regions behind a turbine or actuator disc (adapted from Sanderse (2009)).

3.5.2 Addition of body force to CFD equation

This section discusses how a momentum sink body force may be calculated and added to right hand side of the RANS or LES equations to account for the energy extraction by a turbine.

Uniform actuator disc

Actuator disc theory can be used to derive a momentum sink term, F_B, applied to the right hand side of the RANS or LES equation (3.2 and 3.7 respectively). The momentum sink term is applied in the actuator disc region and accounts for the extraction of kinetic energy from the flow by the turbine. Equating the equations for thrust coefficient (3.14, 3.16) and rearranging yields the thrust force in terms of the free-stream velocity and axial induction factor.

$$T = 2\rho A U_\infty^2 a(1-a). \tag{3.18}$$

For constant density, the momentum sink term (F_B) is the thrust force divided by the density and actuator disc volume, V_t. The momentum sink term is the thrust force per unit mass with units of ms^{-2}, and is therefore strictly speaking an acceleration.

$$F_B = \frac{T}{V_t \rho} = 2\frac{A}{V_t} U_\infty^2 a(1-a). \tag{3.19}$$

For a given axial induction factor and free stream velocity the momentum sink term applied is constant and no further turbine information is required to implement this technique.

BEM actuator disc

Non-uniform blade element momentum (BEM) actuator disc body forces are derived using turbine blade section data. BEM actuator disc forces are calculated using the following steps. Refer to Harrison (2011) or Malki et al. (2013) for a full derivation.

1. The rotor is split into sections along the blade radius.
2. Lift and drag forces of each blade section are calculated using 2D airfoil data.
3. The total axial and tangential forces acting on each blade section (taking into account the total number of turbine blades) are then rotationally averaged, or smeared, around the annulus occupied by that blade section.
4. The rotation averaged axial and tangential forces are then divided by the annulus volume and applied as momentum sink terms on the CFD equations as for the uniform actuator disc.

Actuator line

The body forces applied for the actuator line model are derived using the same method as for the BEM actuator disc forces. However, the forces are not rotationally averaged and applied along a line that represents the turbine blade location at that current time. The line is then rotated for the next time step and the forces re-calculated.

Channel Reynolds number and Froude number

Dynamic similarity of full size tidal flows and small scale experiments is achieved by using equivalent Froude numbers, which is the ratio of inertial force to gravitational force as shown in equation 3.20 Massey & Ward-Smith (2006).

$$Fr = \frac{U_\infty}{\sqrt{gd}} \tag{3.20}$$

where Fr = Froude number; g = acceleration due to gravity; and d = channel depth. Typical Froude numbers of tidal sites are less than 0.5 (e.g. Fr=0.12 in the Bristol Channel (Croft et al. 2010)) and Harrison (2011) used Fr=0.17. However, maintaining Froude number similarity often results in low Reynolds numbers of the flow. Harrison

(2011) used RANS simulations to compare the wake of an actuator disc with $Re = 9\times10^5$ to a hypothetical full scale simulation with $Re = 9 \times 10^7$. It was found that there was little difference between the wake profiles for these two cases demonstrating the suitability of small scale experiments and simulations to represent full scale sites.

3.5.3 RANS models

Uniform actuator disc RANS simulations have been widely used to study the wakes of tidal turbines (Macleod et al. 2002, Sun et al. 2008, Harrison et al. 2010). Comparisons have been made between the results of small scale experiments and actuator-disc RANS simulations by Harrison et al. (2010). It was shown that the velocity deficit is over estimated on the centreline when compared to the experimental results and concluded that the RANS model is sensitive to initial conditions of boundary layer velocities and turbulence intensities. However, little consideration was made to the characteristic length scale used to define the turbulence dissipation term (equation 3.6). Values of the characteristic length are often based on the author's 'best-guess' of what the turbulence length scale might be. Harrison et al. (2010) took the length scale to be the channel depth whereas Sun (2008) took the length scale to be 0.07 times the hydraulic diameter. More complex approximations for the length scale exist based on functions relating the length scale to the wall proximity and some other length as shown by Versteeg & Malalasekera (1995). There are many options for the length scale, but due to the sensitivity of RANS simulations to initial conditions it is likely that the length scale chosen will affect the results due to changes in dissipation of turbulent kinetic energy.

Harrison (2011) compared the $k-\omega-SST$ with the $k-\epsilon$ turbulence model for RANS actuator disc simulations. It was found that the wake recovery was faster for the $k-\epsilon$ compared to the $k-\omega-SST$ and resulted in better agreement with the experimental data. The reason for this was argued to be due to the $k-\epsilon$ model being more accurate in free-shear flows experienced behind the actuator disc. A turbulent source term was then added to the actuator disc to represent the turbulence generated by a turbine. The turbulent source was calculated using an empirical relation that relates the change in turbulence intensity (ΔI_m) at the turbine to the turbines resistance coefficient, k_R (Harrison 2011).

$$\Delta I_m = 0.362 \left[1 - \sqrt{\frac{1}{1 - k_R \left(1 + \frac{k_R}{4}\right)^2}} \right]. \tag{3.21}$$

Including a turbulent source increased the turbulence intensity in the near wake significantly improving agreement with experimental data. However, little consideration was made to the characteristic turbulent length scale of the turbulent source. It is likely

that the length scale used will have an effect on the wake profile through changes in turbulence dissipation.

Malki et al. (2013) used a RANS BEM actuator disc method to model a three bladed tidal turbine. Performance predictions were compared to published experimental data and found to be in good agreement when blockage corrections were made. This approach was then used by Masters et al. (2013) to investigate the effects of an accelerating flow on the wake behind the actuator disc. Comparisons between a uniform actuator disc with turbulence source and BEM was made by Batten et al. (2013). The results showed that beyond 6D downstream there is very little difference between the two models. However, in the near wake the turbulence intensity was higher for the uniform disc due to the addition of the turbulence source term. The advantage of the BEM model was that the performance of a specific turbine design could be predicted. However, it was shown that the power coefficient was under predicted while the thrust coefficient was over predicted so further work is required to improve the accuracy of this method.

Castellani & Vignaroli (2012) used RANS simulations with uniform actuator discs to model a small wind farm with four turbines. The computational domain consisted of 4×10^6 hexahedral cells. As such the actuator disc region did not have a smooth edge, but was made up of staggered squares. A mesh independence study was performed to validate the use of this mesh. Areas on the ground corresponding to forest, sea, and land were given different roughness values in the model boundaries to generate realistic velocity profiles. Good agreement was found 2.5 diameters downstream of the turbine. The model was proposed as a simple method to estimate wake losses far downstream. The authors found that although the method is simplistic, and not designed to provide detailed near wake characteristics, it does provide a good estimation of the power losses of a wind farm through accurate prediction of the far wake. Comparisons were also made to the analytical wake model WASP. The RANS actuator disc model was shown to be far more accurate with very good agreement to the experimental data when compared to the analytical model.

3.5.4 LES models

Churchfield et al. (2013) analysed the wake propagation and power produced by an array of four turbines arranged in different configurations. Turbulence was generated in the domain by running a precursor simulation with periodic boundaries to drive turbulence from the boundary layer. The domain was 240 m long, 80 m wide and 70 m deep with a grid resolution was 0.5m resulting in a mesh with approximately 12×10^6 mesh cells. It was assumed that quasi-steady state flow conditions were achieved after a simulation time of 6000 s, or seven large-eddy turn over times. The actuator line turbine representations were then inserted in the turbulent flow. It was found that the domain was constraining the largest eddies which were found to cycle across the periodic

boundaries. This low speed cycling of turbulent structures was found to reduce the power output of the turbines on one side of the domain. This further demonstrates the sensitivity to inlet conditions, as also found by Harrison et al. (2010) for RANS models. Tip vortices were found to form on the first row of turbines but decayed rapidly on downstream turbines due to the increased turbulence levels generated by the first row. This investigation was one of the first simulations of this type applied to tidal flows and demonstrates the level of detail that can be resolved using this method. However, turbulence characteristics such as length scales and intensities in the array were not reported. This method also required huge computational resources, and even then it was found a larger computational domain was required. For application to large scale array modelling of multiple devices simplified turbine representations such as the actuator disc are required.

Wu & Porte-Agel (2011) investigated the difference between a uniform actuator disc and a BEM actuator disc in LES for modelling wind turbine wakes. The simulations were compared to experimental wind tunnel data. The mesh contained just under 1×10^6 cells and turbulent inflow conditions were generated by running a separate simulation with periodic boundaries to generate turbulence from the boundary layer. The results show that there is very little difference between the two turbine models in the far wake, greater than $5D$ down stream. Both models compared well to the experimental data and their findings are in agreement with Harrison (2011) from RANS simulations. In the near wake the turbulence intensity is under predicted while the average velocity is over predicted. The tangential forces from the BEM actuator disc introduce rotation to the flow generating shear and hence turbulence, improving agreement with the experimental data in the near wake. However, beyond 4-5D there is little rotation in the flow and the results from uniform and BEM actuator discs are comparable.

3.5.5 Discussion

Comparisons between the centreline velocity deficit from both RANS and LES models with uniform and BEM actuator discs are shown in figure 3.6. It can be seen that there is significant variation in velocity deficit from 0.1-0.75 at $x/D = 5$. As discussed previously, this variation is likely to be attributed to differences in initial conditions. Of particular interest are the results of Batten et al. (2013) and Wu & Porte-Agel (2011) who compared the uniform actuator disc with BEM actuator discs using RANS and LES respectively. It can be seen that both authors report the same trends with very good agreement between each model in the far wake, beyond 5D. However, different trends are seen in the near wake. The results from Wu & Porte-Agel (2011) show a higher deficit for the BEM model which is in contrast with Batten et al. (2013) who reports a higher deficit for the uniform actuator disc in the near wake. This difference may be explained through the consideration of turbulence. Batten et al. (2013) included

a turbulence source in the uniform actuator disc to account for the device generated turbulence which was found to increase the turbulence in the near wake. However, no turbulence source is included for the uniform actuator disc by Wu & Porte-Agel (2011). As discussed in section 3.4 the generation of turbulence in LES is complex, and therefore adding a turbulence source to an actuator disc would suffer from the same issues. In order to improve the accuracy of actuator disc LES models turbulence generation in the disc region would be required to account for the device generated turbulence.

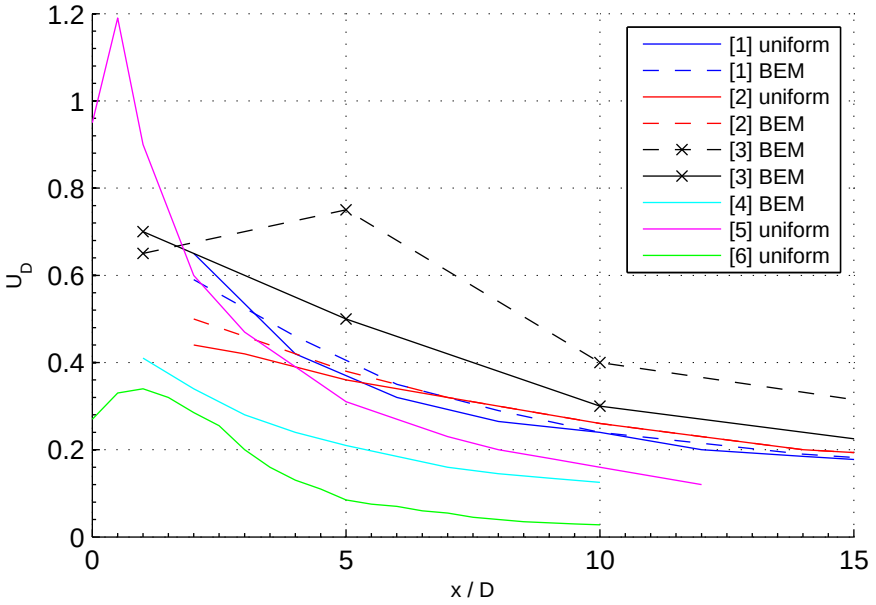

Figure 3.6: Centreline velocity deficit for different authors using different methods with $C_T \approx 0.9$. [1]: Batten et al. (2013) [2]: Wu & Porte-Agel (2011) [3]: Masters et al. (2013) [4]: Turnock et al. (2011) [5]: Sun et al. (2008) [6]: Macleod et al. (2002).

The motivation for doing this is the limited availability of lift and drag data sets for the rotor blades in different flow conditions, as required for actuator line and BEM models. Also there is a lower computational requirement compared to full rotor and actuator line methods. A uniform actuator disc model would therefore be more suited to investigate the effects of turbulence on a tidal stream turbine.

Summary

Actuator disc RANS simulations have been used to model both single devices and arrays of multiple devices. It was shown that the actuator disc simulations are sensitive to the initial conditions, but little consideration was paid to the value of the characteristic turbulent length scale used in RANS models.

It has been shown that both uniform and BEM actuator disc turbine models can produce good agreement with experimental data. However, a turbulence source is required for the uniform actuator disc to represent the turbulence generated by the turbine.

The LES actuator line method requires significant computational resources making it impractical for large array modelling. Further, the availability of lift and drag data for different turbulent flows would be a problem. However, the use of uniform and BEM actuator disc models has been shown to accurately model the wake of a turbine with LES. The BEM actuator disc performs better in the near wake due to the increased turbulence generated by the rotational forces. However, in the far wake, greater than 5 diameters downstream, there is little difference between the two methods.

Overall, actuator disc models are sensitive to the initial conditions used, but the effects of the turbulent length scale have not been considered. RANS has the advantage of lower computational requirements, while LES has the advantage of providing information on turbulence structure. As BEM models suffer from the same problem as the actuator line models with the availability of lift and drag data sets, a uniform actuator disc would allow more general results to be obtained for studying the effects of turbulence on a tidal stream turbine. However, a turbulence source would be required for the actuator disc in LES models. The next chapter considers the effects of turbulence on the wake profile and mean thrust loads of solid discs, turbine rotors, and porous disc rotor simulators.

Chapter 4

Influence of turbulence on discs and rotors

The previous chapters presented background theory on turbulence, the expected characteristics of a tidal site and CFD techniques for modelling tidal turbines. This chapter first considers how turbulence can affect the mean thrust, or drag, acting on a disc or turbine rotor. The effects of turbulence on the wake of discs and turbine rotors is then considered before the overall findings of this review summarised.

4.1 Effects of turbulence on thrust

The effects of turbulence on the thrust of a streamlined body, or sphere, have been well documented as shown in figure 4.1. Typically the effects of turbulence cause a transition from laminar to turbulent boundary layer at a lower Reynolds number than for a laminar flow. This transition injects high momentum fluid near the surface and delays the separation point of the boundary layer from the surface of the object, reducing the size of the wake, reducing the thrust (Figure 4.1). However, the effects of turbulence on the thrust of a turbine rotor, or porous disc rotor simulator are little understood. The problem is first simplified to consider the effects of turbulence on the thrust of a solid disc before the effects of turbulence on the thrust of a turbine rotor and porous disc rotor simulator are considered. The latter section considers how turbulence affects the wake of a turbine rotor and porous disc rotor simulator before an overall summary is made.

4.1.1 Solid discs

Table 4.1 shows typical thrust coefficients of a sharp edge circular disc with an average of C_T=1.17. On assuming that turbulence acts to increase the 'effective' Re this leads

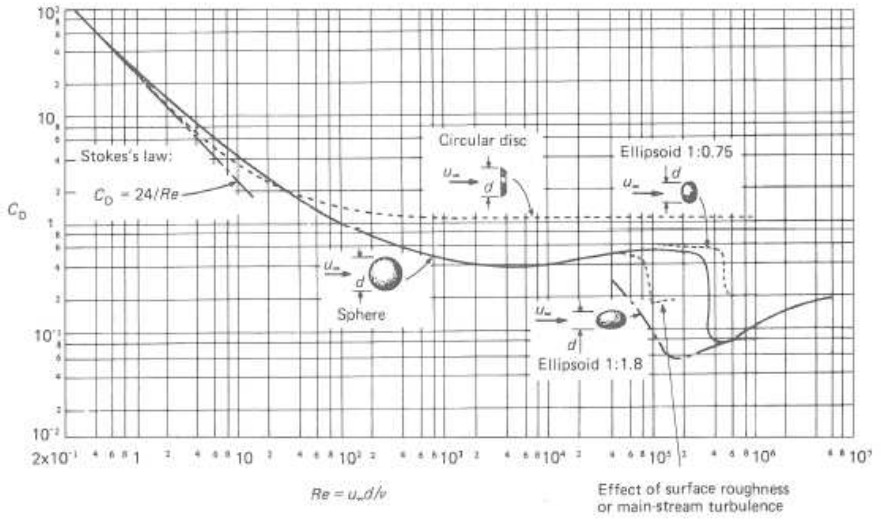

Figure 4.1: Reynolds number dependence of drag coefficient for 3D objects (Massey & Ward-Smith 2006).

Table 4.1: Influence of Reynolds number on the thrust coefficient of a sharp edge circular disc Knight (1926), Roos & Willmarth (1971).

Reynolds number RE	Thrust coefficient C_T	Author
38700	1.15	Roos & Willmarth (1971)
50100	1.16	Roos & Willmarth (1971)
60400	1.17	Roos & Willmarth (1971)
130000	1.167	Knight (1926)
195000	1.182	Knight (1926)
260000	1.186	Knight (1926)

to the general assumption that disc thrust is not strongly effected by turbulence (e.g. Massey & Ward-Smith 2006), as seen in figure 4.1. Turbulence may be characterised by a mean intensity, I, (ratio of root mean squared velocity to mean velocity) and integral length scale, ℓ, (the size of eddies containing the greatest proportion of turbulent energy).

Schubauer & Dryden (1935) first demonstrated that increasing turbulence intensity increased the thrust force acting on a circular disc. Craze (1977) confirmed this result and also demonstrated, for a limited number of cases, that the thrust force of a circular disc is also dependent on the integral length scale to disc diameter ratio (ℓ/D). Table 4.2 shows the thrust coefficients recorded for the different turbulent conditions, which are larger ($1.2 < C_T < 1.33$) than the previous low turbulence case ($C_T \approx 1.17$). Bearman & Morel (1983) also found a strong dependence on the length scale for the thrust of a circular disc and that increasing turbulence intensity always increased thrust. While a clear relationship between turbulence length scale and thrust was not found, variations in thrust in excess of 10 % have been recorded.

Table 4.2: Influence of turbulence intensity and integral length scale on the drag coefficient of a sharp edge circular disc. Note the low $C_T = 1.13$ for low level turbulence with $I < 0.5$ %.

I (%)	ℓ/D	C_T	Author
1	-	1.27	Schubauer & Dryden (1935)
3	-	1.33	Schubauer & Dryden (1935)
$<$ **0.5**	-	1.13	Craze (1977)
6	0.5	1.2	Craze (1977)
10	1	1.26	Craze (1977)

More recent studies have shown how turbulence affects the wake structure of a conical disc. It was found that free-stream turbulence acted to reduce the vortex shedding around the disc while reducing the recirculation region with lower velocities in the near wake. They associated these flow features with an increase in thrust, although no thrust measurements were made (Rind & Castro 2012).

These previous studies have demonstrated how turbulence can affect the mean thrust acting on a solid disc, but the number of test cases are limited so firm conclusions cannot be drawn. It seems likely that variations in thrust force of 10-20 % are likely with different turbulent flows but the specific interaction of integral length scale and turbulence intensity is still unclear.

4.1.2 Rotors and porous disc simulators

While investigations on solid discs have been of interest for sometime, the effects of turbulence on the thrust of turbine rotors and porous discs is a relatively new subject. Sicot et al. (2006) investigated the effects of turbulence on a model two-bladed horizontal axis wind turbine. Experiments were performed in a wind tunnel with grid generated turbulence at turbulence intensities of 4.4-12 % and integral length scales approximately equal to the chord of the turbine blades giving a length scale to turbine diameter ratio of $\ell_x/D < 0.05$. The results of their study showed no significant effects on the turbine thrust or power coefficients as the turbulence intensity was increased. They reasoned that this was due to the fact that 80 % of the generated rotor torque is generated by the outer 60 % of the blade where the effective turbulence intensity that the blade experiences is lower due to the higher velocity of the blade tip. However, the integral length scales used were very small in comparison to the turbine diameter, which is not representative of a tidal site where length scales would be comparable to the turbine diameter or even greater.

Maganga et al. (2010) performed experiments on a model three-bladed tidal turbine in a circulating water channel. Turbulence was controlled by introducing honeycomb flow straighteners which reduced the ambient turbulence intensity from 15 % to 3 %. The

integral length scales were not reported, but it is likely that without the flow straighteners there would be large turbulent structures, potentially as large as $\ell_x/D \approx 4$ where the eddies are constrained by the size of the flume cross-section. With the flow straighteners installed the turbulent structures are likely to be smaller as they would break up the larger turbulent eddies. The results of this study showed that the thrust and power coefficients reduced by approximately 10 % as the turbulence intensity increased from 3-15 %, and the magnitude of thrust fluctuations were doubled.

While the studies of Sicot et al. (2006) and Maganga et al. (2010) show different effects of turbulence on turbine thrust, they were carried out with different scales of turbulence. Sicot et al. (2006) only considered the effects of small scale turbulence with $\ell_x/D < 0.05$, whereas Maganga et al. (2010) used turbulent flows with larger scales of turbulence (although length scales were not reported). Turbine rotors are therefore sensitive to ℓ_x/D ratios, just as solid discs are, and further investigation is required.

Experimental investigations using model turbines are expensive and require large circulating flumes or wind tunnels to achieve suitably low blockage ratios. Myers & Bahaj (2010) used porous disc rotor simulators to represent the far wake of a tidal turbine for small scale experiments. Their justification for using porous disc rotor simulators were:

- Thrust coefficients of porous discs and turbine rotors are comparable. Therefore results from small scale investigations using porous discs could be scaled to real turbine installations.
- Using small scale turbine rotors would be impractical due to issues with scaling the Reynolds number of the turbine blades when maintaining the tip speed ratio of the rotor.
- Porous discs dissipate turbulent kinetic energy of the flow by generating small scale turbulence that decays, and eventually dissipated as heat through the energy cascade, section 2.2.1. Differences between rotors and porous discs are therefore likely in the near wake region only, up to 4-5 diameters downstream. Beyond this region in the far wake studies on wind and tidal turbines show no major differences between the wakes of rotors and porous discs.

Small scale experiments using porous discs with porosities of 50 % and 14 % were performed by Sun (2008) in a water channel, in a towing tank, and in a towing tank with a turbulence grid generator upstream of the disc. The turbulence characteristics were not reported but the towing tank would be a zero turbulence case while both water channel and grid generated turbulence would be high turbulence cases, but the intensities and length scales of these flows were not reported. For the 50 % porous disc the thrust coefficient was 3.5 % lower for the zero turbulence case and larger variations of over 10 % were recorded for the 14 % porous disc. However, the thrust of the 14 %

porous disc was lower in the water channel than the zero turbulence case. This suggests the thrust coefficient of porous discs are also sensitive to the turbulence characteristics and further investigation is required.

Overall the thrust coefficients of turbine rotors and porous discs are sensitive to the turbulence conditions of the incoming flow. However, little consideration has been made to characterising the free-stream turbulence so effects of turbulence intensities and ℓ_x/D ratios are unclear. Further work is required to investigate the effects of both turbulence intensity and integral length scales on the thrust of turbine rotors and porous disc rotor simulators. The next section discusses the effects of turbulence on the wake profiles behind turbines and porous discs.

4.2 Effects of turbulence on the wake

The previous sections have considered how turbulence affects the thrust loads on turbine rotors, porous disc rotor simulators and solid discs. However, turbulence can also affect the wake recovery; increasing turbulence intensity speeds up the wake recovery (Sforza et al. 1981, Macleod et al. 2002, Sun 2008, Nishino & Willden 2012). Comparisons have been made between the measured centreline velocity deficit behind model turbine rotors and porous disc simulators with thrust coefficients of approximately 0.9 and with different turbulence intensities as shown in figure 4.2, although the integral length scales were not considered. It can be seen for each individual study that increasing the turbulence intensity reduces the velocity deficit in the wake, particularly for Sun (2008), Mycek et al. (2013), Myers et al. (2013). However, cross-comparing between different studies shows a large overall variation in the measured velocity deficits. At $x/D = 4$ the variation in velocity deficit is from ≈ 0.1 (Mycek et al. 2013) to ≈ 0.6 (Myers et al. 2013) highlighting the sensitivity of the wake to different flow conditions.

For a zero turbulence case Sun (2008) reports a velocity deficit of 0.68 at $x/D = 3$ reducing to 0.58 at $x/D = 4$ while Krogstad & Eriksen (2013) reports a velocity deficit increasing from 0.33 at $x/D = 3$ to 0.38 at $x/D = 4$ with a very low turbulence intensity of 0.3 %. While the number of data points are limited, it is clear that these authors have found very different trends in the wake. However, it is likely that the differences may be explained by considering the blockage ratio. Sun (2008) used a low blockage ratio of 0.4 %, but the blockage ratio of Krogstad & Eriksen (2013) was 12 %. The effect of higher blockage forces more fluid through the rotor increasing the wake velocities, thus reducing the velocity deficit (Nishino & Willden 2012).

Considering the two cases of Mycek et al. (2013) and Myers et al. (2013) with turbulence intensities of ≈ 5 % and ≈ 15 % one would expect to see little difference in the wake profiles. But the velocity deficit reported by Mycek et al. (2013) is significantly lower than reported by Myers et al. (2013). Although the blockage ratio was lower for Myers et al.

(2013), < 2 % compared to < 5 % for Mycek et al. (2013), only small variations would be expected (Whelan et al. 2009). The differences in wake may therefore be attributed to differences between the wake of a porous disc used by Myers et al. (2013) and a turbine rotor used by Mycek et al. (2013), or differences in the turbulence characteristics of the free-stream flow. The first point may be addressed by consideration of the experiments by Chamorro & Porté-Agel (2009) on a model turbine with blockage ratio of approximately 5 % and turbulence intensities of 7-11 %. Comparing the velocity deficit for turbulence intensities of 5 % for Myers et al. (2013) and 7 % for Chamorro & Porté-Agel (2009) shows a very close agreement in the far wake. In the near wake the velocity deficit differs with higher deficits for the porous disc, but this case had a slightly lower intensity so it would be expected to have a higher deficit. Also, some variation is to be expected in the near wake region due to the assumptions behind the use of porous disc rotor simulators (Myers & Bahaj 2010). Due to a process of elimination, the differences in velocity deficit must be due to the characteristics of the free-stream flow. The integral length scales are not reported by Mycek et al. (2013), but as previously discussed, it seems likely that the high intensity case will have large length scales while the low intensity case will have small length scales due to the flow straighteners. In contrast the high intensity case of Myers et al. (2013) had small integral length scales of $\ell_x/D \approx 0.5$ while their low intensity case had large integral length scales of $\ell_x/D \approx 1.5 - 2$. Due to the limited information presented it is not possible to draw a firm conclusion but it seems likely that the wake recovery is sensitive to the integral length scale of the ambient flow.

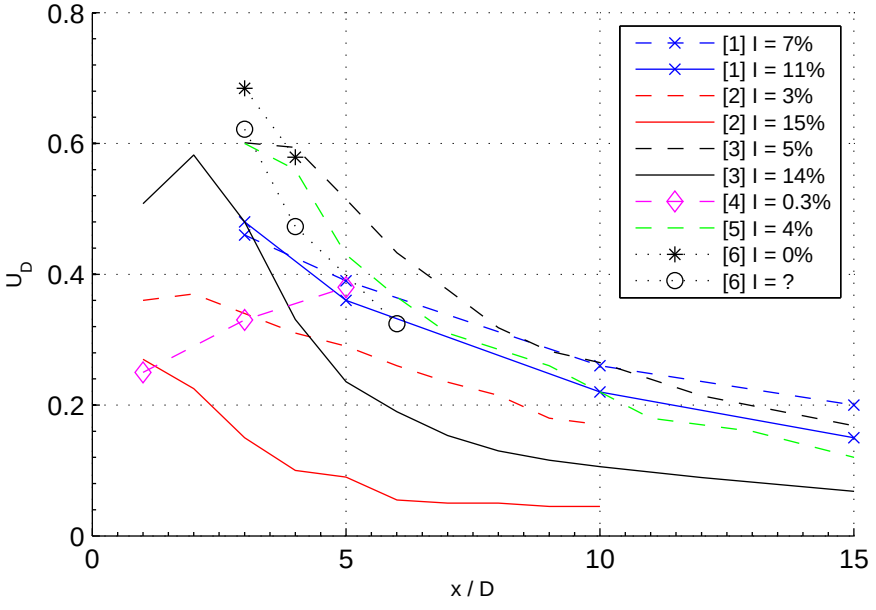

Figure 4.2: Centreline velocity deficit from experiments with model rotors and porous disc rotor simulators with thrust coefficients of approximately 0.9. [1]: Chamorro & Porté-Agel (2009) [2]: Mycek et al. (2013) [3]: Myers et al. (2013) [4]: Krogstad & Eriksen (2013) [5]: Myers & Bahaj (2010) [6]: Sun (2008)

Espana et al. (2012) considered the effects of integral length scale on the wake of solid and porous discs in a simulated atmospheric boundary layer. It was found that the wake meandered with integral length scales of ten times the diameter. On comparison with grid generated turbulence with scales of $0.1 < \ell/D < 0.3$ the wake did not meander. While this study demonstrates the phenomena of wake meandering only occurs for very large scale turbulent structures, the effects of body-scale turbulence were not considered on the velocity deficit behind the disc. It is important to consider the velocity deficit profile as it dictates the spacing of devices within an array. If the wake recovers faster then turbines may be positioned closer together within an array and the power output per unit area increased. This was observed in actuator-disc RANS simulations by Harrison (2011) who found the power output of an array increased when the turbulence intensity of the ambient flow was increased.

Ainslie (1986) developed a numerical wake model that accounts for ambient turbulence intensity of the flow and predicts the wake profile for array planning. The model is based on the assumption that the turbulence energy in the ambient flow may be added to the turbulence energy generated by the turbine as shown in equation 4.1.

$$u_w'^2 = u_\infty'^2 + u_t'^2. \tag{4.1}$$

While this method has been shown to produce reasonable agreement with some experimental data the assumption of adding turbulence of the ambient flow with the turbine generated turbulence may be an over simplification as the integral length scale is not considered. Jonsson et al. (2011) developed an analytical model that considers the integral length scale of the ambient flow. The model simplifies the problem of tidal turbulence by assuming isotropic turbulence, but considers both turbulence intensity and integral length scale. Their model assumes that the wake initially grows linearly with distance downstream and later at a rate dictated by the turbulence intensity and integral length scale of the ambient flow. Comparisons were made to an experiment with turbulence intensity of 18 % and integral length scale of 0.2 m, which corresponded to a length scale to disc diameter ratio of 4. The centreline velocity deficit predicted by the model was compared to the experimental results and it was found that the model produced reasonable agreement for 3-6 diameters downstream. However, more significant differences existed outside of this region and only a single case has been considered, for a flow with one set of turbulent characteristics. Due to the complex nature of a tidal flow these simple analytical models do not really capture the full effects of turbulence, a 3D model is therefore required.

CFD simulations with actuator discs are commonly used to investigate turbine wakes as they can provide information on the whole flow field at reduced cost and time compared with experiments (Macleod et al. 2002, Sun et al. 2008, Harrison et al. 2010, Turnock et al. 2011, Nishino & Willden 2012, Malki et al. 2013). Refer to chapter 3 for further

details on CFD techniques for modelling turbines. Nishino & Willden (2012) used RANS actuator disc simulations to investigate the effects of free stream turbulence and blade induced turbulence on the thrust and power of a tidal turbine. Two different turbulence levels were used at the inlet corresponding to a high and low turbulence level with 10 % and 0.1 % turbulence intensity respectively. A length scale of 0.1 times the disc diameter was used for both cases. Due to turbulence decay from the inlet the turbulence intensity at the disc reduced to 5.7 % for the high turbulence case, which is lower than expected for a tidal flow as discussed in section 2.5. A uniform actuator disc was used with the $k - \epsilon$ turbulence model. Turbulence sources were calculated using two parameters; the ratio of energy converted to turbulence to the energy extracted from the flow by the disc, and a characteristic length scale of the blade induced turbulence. As with the model of Ainslie (1986) it was assumed that the energy of the ambient turbulence may be added to the turbulence generated by the disc to give the total turbulence.

Their results show that increasing the characteristic length scale of the device generated turbulence increases the maximum power coefficient of the disc, but the effects of the characteristic length scale on the wake were not considered. The results show the wake recovery is faster with high ambient turbulence, which is in agreement with Mycek et al. (2013), Myers et al. (2013). Their results also showed that the thrust and power coefficients slightly increased with increasing levels of ambient turbulence. The cause of this was postulated to be due to an increase in shear stress between the free-stream bypass flow and the wake causing a greater proportion of the upstream flow to pass through the disc. As the axial induction factor is held constant the thrust and power coefficients must increase, as found by dividing equation 3.15 by 3.16, $a = 1 - C_P/C_T$. This work highlights the importance of both ambient and device generated turbulence on the wake and performance of an actuator disc. However, the effects of ambient turbulence are in contrast to Mycek et al. (2013) who found the thrust and power decreased with an increase in turbulence. It is possible that this difference can be explained by considering the integral length scale of ambient turbulence. The effects measured by Nishino & Willden (2012) were for small scale turbulence, while it is likely that larger scales were present in the work by Mycek et al. (2013). Further investigation is therefore required to identify the effects of integral length scale on turbine performance and wake profiles.

The sensitivity of actuator disc wakes to the ambient flow conditions was further demonstrated by Mason-Jones et al. (2013) who investigated the effects of a velocity profile on the power coefficient of a three bladed tidal turbine. A RANS simulation with full rotor turbine model was used with both a uniform inlet and a boundary layer velocity profile taken from ADCP site measurements. The results show a reduction in power coefficient from 0.4 to 0.34 when the turbine operates in a boundary layer velocity profile. This is due to the variation in velocity across the disc which also caused asymmetric loading of the blades. However, no wake measurements were presented. Further sensitivities were reported by Masters et al. (2013) who used RANS simulations with an accelerating flow.

It was found that the wake recovery is increased when the actuator disc is located in an accelerating flow. However, in a RANS simulation the effects of turbulent length scale on an actuator disc may not be captured as the turbulence is modelled. Changing the characteristic length scale only effects the rate of turbulence dissipation (as shown in equation 3.6), therefore no spatial structure is resolved. An LES model would therefore be required to resolve the structure of the larger energy containing eddies to further the understanding on the interaction of turbulence with an actuator disc (Batten et al. 2013). However, these studies do further highlight the sensitivity of turbine performance and wake profiles to the ambient flow conditions.

4.3 Summary

The effects of turbulence intensity and length scale on the thrust of solid discs, porous discs and turbine rotors is little understood. Previous studies suggest that turbulence intensity acts to increase thrust on a solid disc and there is a strong dependence on integral length scale. However, the effects were measured for a limited number of cases and a clear relationship has not been found. Similar trends have been observed for porous discs used to simulate tidal turbines in small scale experiments, although the effects of integral length scale have not been considered. Finally, conflicting results have been found for the affects of turbulence on a turbine rotor, some suggesting turbulence has little affect while others suggest increasing turbulence reduces thrust and power by approximately 10 %. It was speculated that these differences were due to variations in integral length scales in the flows, but specific values were not presented. Further work is therefore required to understand the effects of turbulence intensity and integral length scale on the thrust of solid discs, porous discs, and turbine rotors.

Considering investigations using porous discs and turbine rotors it is clear that their wakes are very sensitive to the turbulence characteristics. Each study showed a reduction in velocity deficit with an increase in turbulence intensity. However, discrepancies existed when cross-comparing results from different authors and the variations attributed to differences in flow conditions, in particular the integral length scale. It was also shown how the wake of a porous disc meandered for very large scale turbulence ($\ell_x/D = 10$) but the effects of body scale turbulence were not considered.

Analytical wake models were found to be too simplistic to enable the investigation of turbulence intensity and integral length scale requiring CFD models which have been used to investigate the wakes of actuator discs. Their findings agree with the experimental results where increasing the turbulence intensity reduces the velocity deficit and increases thrust. They have also shown how the wakes of actuator discs are sensitive to other flow features. Thrust was reduced when a turbine operates in a boundary layer velocity profile compared to a uniform flow and in an accelerating flow the velocity deficit

is reduced and wake recovery is faster. It was also shown that increasing the device generated turbulence, marginally increased thrust and further reduced the velocity deficit. However, the effects of integral length scale were not fully considered and an LES model would be required to investigate the interaction of different turbulent eddy sizes.

Overall, the thrust and wakes of porous discs and turbine rotors are very sensitive to the turbulence characteristics of the ambient flow. However, it remains unclear how the integral length scale or turbulence intensity affects the thrust and wake. This is important to allow accurate predictions of performance and wake profiles for the optimisation of tidal turbine arrays. The next chapter defines the problem statement, aim, and objectives of this study.

Chapter 5

Problem Statement

The previous chapters have presented relevant background theory and the current state-of-the-art on turbulence in tidal flows, CFD modelling of tidal stream turbines, and the effects of turbulence on turbine rotors, porous disc simulators, and solid discs.

It was shown that tidal flows are very turbulent with a broad range of scales and intensities of around 10 %, but the characteristics are site specific. Few sites have been fully investigated and further research is required in this area. However, this is beyond the scope of this investigation due to the large costs involved. Grid generated turbulence is commonly used in wind tunnel studies to generate approximately isotropic turbulence with intensities and integral length scales proportional to the grid dimensions, this method can therefore be used to generate flows with different turbulence characteristics.

CFD simulations using RANS and LES turbulence models have been used with actuator disc turbine representations and found to be in good agreement with experimental data. It was also shown that small scale experiments and simulations are representative of full scale tidal sites. A turbulence source in actuator disc RANS simulations is required to improve agreement with experimental data to account for the turbulence generated by the turbine, but the characteristic length scale of the source has not been considered. It has also been shown that the ambient turbulence intensity affects the wake recovery behind an actuator disc, but the effect of the integral length scale has not been considered and the inflow turbulence characteristics are often poorly reported in both experiments and numerical simulations. RANS models cannot capture effects of integral length scale as simulations are steady state and changes in the characteristic length scale simply change the dissipation rate. They can however be used to identify any sensitivities to assumptions of the characteristic length scale. A transient LES model could then be used which directly resolves the larger energy containing eddies allowing the interaction of turbulent eddy size on actuator discs to be investigated. For investigating the effects of turbulence a uniform actuator disc with turbulence source is beneficial as BEM models are limited by the availability of lift and drag data sets of the turbine blades for different

turbulence conditions. By applying a turbulence source to the actuator disc the effects of device generated turbulence may be investigated.

The effects of turbulence on the performance of tidal stream turbines, or porous disc rotor simulators is unclear from the literature. From the research on solid discs it seems likely that turbulence could have a significant effect with variations in thrust of $10 - 20$ %. In order to simplify the problem the investigation on the effects of integral length scale and turbulence intensity will be performed with isotropic turbulence that can be generated with a grid. This allows the specific effects of integral length scale and turbulence intensity to be isolated without further complexities from anisotropic stresses. Understanding the effects of grid generated turbulence on the thrust of a porous disc rotor simulator is important as turbine power may be estimated from the measured thrust in small scale experiments. A new method of generating isotropic turbulence in LES models based on grid generated turbulence has been proposed. This method allows turbulence with different integral length scales and turbulence intensities to be generated. An extension of this method has been proposed to produce turbulence in an actuator disc for LES models. The combination of these new techniques would allow the effects of turbulence on the wake of an actuator disc to be investigated.

5.1 Aim

The aim of this research project is to investigate the effects of grid generated turbulence on the thrust and wake of an actuator disc representation of a tidal turbine. Grid generated turbulence will be used so the integral length scale and turbulence intensity may be controlled to isolate the effects of these turbulence parameters on the thrust and wake profile behind an actuator disc. This is important as turbines operate in a highly turbulent environment, but the effects of these extreme turbulent conditions are unclear. Understanding the effects of turbulence will be beneficial for turbine developers as it will allow further optimisation of tidal turbines and arrays of devices that may be tuned to the specific turbulent conditions.

5.2 Objectives

The aim will be achieved by breaking the investigation down into a set of objectives that are described below. Each of the 5 objectives relates to the results chapters 6-10.

- Investigate the sensitivity of actuator disc RANS simulations to the characteristic length scale used for the turbulence source.

- Investigate experimentally the effects of turbulence intensity and integral length scale on the thrust of porous disc rotor simulators in a water flume with grid generated turbulence.
- Develop an LES inlet that generates isotropic turbulent flows with integral length scales and turbulence intensities that may be controlled.
- Develop an actuator disc model with added turbulent source for LES and investigate the effects of device generated turbulence.
- Investigate the effects of the isotropic turbulence intensity and integral length scale on the wake behind an actuator disc using the developed LES model.

Chapter 6

RANS modelling of an actuator disc: Influence of characteristic length scale assumptions

6.1 Introduction

The use of actuator disc RANS models to simulate tidal stream turbines was discussed in section 3.5.3. Sun (2008) and Macleod et al. (2002) showed how the ambient turbulence levels in actuator disc RANS simulations affected the wake profile. Increased ambient turbulence results in greater mixing between the free stream and wake resulting in faster wake recovery, as postulated by Sforza et al. (1981).

The agreement of actuator disc RANS simulations with experimental data has been improved with the addition of a turbulent source at the disc (Harrison 2011). However, the characteristic length scale of this turbulent source has not been considered, and also likely to affect the wake recovery.

This chapter considers the the sensitivity of actuator disc RANS simulations to assumptions in the characteristic length scale of the turbulence source and was presented at the 9th European Wave and Tidal Energy Conference (Blackmore et al. 2011).

6.2 Experimental Validation Data

Experimental data used for validation was obtained in a circulating water channel measuring 21 m in length, 1.37 m wide, and 0.3 m deep at the University of Southampton. Porous disc rotor simulators of 0.1 m diameter were used to represent a turbine with

thrust coefficient of 0.86. Thrust forces were measured using load cells and flow velocities measured using an Acoustic Doppler Velocimeter (ADV) at a sampling frequency of 50 Hz. Full details of the experimental procedure can be found in Myers & Bahaj (2010).

6.3 Numerical Method

The OpenFOAM® SimpleWindFoam steady state RANS solver was used with a modified $k-\epsilon$ turbulence model. The solver is for single phase incompressible fluid flows and uses the SIMPLE algorithm for pressure velocity coupling. The solver allows an actuator disc momentum source term to be specified, and added to the actuator disc region. A modified $k-\epsilon$ turbulence model was used that allows a uniform fixed value turbulence source term to be added to the actuator disc region. Combinations of central differencing and Van Leer TVD schemes were used for discretisation of the equations (OpenCFD 2012).

6.3.1 Pre-processing: meshing, boundaries and inlet values

The computational domain is shown in figure 6.1. Only half the flume was modelled, due to symmetry, to reduce computational resources.

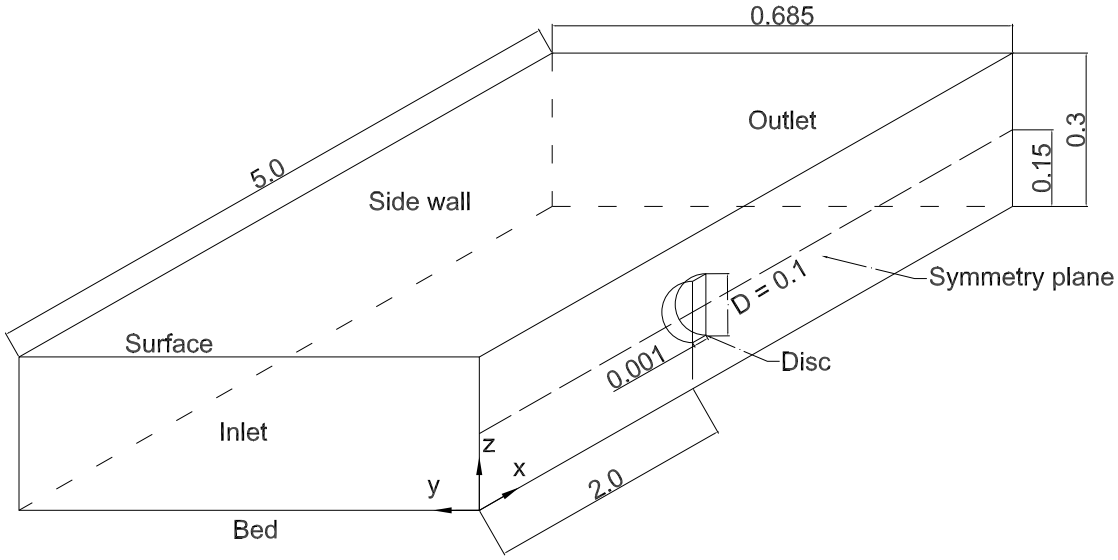

Figure 6.1: Computational domain and principle dimensions, in meters.

Gmsh 2.5 finite element grid generator was used to produce a structured hexahedral mesh. Three meshes were produced to assess the mesh independence with the following cell counts:

- Course $\approx 0.3 \times 10^6$ cells.

- Medium $\approx 1.0 \times 10^6$ cells.
- Fine $\approx 3.8 \times 10^6$ cells.

Inlet velocity and turbulent kinetic energy profiles were specified by fitting a logarithmic profile to the experimental data. The inlet turbulence dissipation was calculated using equation 3.6 that requires the specification of a turbulence characteristic length scale. A characteristic length scale of one third the channel depth was used based on the findings of Blackmore et al. (2011).

The boundary conditions of the computational domain are shown in table 6.1.

Table 6.1: RANS Computational domain boundary patches

	Field			
Boundary	U	P	k	ϵ
Inlet	Inlet Profile	Zero Gradient	Inlet Profile	Inlet Profile
Outlet	Zero Gradient	Fixed Value	Zero Gradient	Zero Gradient
Symmetry Plane	Symmetry Plane	Symmetry Plane	Symmetry Plane	Symmetry Plane
Bed	No slip	Zero Gradient	Wall function	Wall function
Side Wall	No slip	Zero Gradient	Wall function	Wall function
Surface	Free slip	Free slip	Free slip	Free slip

6.3.2 Actuator disc

Refer to section 3.5 for details of how the actuator disc turbine representation is implemented for RANS simulations.

6.3.2.1 Turbulence source

The magnitude of the turbulent intensity at the actuator disc was calculated using equation 3.21. Equation 3.5 was then used to calculate the magnitude of the turbulent kinetic energy source. The turbulence dissipation source was calculated using equation 3.6, requiring the specification of a characteristic length scale of the turbulent source. The sensitivity of RANS actuator disc simulations to turbulent source characteristic length scale, L_s, was investigated using two values listed below:

1. L_s = Hole diameter of the porous discs used for experiments (5 mm).

2. L_s = Half the hole diameter of the porous discs used for experiments (2.5 mm).

The next section presents the results from this study.

6.4 Results

Stream wise velocities (U_x) have been normalised using the average velocity over the range $0.5 < z/D < 2.5$: U_∞=0.329 m/s for experimental data, U_∞=0.333 m/s for the CFD model.

6.4.1 Mesh independence

A mesh independence study was performed to demonstrate the results obtained from the RANS simulation are independent of the computational mesh. The results show little variation in the velocity profiles for the three meshes, figure 6.2. The medium mesh with $\approx 1 \times 10^6$ cells was used for this investigation with improved computational efficiency over the fine mesh.

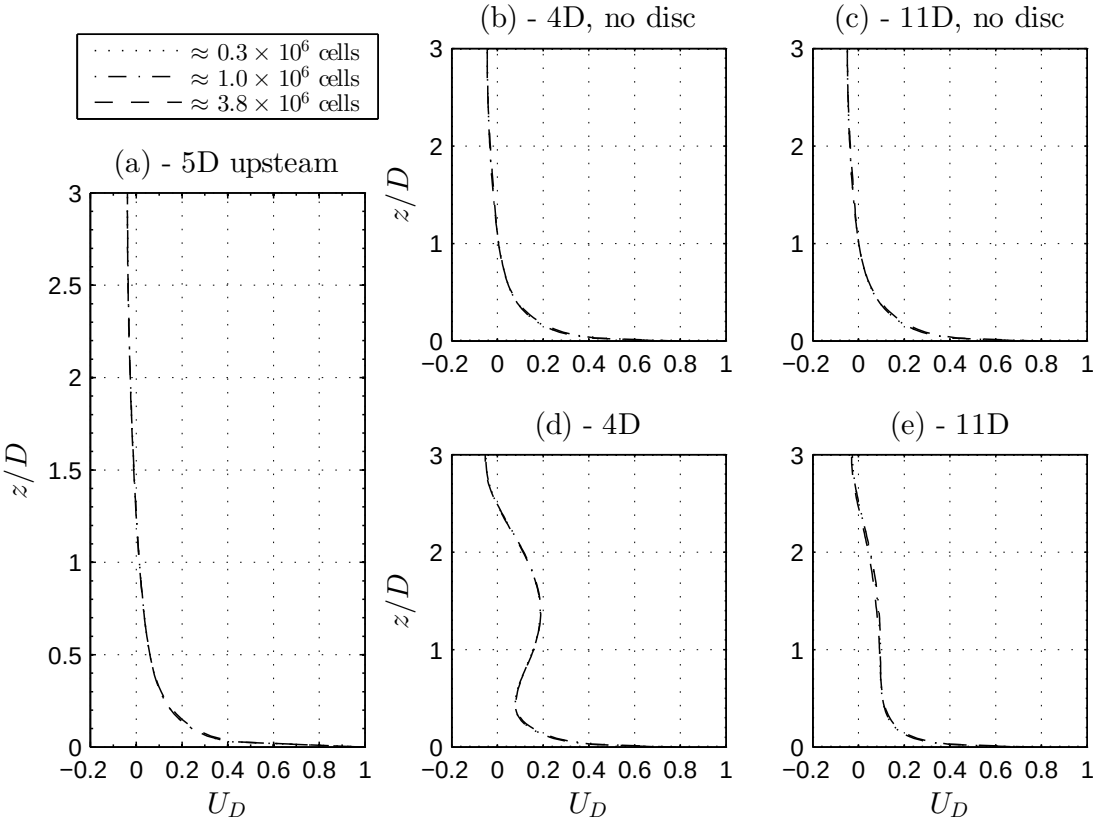

Figure 6.2: Velocity deficit profiles with and without actuator disc for different mesh densities. (a) - 5D upstream of disc; (b)&(d) - 4D downstream; (c)&(e) - 11D downstream; (b)&c - no disc; (d)&(e) - with disc.

6.4.2 Turbulent Source Characteristic Length Scale

It can be seen in figure 6.3(a) that the velocity deficit is underestimated without a turbulent source at the actuator disc as found by Harrison (2011). The inclusion of a turbulent source with $L_s = 5$ mm significantly improved agreement with the experimental data. Reducing the turbulent source characteristic length scale to $L_s = 2.5$ mm reduces agreement and the wake recovery is slowed. This is due to an increase in turbulence dissipation as the turbulent source length scale is reduced. This reduces the turbulence intensity which reduces the turbulent mixing and delays the wake recovery. This can be seen in figure 6.3(b) where the turbulence intensity is lower for the smaller turbulent source characteristic length scale. However, for both cases where a turbulent source is added the turbulence decays rapidly to below the case with no turbulent source.

Figure 6.4(a) shows the velocity deficit profiles downstream of the actuator disc. It can be seen that the velocity deficit is under estimated with no turbulent source term. A characteristic length scale of $L_s = 5$ mm shows very good agreement with the experimental data in both the near and far wake. However, as before it can be seen in figure 6.4(b) that the turbulence intensity is underestimated in the near wake.

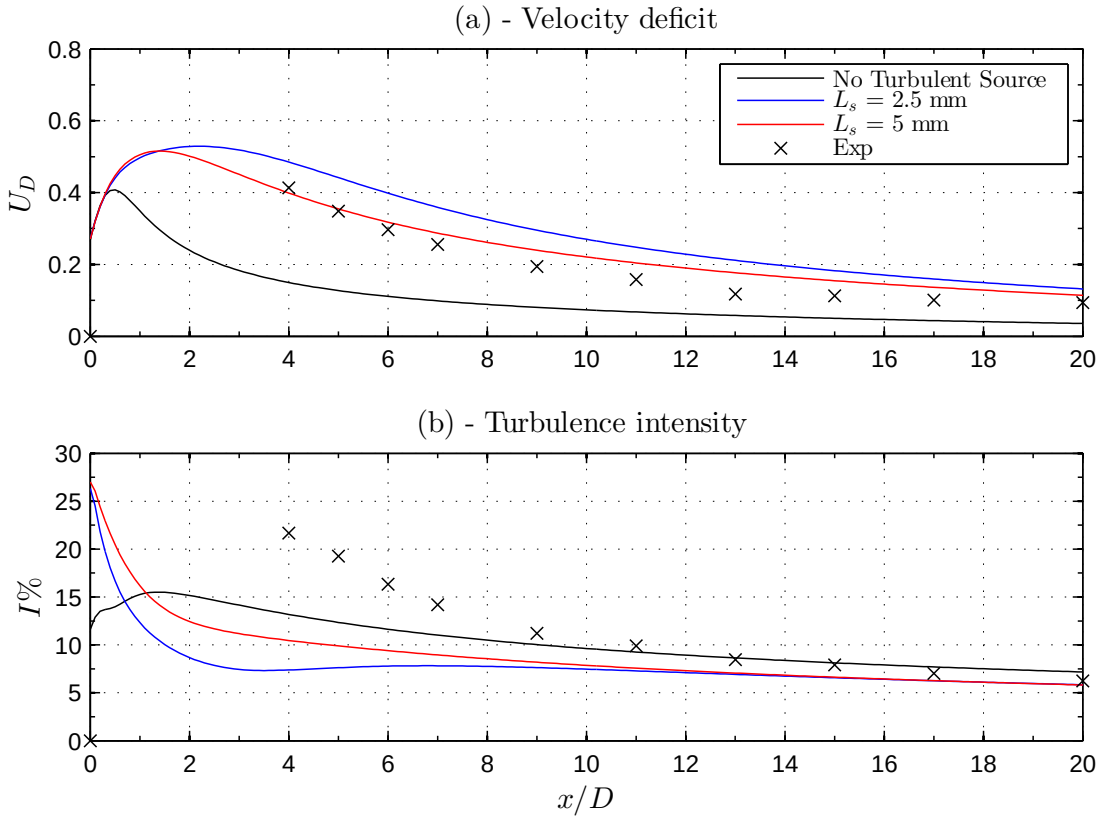

Figure 6.3: Centreline velocity deficit and turbulence intensity profiles for three turbulent source values.

A possible reason for this could be that the turbulent source added is an under estimate as derived from an empirical expression (equation 3.21) used for wind turbines. As the experiments were performed with porous discs which dissipate energy through the generation of small scale turbulence, representing the energy extraction by a turbine, the turbulence intensity close to the porous disc would be higher than that measured behind a wind turbine rotor. Further increasing this source would improve agreement in the near wake, which combined with an increase in dissipation would maintain agreement in the far wake.

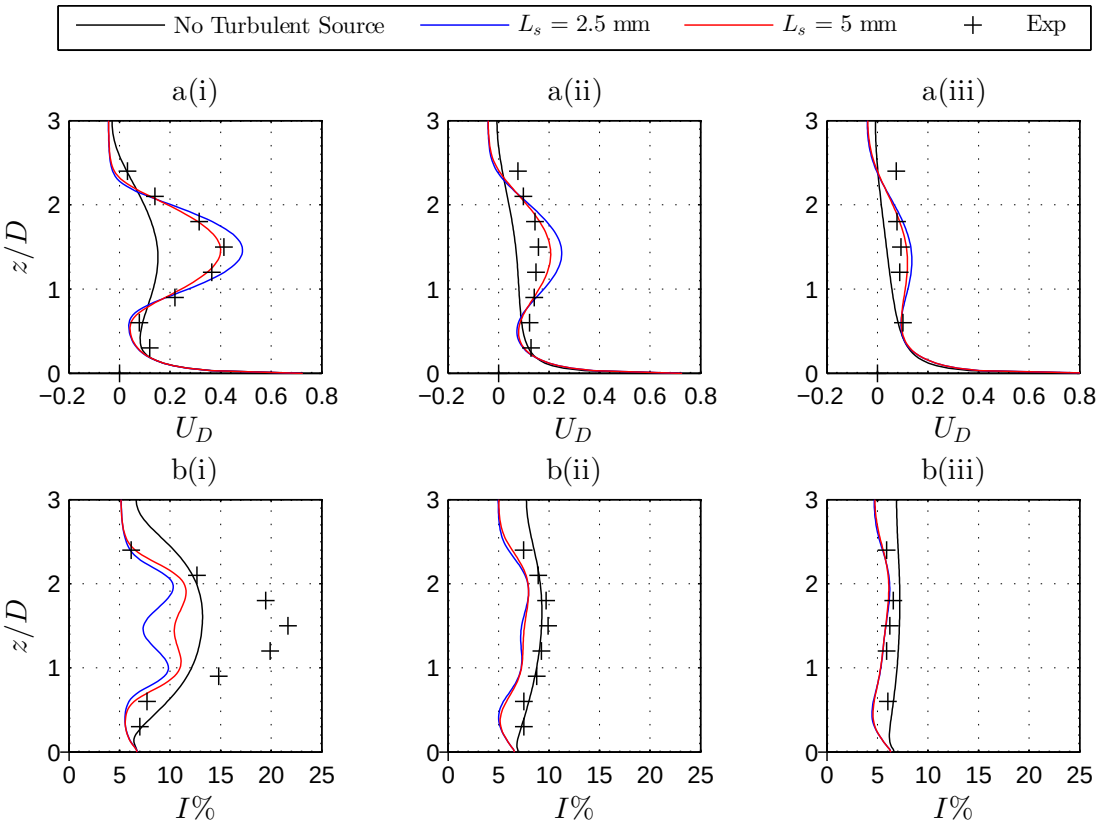

Figure 6.4: Velocity deficit (a) and turbulence intensity (b) vertical profiles downstream of actuator disc. (i) - 4D downstream; (ii) - 11D downstream; (iii) - 20D downstream.

6.5 Summary and implications

It has been shown that actuator disc RANS simulations are sensitive to the characteristic length scale assumed for the turbulence source. With no turbulence source the velocity deficit in the near wake was severely underestimated, while a small length scale of the turbulence source resulted in over estimates of velocity deficit with delayed wake recovery. A characteristic length scale equivalent to the porous disc hole diameter (L_s = 5 mm) showed the best agreement, but the turbulence intensity in the near wake was still underestimated. Further increasing the turbulence source kinetic energy would improve agreement in the near wake, while a corresponding increase in dissipation would maintain agreement in the far wake.

These results demonstrate the significance of turbulence on the wake recovery of a turbine. Previously only the turbulence intensity had been considered, but these results show that the characteristic length scale also significantly affects the wake of a turbine. However, as these RANS simulations are steady state only the mean turbulence characteristics have been considered. Changing the characteristic length scale only changes the dissipation rate as no turbulent structure is resolved. To further this investigation

transient simulations are required that can resolve the structure of turbulence to better understand how turbulent structures interact with an actuator disc.

Chapter 7

Influence of turbulence on the thrust of turbine simulators

7.1 Introduction

The previous chapter demonstrated that both turbulence intensity and length scale have a significant effect on the wake profile behind an actuator disc. The aim of this chapter is to investigate the effects of turbulence on the thrust of a porous disc rotor simulator, and more generally on a solid disc. As discussed in chapter 4, it is commonly assumed that turbulence acts to increase the 'effective' Re which leads to the general assumption that disc thrust is not strongly effected by turbulence (e.g. Massey & Ward-Smith 2006). However a few studies suggest this may not be the case and turbulence may alter the thrust loads (Schubauer & Dryden 1935, Craze 1977, Bearman & Morel 1983). This is important as load predictions made from small scale experiments with low levels of turbulence may be underestimated leading to device failure when operating in highly turbulent conditions as found in a tidal flow, see section 2.5.

The effects of turbulence intensity and length scale on the drag of solid and porous discs is little understood. Previous studies suggest that turbulence intensity acts to increase drag on a solid disc and there is a strong dependence on turbulence length scale (Bearman & Morel 1983). However, the effects were measured for a limited number of cases and a clear relationship has not been found. Porous discs have been used to simulate wind and tidal turbines in small scale experiments. It is possible to estimate the power output of a device from the measured thrust on the porous disc. Understanding the effects of turbulence on the thrust of a porous disc is therefore important to allow realistic predictions to be made from small scale experiments. The aim of this chapter is to investigate the effects of turbulence intensity and integral length scale on the thrust of solid and porous discs.

The investigation was performed in a gravity fed flume and different turbulent flow conditions were generated using grids. Although the characteristics of grid generated turbulence will differ from the characteristics of a natural tidal flow, it allows the specific turbulence characteristics to be controlled, simplifying the problem (Murzyn & Belorgey 2005). Discs with different porosities and diameters were installed in the turbulent flow and the thrust force measured. This chapter has been published in the journal Experiments in Fluids (Blackmore, Batten, Műller & Bahaj 2013).

7.2 Experimental configuration and method

The experimental method is shown schematically in figure 7.1. Turbulent structures proportional in size to the grid bars are generated whose turbulence intensity decays with distance downstream from the grid. Discs of different diameter and porosity were installed and the thrust force measured under different turbulent conditions.

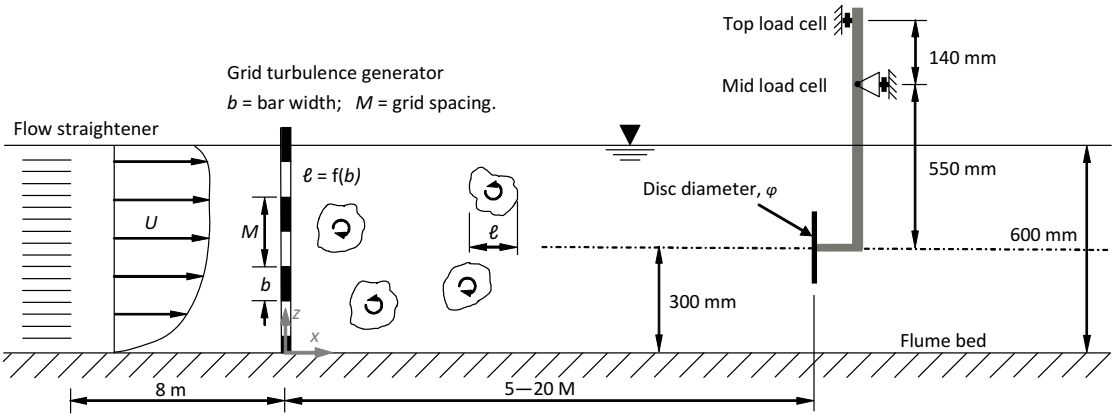

Figure 7.1: Schematic showing the experimental method. Mid plane cross section of the tank showing Grid-B turbulence generator and disc mounted on the measurement load cell rig. Not drawn to scale.

7.2.1 Test facility and grid layout

The investigation was performed at the indoor flume at the Technical University of Braunschweig, Germany. The flume is 36 m long, 2 m wide, 0.6 m deep, and tilted 0.02 % to achieve uniform flow conditions with constant depth and velocity profile along the flume. Three different turbulent grids were installed 8 m downstream of the flume flow straighteners. The use of grids to generate turbulence of different length scales and intensities is well understood, see section 2.4. Almost homogeneous and isotropic turbulence with a range of turbulence intensities and length scales may be created by changing the grid size and varying the distance downstream of the grid (Mohamed & LaRue 1990, Krogstad & Davidson 2009). Each grid had an open area ratio of 0.56 and arranged with square pattern, further details are in table 7.1. The coarsest grid

($M = 300$ mm) required only two horizontal bars in order to generate length scales of $\approx 1/4$ the depth and of the order of a disc diameter. A half bar was used at the flume bed and free surface as indicated in figure 7.2 and the schematic of figure 7.1 for the $M = 200$ mm grid.

The coordinate system is defined from the center of the tank at the base of the grid, x is stream-wise direction with $x = 0$ at the grid, y is the flume transverse with $y = 0$ on the centerline of the flume, and z is height above the flume bed with $z = 0$ on the flume bed.

Table 7.1: Parameters for the three grids used to generate turbulence

Spacing, M (mm)	Bar width, b (mm)	Number bars, vertical / horizontal
100	25	20 / 7
200	50	10 / 3
300	75	7 / 2

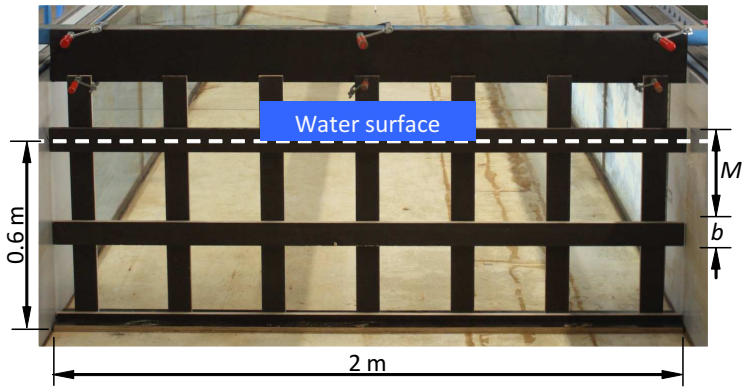

Figure 7.2: Photograph of M=300 mm grid, showing the first horizontal installed at the flume base as a half width. The upstream water level depth was set at 600 mm, half way up the third horizontal bar.

7.2.2 Choice of discs

Seven discs were used to perform the investigation, details of their porosities and diameters are shown in table 7.2. The porosity, or open area ratio, (θ) is defined as the ratio of open area to total disc area. The hole pattern used for the porous discs was chosen to maintain approximately uniform porosity across the disc radius. The hole pattern of the smaller discs was kept the same as the larger discs and all discs laser cut from 2 mm stainless steel. Full details of the hole patterns used are provided in appendix B; table B.1 details the hole patterns, figure B.1 shows a photo of disc 4 attached to the

Table 7.2: Details of the seven 2 mm thick discs used in the experiments

Disc ID	Diameter, D (mm)	Porosity, θ	Number of holes
1	150	0, solid, chamfered edge	0
2	150	0, solid, square edge	0
3	150	0.4	249
4	150	0.6	375
5	108	0, solid, square edge	0
6	108	0.4	129
7	108	0.6	193

mounting beam. The 6 mm diameter holes were evenly spaced around each pitch circle diameter.

The 150 mm chamfered, sharp, edge disc was used to provide a comparison between a disc with square edges. It was found that drag on the chamfered disc was 1.7 % lower than the square edge disc. The chamfered disc was used for the remaining investigation to allow direct comparison with previous studies where sharp edge discs were used.

7.2.3 Velocity and turbulence data reduction and experimental accuracy

Two Nortek Vectrino+ Acoustic Doppler Velocimeters (ADV's) were used with a sampling frequency of 50 Hz for all tests, as above this frequency the signal to noise ratio (SNR) reduced to unacceptable levels (SNR < 15). A velocity correction filter was used to filter all raw ADV data using the method described in (Cea et al. 2007). Typically less than 1.5 % of the data points were removed and replaced by the filter to correct for erroneous spikes introduced by the ADV.

The choice of sample period, S_t, and error estimation was investigated using a 90 minute sample recorded in the flume with no grid installed. Mean velocities, turbulence intensities, and integral length scales were calculated for sample lengths ranging from 1-90 minutes. Figure 7.3 shows the convergence of turbulence intensity. It can be seen that as the sample period increases, the turbulence intensity converges on a value of approx 5.13% with little variation for samples greater than 20 minutes.

The sample period was chosen to be 6 minutes as a compromise between accuracy and available flume time. Turbulence characteristics were then calculated from 6 samples giving a total sample time of 36 mins. This corresponds to an error of less than 0.5 % for turbulence intensities, less than 8 % for integral length scales, and less than 0.1 % for mean velocities.

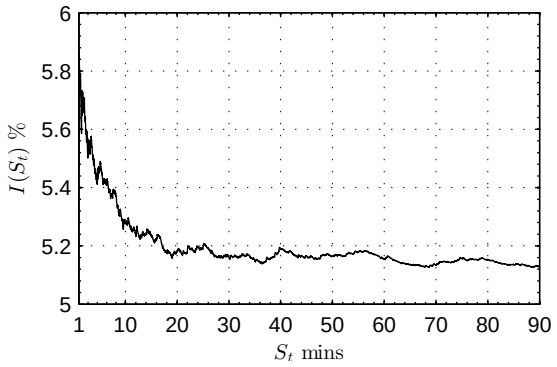

Figure 7.3: Convergence of turbulence intensity with increasing sample length.

7.2.4 Load rig

The discs were mounted on the end of a cantilevered beam with two load cells to measure the thrust force, as shown in figure 7.1, to determine both the thrust and location. The signals from the load cells were passed through a bridge conditioner with amplifier and recorded using analogue to digital data acquisition card at 200 Hz. The load cells were calibrated and thrust coefficients accurate to within 2 % error. The thrust force acting on the disc mounting beam was found to be less than the error (< 2 % of the disc drag), therefore no compensation was applied for the thrust acting on the mounting beam. Figure B.2 in appendix B shows further details of the load rig and key dimensions. The thrust measurements were made with discs located $5.7 < x/M < 20.0$ downstream of the grid. The centre of force for all measurements was within $0.03D$ of the disc centre.

7.3 Flume velocity and turbulence characteristics

The velocity profile of the empty flume was measured and compared against the profiles behind the three turbulent grids. Figure 7.4 shows typical vertical velocity profiles behind the $M = 200$ mm grid compared to the profile of the flume with no grid installed. Figure 7.5 shows the transverse profiles.

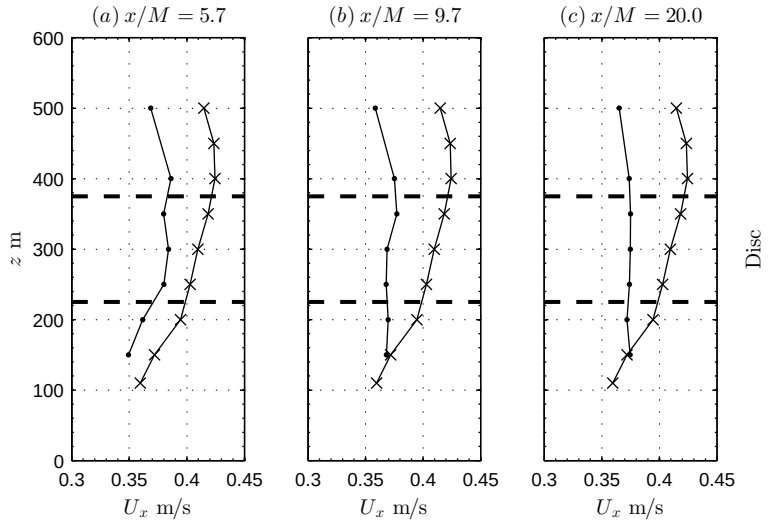

Figure 7.4: Vertical velocity profiles behind Grid-B $M = 200$. —•— = grid data; —×— = empty flume data.

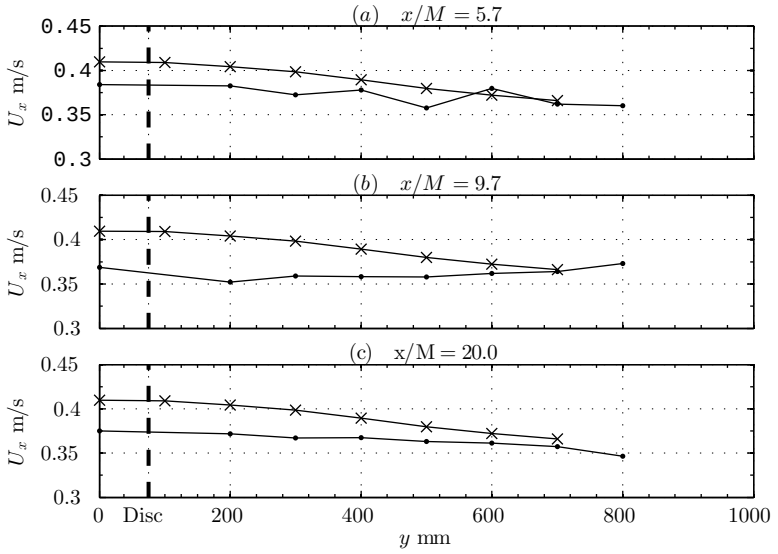

Figure 7.5: Horizontal velocity profiles behind Grid-B, $M = 200$. —•— = grid data; —×— = empty flume data, and $y = 0$ is the flume centreline.

7.3.1 Turbulence decay behind grids

Downstream of the turbulent grid the turbulence intensity decays from $\approx 20\%$ at $x/M = 5.7$ to around 8% at $x/M = 20$. Equation 2.31 was used, taking the virtual origin, $x_o = 0$ (Mohamed & LaRue 1990) and best fit lines fitted to the data as shown in figure 7.6. The data for $x/M = 5.7$ were excluded from this fit due to their high intensity and the energy spectra, discussed below, indicating that the turbulence was still developing. The rate of decay of turbulence intensity behind the three grids is similar with an average decay exponent of $n = 1.33$.

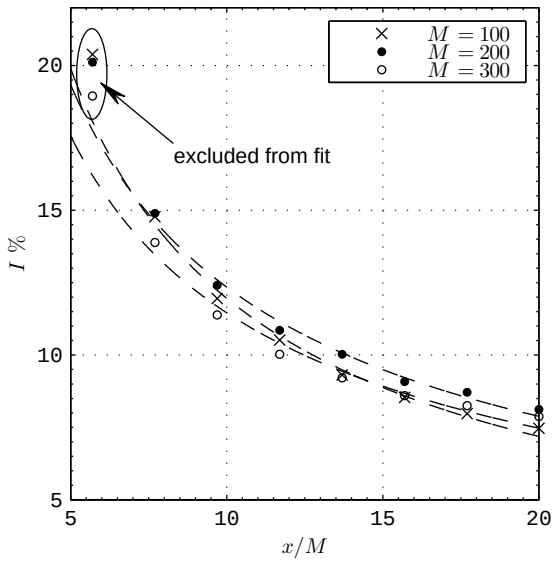

Figure 7.6: Decay of turbulence intensity behind the three turbulent grids.

Similarly it can be seen that the turbulent energy is reducing downstream of the grid as seen in the energy spectra in figure 7.7. A broad -5/3 region defining the inertial subrange was not expected due to the relatively low Taylor scale Reynolds number of $Re_\lambda \approx 100 - 150$, which was higher than measured in the wind tunnel experiments of Krogstad & Davidson (2009) with $Re_\lambda \approx 70 - 90$ and Mohamed & LaRue (1990) with $Re_\lambda \approx 30 - 40$. An inertial subrange is visible as the -5/3 region from $\approx 20 - 30$ Hz, however noise is visible at frequencies approaching the sampling frequency of 50 Hz. This noise is due to aliasing arising from resolving Fourier transforms above the Nyquist frequency of 25 Hz Close to the grid at $x/M = 5.7$ the $-5/3$ region is less clear, indicating that the turbulence is still developing. A measure of isotropy over the disc region was taken as the ratio $\sqrt{u^2} : \sqrt{v^2} : \sqrt{w^2}$ which was found to be typically 1:1.0:0.6 with deviation less than 0.04 behind the three grids.

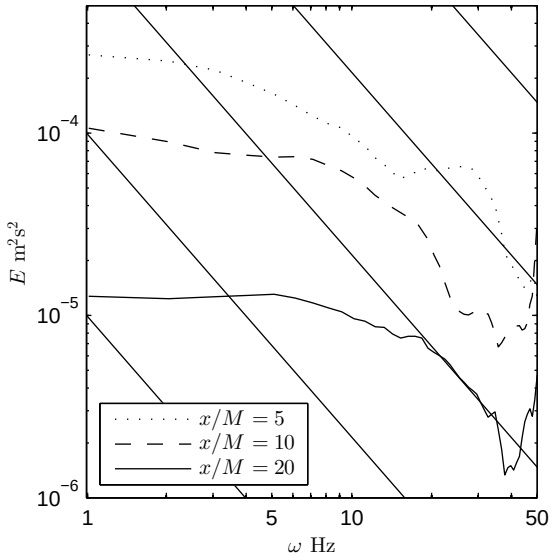

Figure 7.7: Energy spectra behind Grid-B, $M = 200$, with lines of $-5/3$ gradient.

7.3.2 Length scales behind grids

It was found that the length scales increase with distance downstream of the grid as shown in figure 7.8. As expected, the length scales generated by the $M = 300$ mm grid are larger than those generated by the $M = 200$ mm and $M = 100$ mm grids. Length scale growth rate best fit lines of the form of equation 2.32 were applied, as before, data points at $x/M = 5.7$ were excluded from the fit. Figure 7.8 has the following exponents: $n_m(M = 100) = 0.11$; $n_m(M = 200) = 0.35$; $n_m(M = 300) = 0.44$ for each grid.

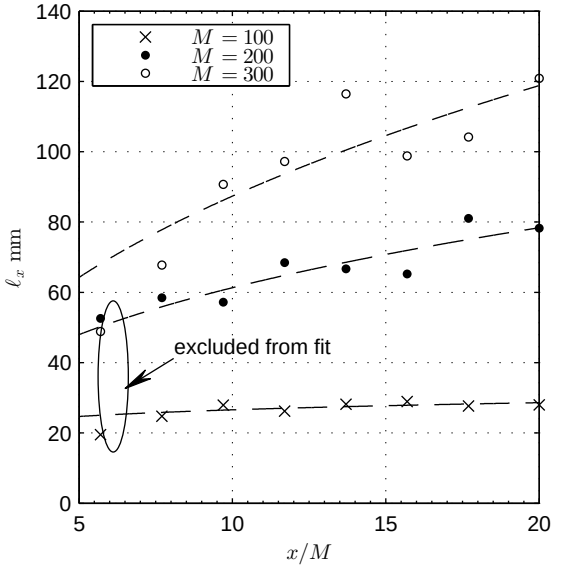

Figure 7.8: Growth of integral length scales downstream of turbulent grids.

7.3.3 Summary

The velocity profiles downstream of the turbulent grids was approximately uniform across the disc as seen in figure 7.4 and figure 7.5. The turbulence fluctuations were approximately isotropic (u:v:w = 1:1:0.6), although lower in the vertical direction, and compared with previous studies where the ratio $\sqrt{v^2}/\sqrt{u^2}$ was found to vary between 0.74-0.9 in a wind tunnel (Comte-bellott & Corrsin 1966). The turbulence decay rate, $n = 1.33$, behind the grids compares well with previous studies of $1.19 < n < 1.47$, when assuming the virtual origin to be zero, Mohamed & LaRue (1990). The integral length scales, figure 7.8, increased with exponent $0.11 < n_m < 0.44$, which compares to $n_m = 0.36$ of Krogstad & Davidson (2009) for similar set-up in a wind tunnel. The difference in length scale growth rate or isotropy is unclear and further investigation would be required to identify differences between grid generated turbulence in flumes and wind tunnels. However, for this investigation the specifics of the decay rates and length scale development are not of paramount importance.

7.4 Results and Discussion

7.4.1 Thrust coefficients with low turbulence

The thrust coefficients measured in the flume with no grid installed are presented in table 7.3. This is a low turbulence case ($I < 4.5\%, \ell_x/D \approx 2$), as expected for this type of flume. The thrust coefficient for the solid discs are compared to typical values in the literature. For the porous disc the drag coefficient is compared with the theoretical relationship of Taylor (1963):

$$C_T = \frac{k_R}{(1 + \frac{1}{4}k_R)^2}. \tag{7.1}$$

where k_R is related by a first order approximation to porosity by $\theta^2 = 1/(1 + k_R)$.

Table 7.3: C_T measurements in the flume with no grid, with $U_\infty \approx 0.4$ and $I < 4.5\%$, compared with predicted values from literature for solid discs and eq. 7.1 for the porous discs.

Disc ID	Re 10^4	ℓ_x/D	Porosity θ	Exp. C_T	Pred. C_T
1	5.2	1.9	0.0 (chamfered)	1.17	≈ 1.17
2	5.2	1.9	0.0 (square)	1.19	≈ 1.17
3	5.2	1.9	0.4	0.91	0.98
4	5.2	1.9	0.6	0.73	0.85
5	3.8	2.7	0.0 (square)	1.17	≈ 1.17
6	3.8	2.7	0.4	0.86	0.98
7	3.8	2.7	0.6	0.60	0.85

Figure 7.9 shows the variation in thrust coefficient with Reynolds number of disc 4 ($D = 150$ mm, $\theta = 0.6$). It can be seen that there is little variation in thrust coefficient for $1 \times 10^4 < Re < 6 \times 10^4$ with an average of $C_T = 0.73$.

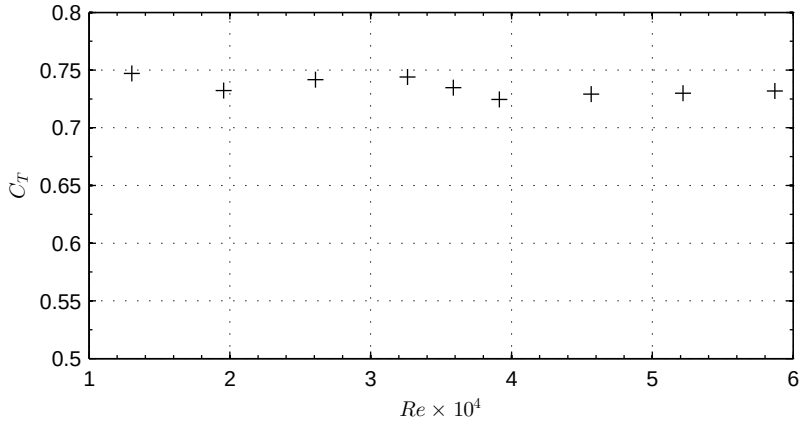

Figure 7.9: Effect of Reynolds number on the thrust coefficient of disc 4 (150 mm diameter, 0.6 porosity).

The thrust coefficients of the solid discs ($1.17 < C_T < 1.19$) in the flume with no grid and low turbulence ($I < 4.5$ %, $\ell_x/D \approx 2$) compare well to previous values of $C_T \approx 1.17$, Knight (1926), Roos & Willmarth (1971). This also shows that the effect of blockage ratio (B_R), defined as the ratio of disc area to flume cross sectional area, is negligible for $B_R = 1.47$ % and $B_R = 0.76$ % for the 150 mm and 108 mm diameter discs respectively. However, the thrust coefficients of the porous discs were lower than predicted from theory, see table 7.3. Figure 7.9 shows that the thrust coefficients of the 0.6 porosity disc are independent of Reynolds number, while the thrust coefficients of the 0.4 porosity discs ($C_T = 0.86 - 0.91$) compare well to previous work by Myers & Bahaj (2010) who found $C_T = 0.86$ for a porosity of ≈0.4. As the hole patterns were the same for the 108 mm and 150 mm porous discs, the difference in thrust is therefore thought to be due to differences in porous hole diameter to disc diameter ratios, which would explain why the difference in thrust is greater for more porous discs, as they have a greater number of holes.

7.4.2 Effect of small scale turbulence on thrust, $\ell_x/D < 0.3$

Small scale turbulence of ≈ 26 mm was generated behind the $M = 100$ mm grid corresponding to $\ell_x/D \approx 0.18$ for the 150 mm discs and $\ell_x/D \approx 0.24$ for the 108 mm discs. It can be seen in figure 7.10 that the effect of increasing turbulence intensity increases the drag coefficient up to $I = 13$ %. As turbulence intensity increases further there is no further change in thrust coefficient. The thrust coefficient decreases with increasing porosity with $1.1 < C_T < 1.3$ for the solid discs, $0.8 < C_T < 1.0$ for the 0.4 porosity discs, and $0.5 < C_T < 0.8$ for the 0.6 porosity discs.

The thrust coefficient of the 150 mm discs was larger than that of the 108 mm discs. As the disc porosity increases it can be seen that the difference between the drag of the 150 mm and 108 mm discs increases.

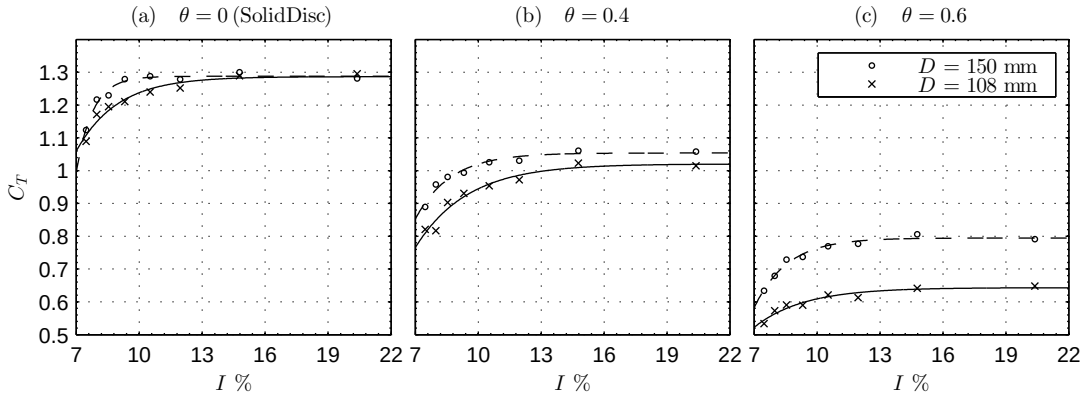

Figure 7.10: Thrust coefficients for small scale turbulence ($\ell_x/D < 0.3$). —x— for $D = 108\ mm$ discs; - -o - - for $D = 150\ mm$ discs.

For these scales and 7 % $< I <$ 9 % the thrust coefficient is lower than measured with low turbulence with no grids ($I < 4.5$ %, $\ell_x/D \approx 2$). This suggests that length scale has a significant effect on thrust coefficient. As the turbulence intensity increases above 10 % the thrust coefficients were higher than measured for the low turbulence case. The thrust coefficients stabilise for turbulence intensities greater than 13 %. Turbulence intensity acts to increase the thrust coefficient as previously found by Schubauer & Dryden (1935), Craze (1977), Bearman & Morel (1983). However, it was also found that there is a limit of $I \approx 13$ %, beyond which the thrust coefficient does not increase further.

7.4.3 Effect of body scale turbulence on thrust, $\ell_x/D \to 1+$

The drag coefficients of the six discs obtained with 10 ± 1 % turbulence intensity are shown in figure 7.11. As before it can be seen that the 108 mm discs have lower drag coefficients than the 150 mm discs.

For both the 108 mm and 150 mm diameter porous discs it can be seen that the drag coefficient decreases with increasing length scale up to $\ell_x/D \approx 0.7$. In both cases there is approximately a 20 % reduction in drag. As ℓ_x/D increases above 0.7 the drag coefficients start to increase. Similar trends are seen for the solid discs, although there is more scatter.

Interpolating between all data points, contour plots were generated to show the combined effects of intensity and length scale on the drag coefficient of the 108 mm discs as shown in figure 7.12. Similar trends were found for the 150 mm discs, but their range of ℓ_x/D was smaller. While fig. 7.11 shows a cross-section of data for which $I \approx 10$ %, fig. 7.12 shows

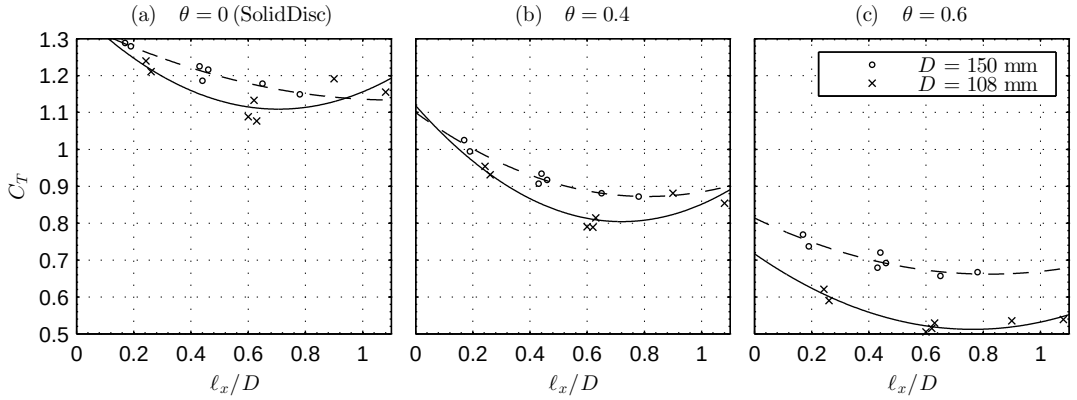

Figure 7.11: Thrust coefficients at 10 ± 1 % turbulence intensity. —x— for $D = 108$ mm discs; - -o - - for $D = 150$ mm discs.

the combined effects of turbulence intensity and integral length scale as a fitted surface to all data. There are some differences between fig. 7.11 and fig. 7.12 as the surface does not intersect each data point, although the fit was very good with a coefficient of determination of approximately 0.9. The minimum thrust occurs at $\ell_x/D \approx 0.7$ as seen in fig. 7.11 but fig. 7.12 shows a minimum at $\ell_x/D \approx 0.5 - 0.6$. It can also be seen, particularly for the 0.6 porosity disc in fig. 7.12(c), that the minimum thrust coefficient occurs at a larger ℓ_x/D ratio with increasing turbulence intensity.

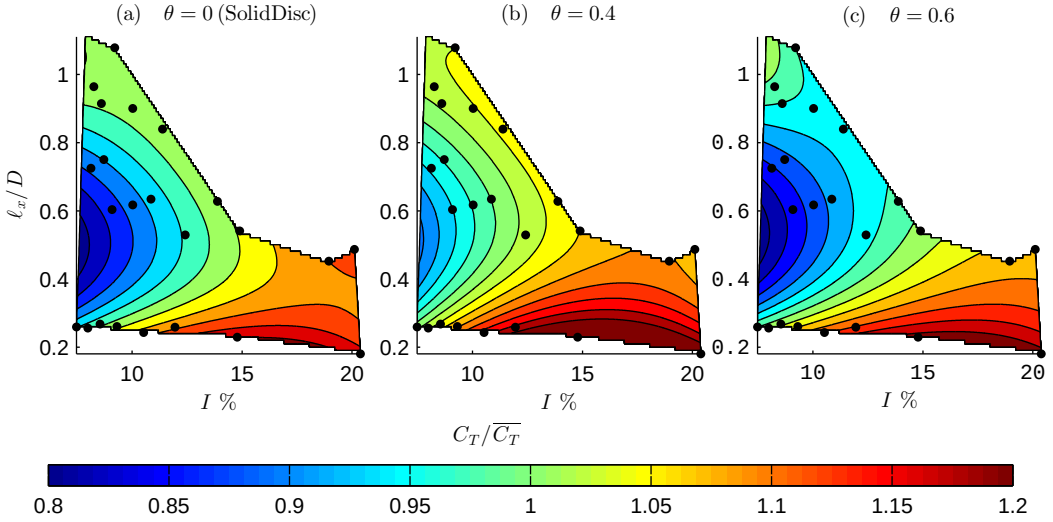

Figure 7.12: Thrust coefficients of 108 mm diameter discs.

It can be seen that thrust coefficient increases with increasing turbulence intensity, which compares to the previous studies by Schubauer & Dryden (1935), Craze (1977), Bearman & Morel (1983). However, the effect of length scale is more complicated than suggested by Craze (1977). For $\ell_x/D \approx 0.7$ minimum thrust coefficients were recorded with overall variation in thrust coefficient in excess of 20 %. It was also found that the thrust coefficients for $I < 4.5$ %, $\ell_x/D \approx 2$ were greater than the case with 7 % $< I < 9$ %

and $\ell_x/D < 0.3$. This suggests that the thrust coefficient would continue to increase for $1 < \ell_x/D < 2$.

7.4.4 Velocity profiles at $3D$ downstream

Due to time constraints limited wake measurements have been made. Vertical velocity profiles were measured at $3D$ downstream of the 150 mm, 0.4 porosity disc in turbulent flows of $I \approx 10$ % and $\ell_x/D = 0.2, 0.6$. It can be seen in figure 7.13 that the velocity deficit is greater for the case with $\ell_x/D = 0.2$ compared to $\ell_x/D = 0.6$, which is consistent with the thrust coefficients recorded of 0.97 and 0.90 respectively. Note, the data is plotted as a continuous profile due to the fine resolution of measurements (≈ 1 mm) made with a profiling ADV. By considering the velocity fluctuations it can be seen in figure 7.14 that $u'u'$ and $v'v'$ are of similar magnitude and greater for the case with larger length scales. This suggests that the rate of mixing is greater with larger length scales and due to the increased generation of turbulence explains the lower velocity deficit for larger length scales. Figure 7.14(c) shows the profile of $w'w'$ which is less than half $u'u'$ and $v'v'$ which is consistent with the anisotropy found in the flow behind the grids.

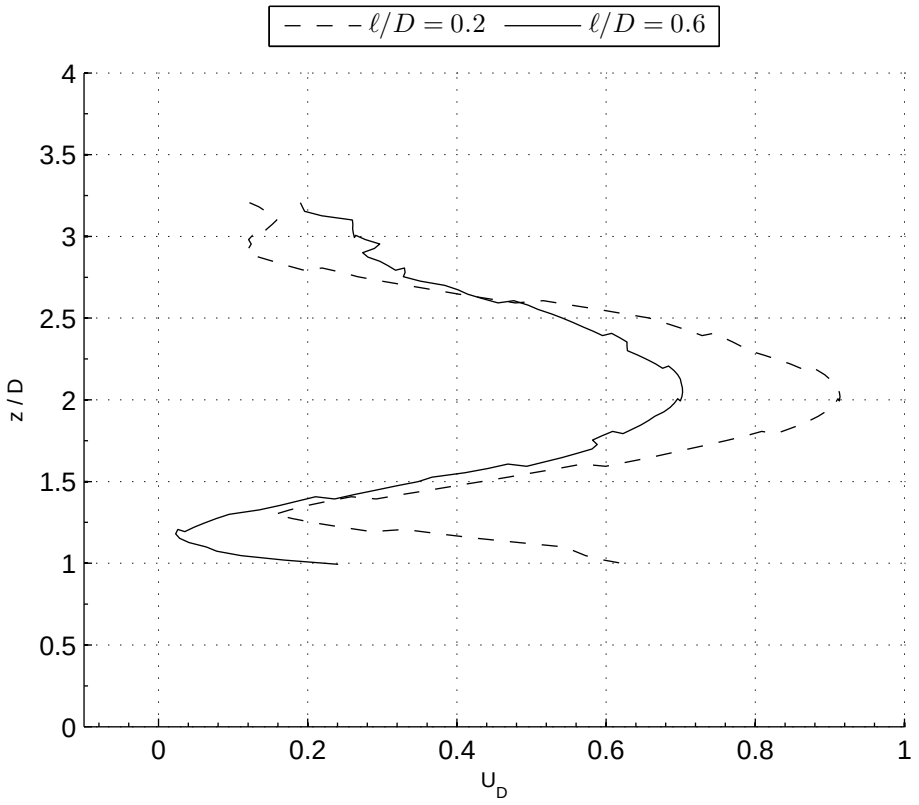

Figure 7.13: Profiles of velocity deficit at $3D$ downstream of the 0.4 porosity, 150 mm diameter disc for $\ell_x/D = 0.2, 0.6$ and $I \approx 10$ %.

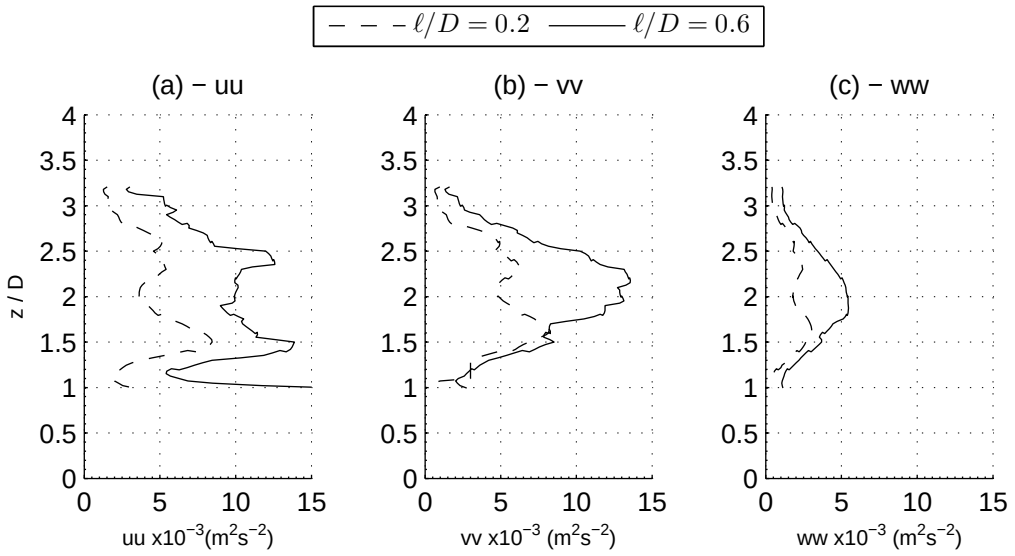

Figure 7.14: Profiles of velocity deficit at $3D$ downstream of the 0.4 porosity, 150 mm diameter disc for $\ell_x/D = 0.2, 0.6$ and $I \approx 10$ %.

7.5 Summary and implications

It has been shown that the thrust forces acting on solid and porous discs are dependent on the turbulent characteristics of the flow. The findings of this chapter are summarised below:

- The thrust coefficients of solid and porous discs are dependent on turbulence intensity and length scale. Similar trends were observed for both solid and porous discs.
- Overall, variations in thrust coefficient of 20 % were observed for different turbulent flow conditions.
- Increasing turbulence intensity increases thrust, for intensities up to 13 %. The thrust coefficient tended to a constant value for intensities greater than 13 %.
- Minimum thrust coefficients were found for length scale to disc diameter ratios of approximately 0.5. Increasing the length scale ratio above 0.5 or reducing the length scale ratio below 0.5 caused the thrust to increase. The minimum thrust occurred at larger length scale to disc diameter ratios as turbulence intensity was increased.
- Further work is required to explain why the smaller diameter porous discs resulted in lower thrust coefficients than the larger diameter discs.
- Further work is required to explain the differences between grid generated turbulence in flumes and wind tunnels.

These findings highlight the need to consider both the size of the turbulent eddies and the intensity of their fluctuations. Predictions of turbine performance made from small scale experiments with low levels of turbulence could under estimate the thrust and power by up to 20 % when operating in high levels of turbulence. This could have a significant impact on the successful design and implementation of a tidal turbine or the success of proposed arrays of multiple devices.

In order to further the understanding of the interaction of turbulence with a turbine it is necessary to consider the effects of turbulent structure on the full wake profile downstream of a tidal turbine. Chapters 8 and 10 present new techniques that have been developed to perform this investigation. The final results, chapter 10, uses these new techniques to investigate the effects of integral length scale and intensity on the wake profiles behind an actuator disc.

Chapter 8

Inlet Grid Generated Turbulence for Large-Eddy Simulations

8.1 Introduction

The previous chapter demonstrated the effects of integral length scale and turbulence intensity on the thrust of a porous disc rotor simulator. It is desirable to use Large Eddy Simulations (LES) to investigate the effects of turbulence on the wake profile of a turbine as detailed information over the whole domain can be obtained, that would be very costly to achieve experimentally. This information is required to explain how, and why, turbulence interacts with an actuator disc turbine representation and its wake.

Section 3.4 discussed the problems associated with generating inlet turbulence with specific characteristics in LES models. This chapter presents a new method of generating inlet turbulence in LES where a solid grid pattern is projected on the inlet boundary as a solid patch. The uniform inlet flow then enters between the solid grid bars and turbulence will develop naturally, as grid generated turbulence in the solution domain. The integral length scale may be controlled by adjusting the grid size, and the turbulence intensity may be controlled by adjusting the distance from the inlet, see section 2.4.

The objective of this chapter is to investigate the mesh and domain requirements of this new technique of generating turbulence in LES by projecting a grid pattern on the inlet boundary. The mesh density, periodicity (or domain size), and Reynolds number dependence are investigated and the results compared with wind tunnel data for validation. This chapter has been published in the international journal of computational fluid dynamics (Blackmore, Batten & Bahaj 2013*a*).

8.2 Numerical Method

The open source code OpenFOAM® 2.0.1 was used to solve the incompressible, finite volume discretisation of the filtered Navier-Stokes equations as discussed in section 3.3.3.

Simulations were run using the pisoFoam solver that uses the PISO algorithm for pressure velocity coupling. A central differencing scheme was used for all spatial discretisation and backward differencing for temporal discretisation. Refer to appendix A for details of the differencing scemes. A time step was set to ensure the Courant number remained less than 0.5. Simulations were run on 128 cores of the IRIDIS supercomputer cluster at the University of Southampton. This corresponded to approximately 7.2 hrs wall time per 1 s simulated time.

8.2.1 Domain and boundaries

Figure 8.1 shows the solution domain and boundaries. Meshes were generated using the OpenFOAM® native meshing software blockMesh and snappyHexMesh to generate meshes with uniform hexahedra cells. The boundary conditions are shown in table 8.1. The single, double, and triple inlet grids show the three different periods, or domain sizes used.

Table 8.1: Turbulent grid boundary conditions. [a]the inlet flow is calculated using the grid porosity, θ, and mean flowrate velocity, U_∞, such that $u_{inlet} = U_\infty/\theta$; [b]switches between zero value and zero gradient, allowing vortices to exit the domain.

Boundary	u	p	ν_{SGS}
Inlet Flow	1.92[a] m/s	Zero Gradient	0
Solid Patch	Zero value	Zero Gradient	Zero Gradient
Outlet	inletOutlet[b]	Zero value	Zero Gradient
Cyclic	Cyclic	Cyclic	Cyclic

An inlet grid spacing of M = 40 mm and porosity of 0.56 was chosen so comparison could be made with the experimental work by Krogstad & Davidson (2009, 2011) with a Reynolds number of $Re = U_\infty M/\nu = 36,000$, where U_∞ is the flowrate velocity. Comparisons were also made with (Mohamed & LaRue 1990) who investigated the turbulence decay rate over a range of geometries and experiments. This grid was used with a single, double, and triple period inlet to assess the effect of domain size on the development of length scales. Two further grid inlets were used with spacing's of M =80 mm and M = 120 mm to investigate the effects of Reynolds number. Table 8.2 shows the eight different cases used. Probes were located on the centerline of the domain from $2 < x/M < 20$ downstream of the grid inlet to record time series data sampled at 1000 Hz.

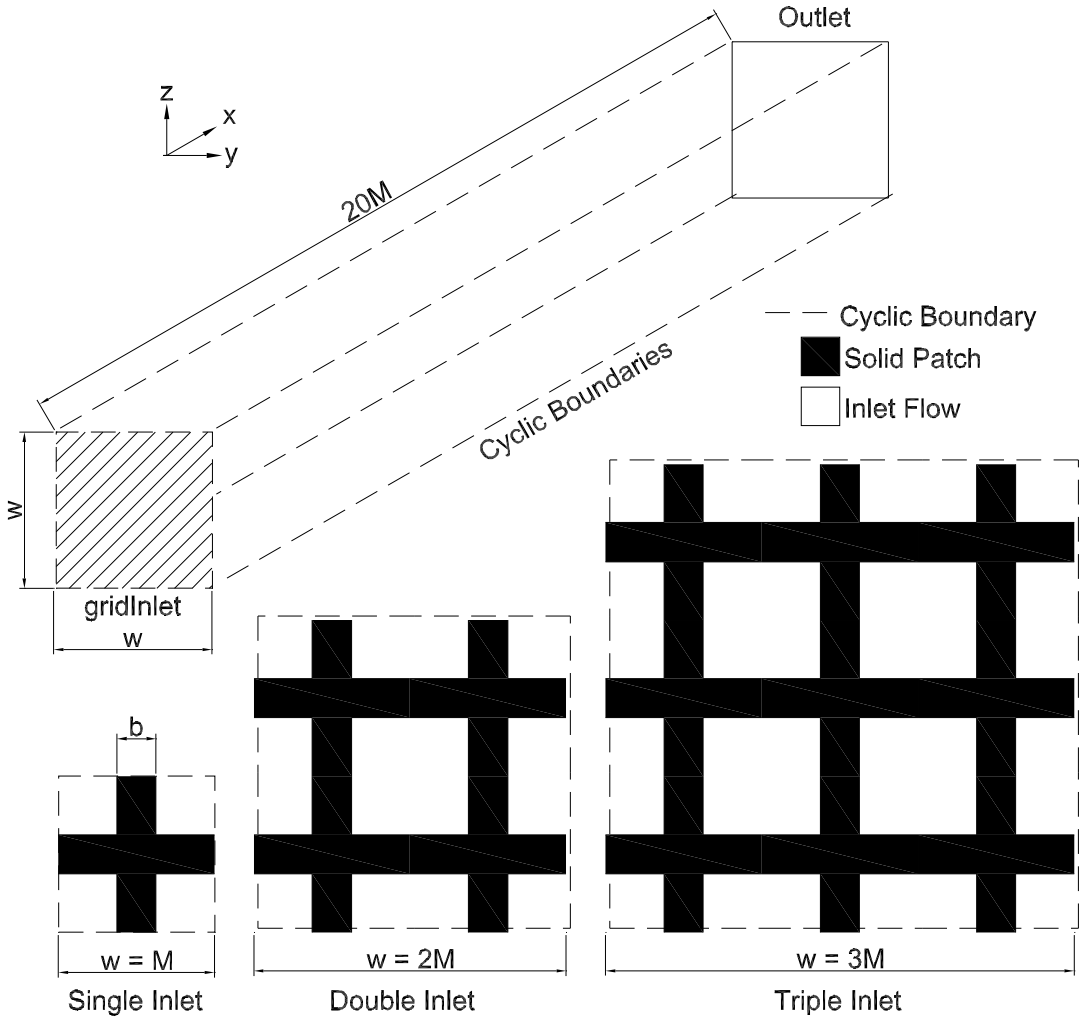

Figure 8.1: Numerical domain and boundaries for single, double, and triple period inlets.

Table 8.2: Mesh and domain details of cases run. [a]Number of cells per grid spacing; [b]Size of domain cross-section, i.e. double period is a domain of $2M$ by $2M$, and triple period $3M$ by $3M$.

Case	Cell density[a]	Grid spacing, M (mm)	Bar width, b (mm)	Inlet Period[b]	$Re = U_\infty M/\nu$
1	$16 \times 16 \times 400$	40	10	Single	36,000
2	$22 \times 22 \times 550$	40	10	Single	36,000
3	$32 \times 32 \times 800$	40	10	Single	36,000
4	$45 \times 45 \times 1125$	40	10	Single	36,000
5	$64 \times 64 \times 800$	40	10	Double	36,000
6	$96 \times 96 \times 800$	40	10	Triple	36,000
7	$96 \times 96 \times 800$	80	20	Triple	72,000
8	$96 \times 96 \times 800$	120	30	Triple	108,000

8.2.2 Data reduction and error estimation

For LES the total turbulence intensity is the summation of the modelled sub-grid scale intensity, I_{SGS}, and the resolved intensity, I_R, such that $I_{tot} = I_R + I_{SGS}$. The SGS turbulent intensity may be calculated by equating the SGS turbulent kinetic energy, k_{SGS}, to the turbulent intensity as shown in equation 8.1.

$$k_{SGS} = \frac{3}{2}(UI_{SGS})^2 = \left(\frac{\nu_{SGS}}{C_K \Delta_g}\right)^2, \tag{8.1}$$

where $C_K = 0.094$ is constant and k_{SGS} is the sub-grid scale component of turbulent kinetic energy. The resolved component of turbulence intensity (I_R) is calculated with the resolved velocity fluctuations using equation 2.16.

Simulations were run for approximately 20 flow though cycles to allow the solution to converge and reach pseudo steady-state. Data was then sampled from this time until the turbulence statistics converged. Figure 8.2 shows how the turbulence intensity and integral length scale of case 6 are affected by the sample time, S_t. It can be seen that a sample time of $S_t = 15$ s is sufficient for the turbulence intensity to converge, but a sample time of $S_t > 20$ s is required for the integral length scale to converge. The error in turbulence intensity is estimated to be < 0.3 % and < 1 % error in integral length scales.

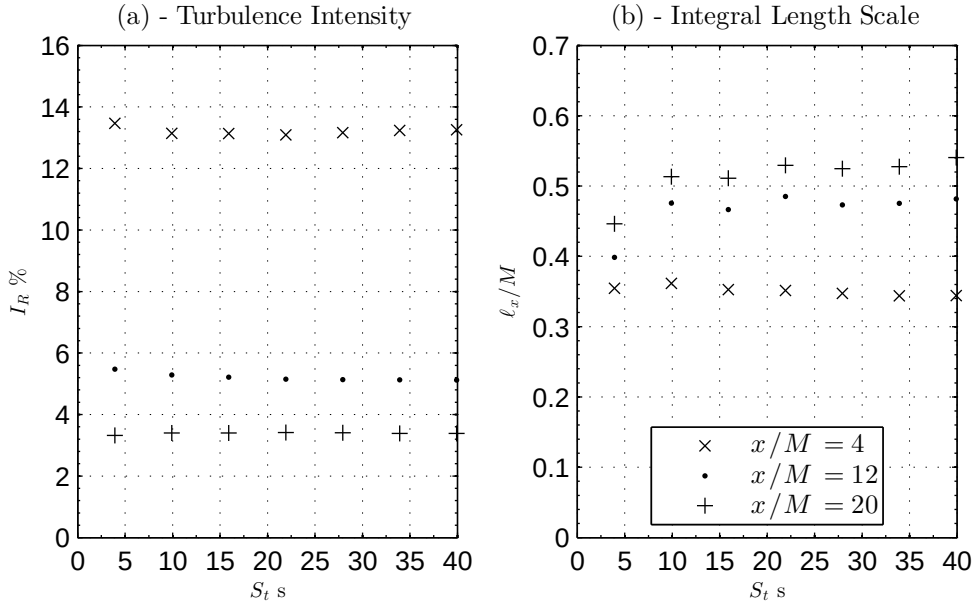

Figure 8.2: Convergence of turbulence intensity and integral length scale with sample time for case 6. Data sampling commenced after $\approx$ 20 flow through cycles to allow the solution to converge and reach pseudo steady-state.

8.3 Results and Discussion

8.3.1 Cell density - (cases 1-4)

Simulations were run on a single grid with four different mesh densities, cases 1-4. It can be seen in figure 8.3(a) that the mesh density used affects the decay of turbulence downstream of the grid inlet. From 16×16 to 22×22 cells per length M there is a large change in the initial dissipation. However for cell numbers of 22×22, 32×32, and 45×45 there is minimal change in the turbulence intensity decay.

Figure 8.3(b) shows the development of integral length scales behind the gridInlet for different mesh densities. It can be seen that there are large differences for the coarser meshes of 16×16 and 22×22 cells. However, there is very little difference between the 32×32 and 45×45 meshes.

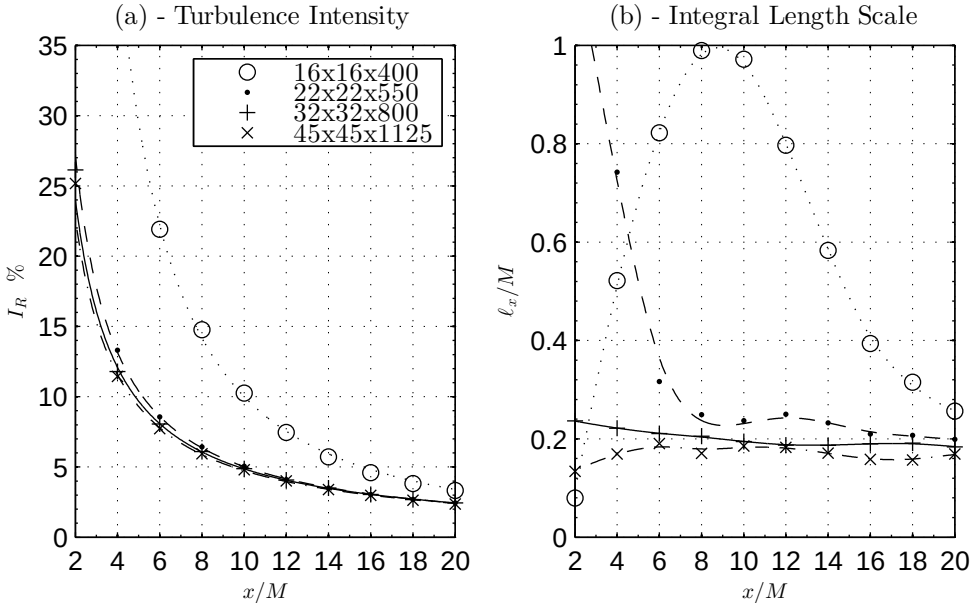

Figure 8.3: Effect of mesh density on turbulence intensity and integral length scale.

Figure 8.4 shows the energy spectra for cases 1-4. It can be seen that the energy contained in the low frequencies is greatest for the 16×16, then 22×22, 45×45, and 32×32. This is consistent with the integral length scales at $x/M = 10$, as seen in figure 8.3, where a larger integral length scale corresponds to higher energy at low frequencies. The inertial sub-range is captured as the -5/3 gradient region for 22×22, 32×32, and 45×45 cells, and only just captured for 16×16 cells. The filter cut-off frequency can be seen as the point where the spectra deviates from the -5/3 gradient as smaller higher frequencies are no longer resolved. Table 8.3 compares the cut-off frequencies estimated from the energy spectra with those predicted using Taylors approximation,

$f = 1/\tau \approx \Delta_g/U$. It can be seen that the predicted and simulated cut-off frequencies compare well. Overall, it was decided that a mesh density of 32×32 cells per length M would be used to perform all further simulations as a good compromise between accuracy and computational efficiency.

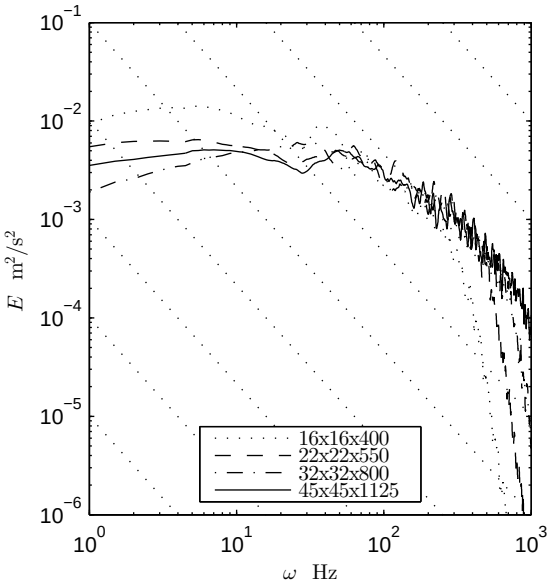

Figure 8.4: Effect of mesh density on energy spectrum at $x/M = 10$.

Table 8.3: LES filter cut-off frequencies.

Case	Cell density	Predicted cut-off frequency (Hz)	Simulated cut-off frequency (Hz)
1	$16 \times 16 \times 400$	216	≈ 200
2	$22 \times 22 \times 550$	297	≈ 300
3	$32 \times 32 \times 800$	432	≈ 450
4	$45 \times 45 \times 1125$	608	≈ 650

8.3.2 Inlet grid period - cases (3,5,6)

Results were compared with single, double and triple grid inlet periods to investigate how the domain size affects the development of length scales. Krogstad & Davidson (2009) found the integral length scale to be $0.6M$ at $x/M = 30$ downstream of their M=40 mm grid.

It can be seen in figure 8.5(a) that there is minimal difference between the decay rate of turbulence intensity for the different inlet periods, with a slightly lower intensity for a single inlet grid period. However, there is significant variation in the development of length scales as seen in figure 8.5(b). The length scale for a single inlet grid is around $0.2M$ which is significantly less than recorded experimentally. This suggests

that the cyclic boundaries are too close and constrict the turbulent eddy development. The double and triple inlet grids produce comparable length scales up to a distance of $x/M = 6$. Beyond which the length scales converge to around $0.4M$ for the double inlet grid, while the triple inlet grid allows the length scales to continue to grow to $\approx 0.54M$ at $x/M = 20$.

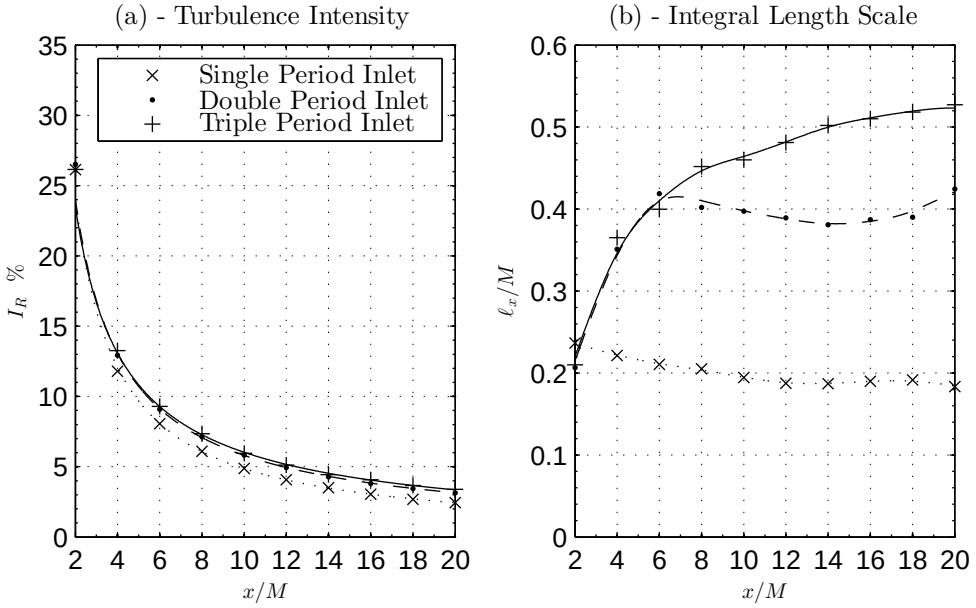

Figure 8.5: Effect of inlet grid period on turbulence intensity and integral length scale.

Figure 8.6 shows the energy spectrum of the three grids. It can be seen that the spectrum of the double and triple grids is comparable, while the single inlet grid contains less energy in the low frequencies. This is to be expected for a smaller integral length scale.

Finally, figure 8.7 shows contours of vorticity magnitude for single, double and triple grid periods. While each of the three grids show similar trends with the inlet jet forming instabilities which break up and form turbulence, the triple inlet grid produces turbulent structures that appear more defined.

A triple inlet grid was therefore selected as the minimum grid period in order to allow turbulence to develop without being constrained by the computational domain.

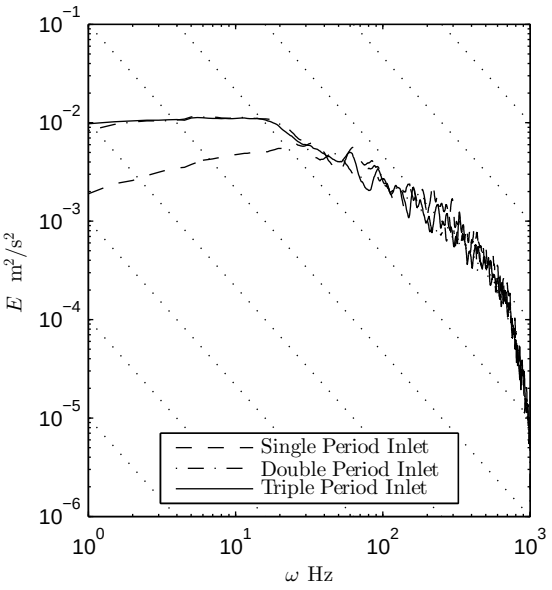

Figure 8.6: Effect of inlet grid period on energy spectrum at $x/M = 10$.

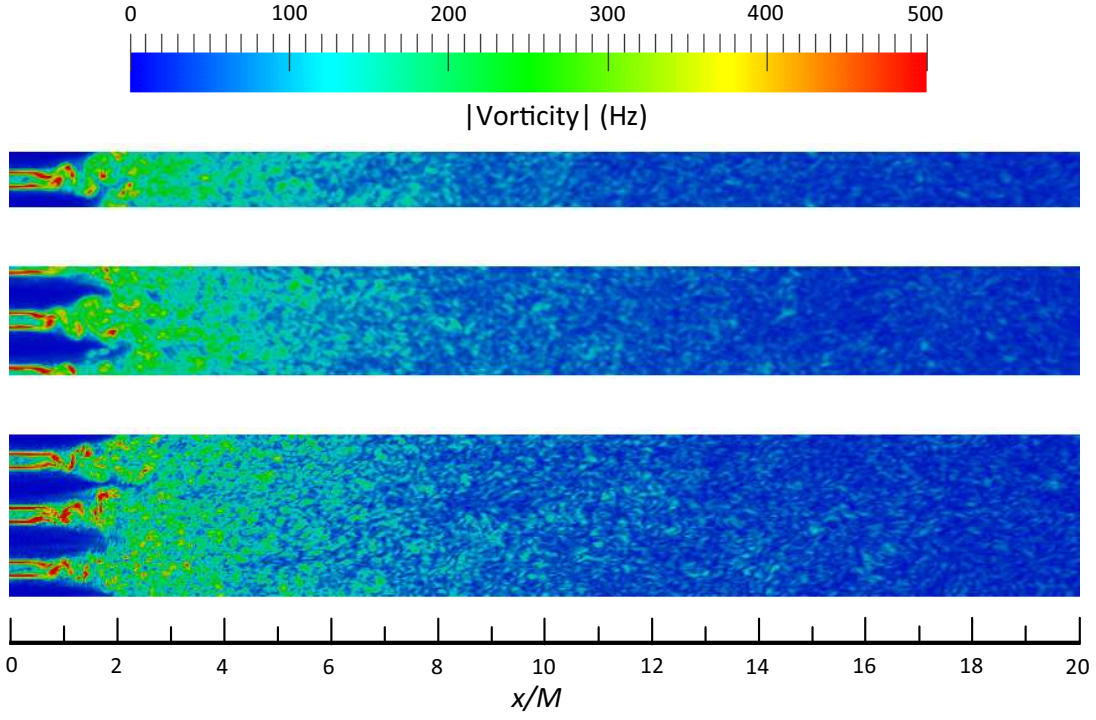

Figure 8.7: Effect of domain size on the development of vorticity for single, double, and triple inlet grids.

8.3.3 Reynolds number - cases, (6,7,8)

The effect of Reynolds number was investigated using triple inlet grids with a cell density of 32 cells per length M, and $M = 40, 80, 120$ mm, corresponding to $Re = 36,000, Re =$

$72,000, Re = 108,000$. Figure 8.8 (a) shows that the decay rate of turbulence intensity is independent of Reynolds number. The velocity fluctuations in the y and z directions were found to be within 0.5%, while the ratio of velocity fluctuations in the x direction to fluctuations in the y direction was found to be typically $\sqrt{u'^2}/\sqrt{v'^2} \approx 1.12$. This compares well to wind tunnel data where grid generated turbulence has been found to be isotropic with a range of $1.05 < \sqrt{u'^2}/\sqrt{v'^2} < 1.35$ (Comte-bellott & Corrsin 1966).

Figure 8.8 (b) shows how the integral length scales grow with distance downstream of the grid. It can be seen that there is a higher growth rate with increasing Reynolds number. Best fit lines of the form of equation 2.32 have been applied to the data, again taking the virtual origin to be zero ($x_o = 0$). The typical length scale growth rate was found to be $n_m = 0.33$ with a range of $0.24 < n_m < 0.44$ as shown in table 8.4. This compares well to Krogstad & Davidson (2009), $n_m = 0.36$ and Krogstad & Davidson (2011), $n_m \approx 0.4$.

The decay exponent of the turbulence intensity, as described in equation 2.31, was found to be $1.66 < n < 1.69$ taking the virtual origin to be zero ($x_o = 0$), which compares to $n \approx 1.33$ found experimentally by Mohamed & LaRue (1990). Figure 8.9 shows the resolved component and modelled sub-grid scale component of turbulence intensity for $Re = 36,000$. The decay rate of the modelled component was found to be $n = 1.89$ resulting in a total decay rate of $n = 1.74$. It can be seen that the power law produces a significantly better agreement for the total turbulence intensity close to the inlet ($x/M < 6$). While the decay rates are higher than measured experimentally, they compare well to previous studies of freely decaying homogeneous isotropic turbulence using LES, $1.17 < n < 2$, as shown in table 8.4.

Figure 8.10 shows the energy spectrum for $Re = 36,000$, $Re = 72,000$, and $Re = 108,000$. It can be seen that increasing the Reynolds number increases the energy at the low frequencies, consistent with an increase in integral length scale. At higher frequencies the inertial sub-range is captured, but the filter cut off frequency is lower for increasing Reynolds number due to the same cell density of 32×32 being used for the three grids, resulting in a smaller cell size and hence filter size for the lower Reynolds numbers. For very large Reynolds numbers, the cell density may need to be increased to ensure the inertial sub range is captured.

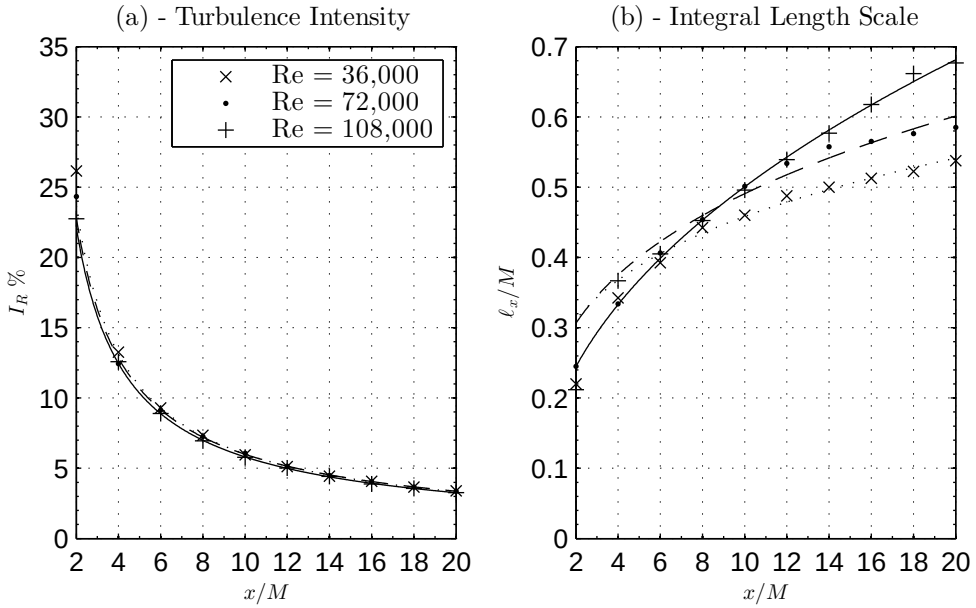

Figure 8.8: Effect of Reynolds number on turbulence intensity and integral length scale. Data points for $x/M < 6$ have been excluded from the fit.

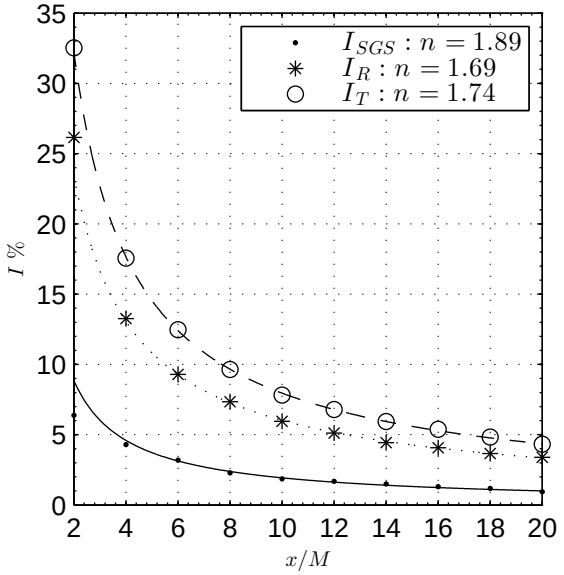

Figure 8.9: Resolved and modelled components of turbulence intensity for the $M = 40$ mm grid, $Re = 36,000$.

Table 8.4: Turbulent decay rates in LES. [a] Re = Flow Reynolds number; Re_λ=Taylor microscale Reynolds number, λ=Taylor microscale; [b] Simulations in the limit of an infinite Reynolds number such that dissipation is from the sub grid model only; [c] at $x/M = 10$.

Turbulence generation	Reynolds Number[a] $Re = \frac{UM}{\nu}$	$Re_\lambda = \frac{u\lambda}{\nu}$	decay rate n	Length scale exponent, m	Author
Random field with prescribed energy spectra	-	71.6	1.17-1.27	-	Carati et al. (1995)
Random field with prescribed energy spectra, or previously developed turbulent field	-	21-195	1.81	-	Wang et al. (1996)
Previous DNS simulation	-	60-90	2	-	Hughes et al. (2001)
Random field satisfying energy spectra	∞[b]		1.97	-	Terracol & Sagaut (2003)
-	200	104	1.3	-	Chumakov & Rutland (2005)
gridInlet	36,000	82[c]	1.69	0.24	present results
gridInlet	72,000	115[c]	1.66	0.29	present results
gridInlet	108,000	142[c]	1.66	0.44	present results

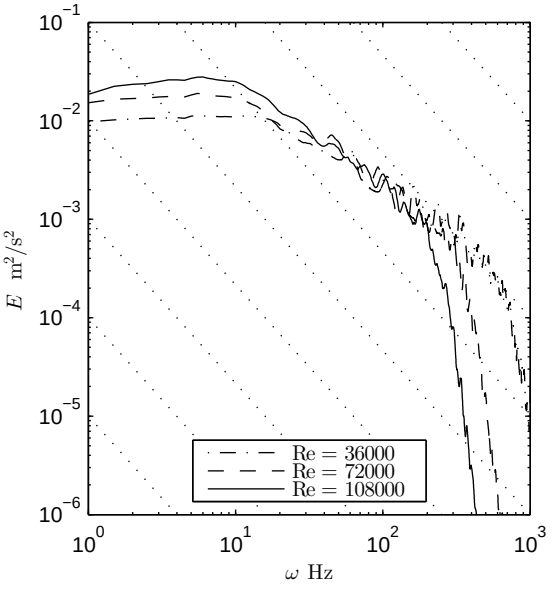

Figure 8.10: Effect of Reynolds number on energy spectrum at $x/M = 10$.

8.4 Comparison with experiments

The previous section has presented results on the mesh and domain requirements for the implementation of the gridInlet technique. This section uses the gridInlet technique to compare with the experimental results behind a grid installed in a water channel from chapter 7.

8.4.1 Numerical domain

The numerical domain is shown in figure 8.11 and based on the flume used for the experimental investigation of chapter 7. Two gridInlets were used with grid spacings of $M = 100$ mm and $M = 300$ mm and the walls, bed and surface were set as free slip due to the uniform velocity profiles recorded behind the grids in the experiments, therefore the effects of the boundary were assumed to be negligible. Finally the the outlet was set to zero gradient. As before, the domain was split into a mesh of hexahedral cells using the OpenFOAM® native meshing software blockMesh and snappyHexMesh (OpenCFD 2012) with approximately 9×10^6 cells.

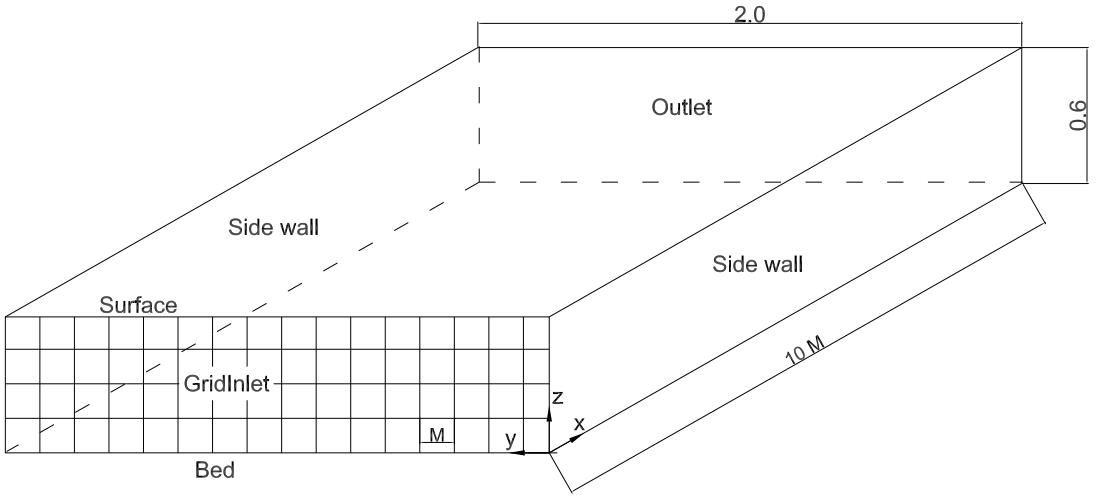

Figure 8.11: Numerical domain used to model the grid generated turbulence in a water channel as used in the experimental investigation, chapter 7.

8.4.2 Comparison of turbulence profiles from the gridInlet and experiments

Comparisons have been made between the profiles of normalised velocity and turbulent fluctuations at 5 and 10 x/M downstream of the grid. It can be seen in figure 8.12(a,b) that the velocity profiles behind the $M = 100$ mm grid are approximately uniform across the depth, which compares well to the experimental data at the centre where the

porous disc was located. Near the surface there is some variation in the experimental data attributed to the effects of the free surface. For the $M = 300$ mm grid it can be seen that a profile exists as seen in figure 8.12(c,d). This profile is due to the large bar spacing compared to the channel depth resulting in a grid bar located across the centreline, further downstream the profile reduces as the flow continues to mix. However, the variation in velocity across the centre where the disc is located is less than 2% and therefore unlikely to affect results with a disc installed. The variation in experimental results is also minimal across the disc, but a visible profile is evident across the depth. Overall the velocity profiles can be assumed uniform across the centre where the discs were located in both experiments and LES model. The differences in profiles close to the surface or bed of the experimental results are attributed to effects of the free-surface and boundary layer driven from the bed.

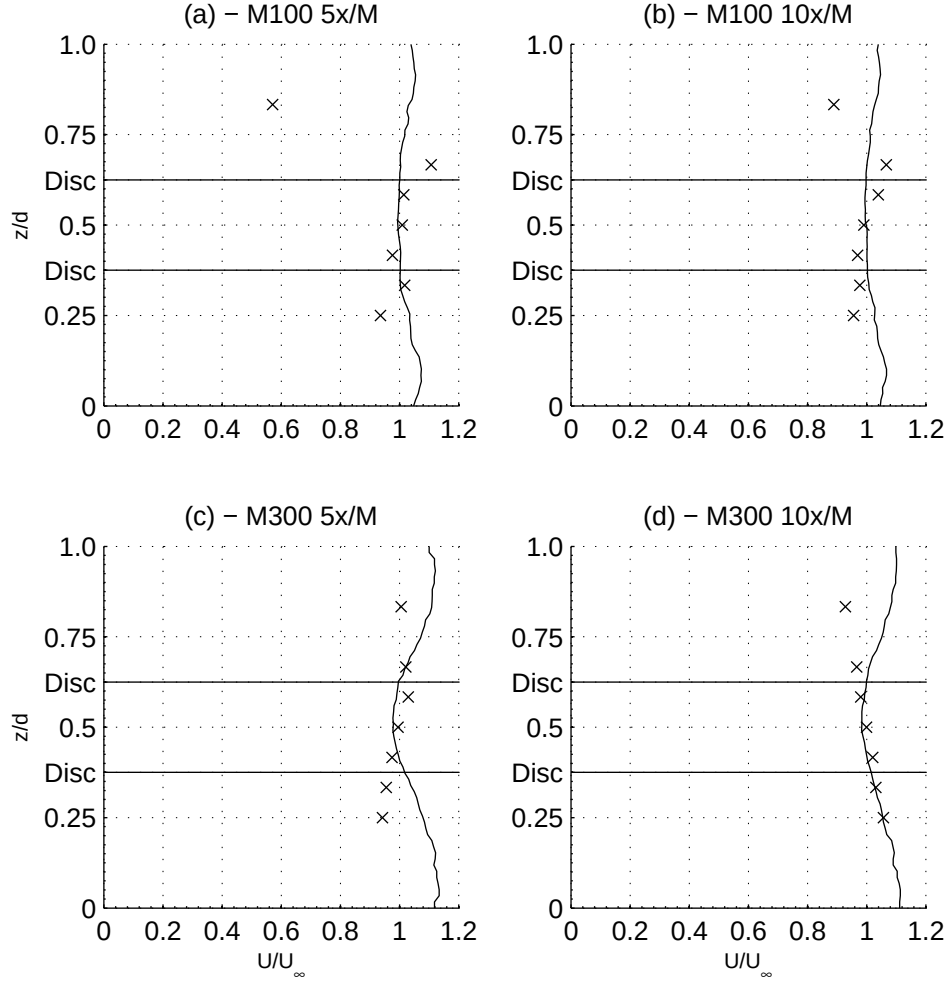

Figure 8.12: Profiles of normalised velocity behind LES gridInlet and experiments for $M = 100$ mm and $M = 300$ mm.

Figure 8.13 shows the profiles of $u'u'$ from the LES gridInlet and experimental results normalised with the free stream velocity squared. It can be seen that the profiles from

the LES model are uniform across the depth. In the experiments $u'u'$ is of comparable magnitude for the $M = 100$ mm and $M = 300$ mm grids from experiments with approximately uniform profiles, although $u'u'$ increases for the $M = 100$ mm grid in the upper half of the flow. However, $u'u'$ is approximately 2-3 times larger for the experiments than the LES model. A possible cause of this could be due to turbulence in the flow upstream of the grids in the experimental case ($I \approx 4.5$ %) which would add to the grid generated turbulence increasing the component $u'u'$ over the LES case where a zero turbulence flow enters the grid.

Similar trends are seen for the transverse component $v'v'$, figure 8.14, but the vertical component $w'w'$ shows smaller fluctuations for the experiments as seen in figure 8.15. Note that $w'w'$ goes to zero at the boundaries due to the walls. The cross components $u'v'$, $u'w'$, and $v'w'$ are shown in appendix C.1 and all fluctuate about zero. Table 8.5 shows the normalised Reynolds stresses averaged over the depth occupied by the disc in the axial, transverse, and vertical directions. For the LES model the ratio $u'u' : v'v' : w'w' \approx 1 : 0.7 : 0.7$ which is comparable to the ratios of $\sqrt{u'u'} : \sqrt{v'v'} : \sqrt{w'w'}$ found earlier in this chapter and compares well to wind tunnel studies of (Comte-bellott & Corrsin 1966). However, in the experiments a ratio of $u'u' : v'v' : w'w' \approx 1 : 1.1 : 0.35$ was measured showing the anisotropy in the vertical direction. Also the standard deviation of normalised Reynolds stress across the center of the flume where a disc would be installed was approximately an order of magnitude larger for the experiments than the LES model as seen in table 8.6. This further demonstrates the turbulence characteristics of the experimental configuration are less stable and more chaotic than simulated in the LES model.

To further investigate the isotropy of the experiments and LES gridInlet the normalised Reynolds stress components $u'u'$, $v'v'$, and $w'w'$ have been cross plotted. Figure 8.16 shows that the magnitude of $u'u'$ and $v'v'$ is greater for the experiments than the LES model, and both LES model and experiments are almost isotropic in the axial and transverse directions as the data is close to the diagonal line representing isotropic flow. However, considering the components $v'v'$ and $w'w'$ as shown in figure 8.17 it can be seen that the LES model is producing isotropic turbulence with $v'v' \approx w'w'$ but in the experiments $w'w'$ is approximately half the magnitude of $v'v'$. It is postulated that the anisotropy of the experiments was due to boundary layer and free surface effects constraining the growth of turbulence in the vertical direction.

Further, differences are seen in the turbulence intensities and integral length scales as shown in table 8.7. It can be seen that the turbulence intensities compare well between the different grid sizes, but the intensities measured in the experiments are approximately double those from the LES model, consistent with the measurements of $u'u'$ previously discussed. The integral length scales were also larger in the LES model than measured experimentally, approximately double for the $M = 300$ mm grid.

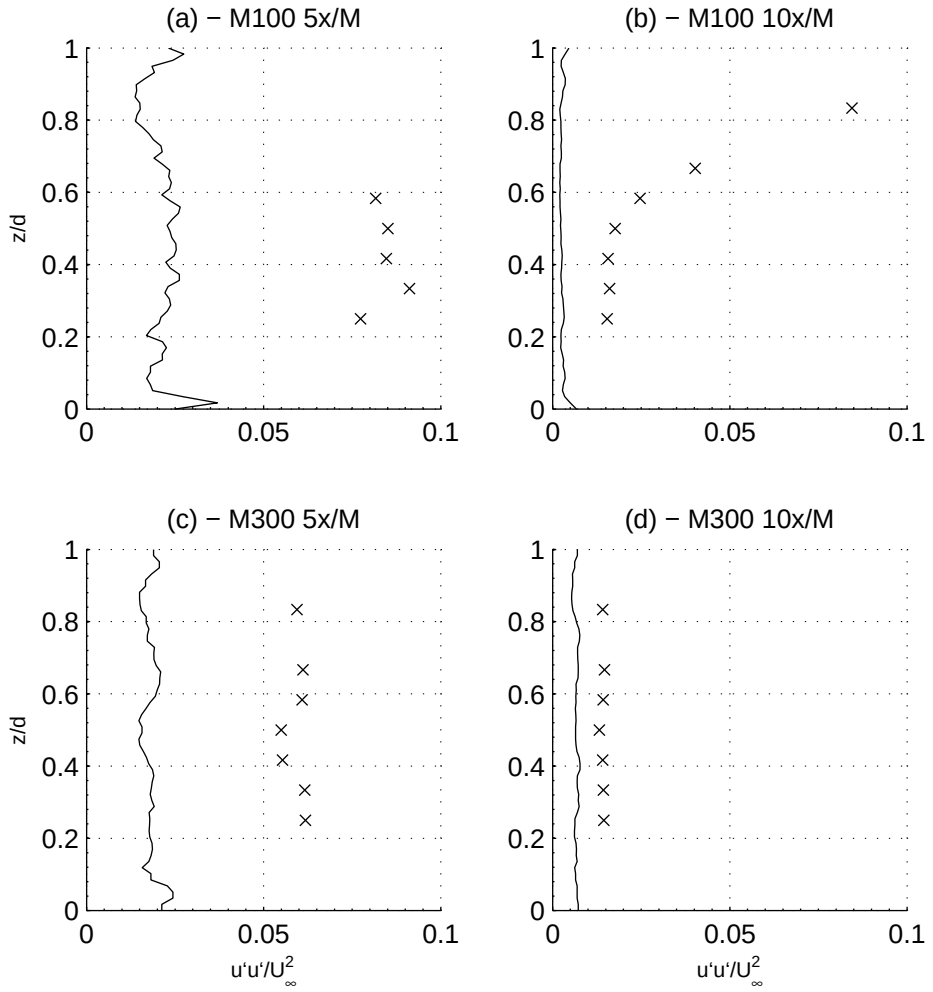

Figure 8.13: Profiles of $u'u'$ behind LES gridInlet and experiments for $M = 100$ mm and $M = 300$ mm.

Table 8.5: Normalised Reynolds stresses in the axial, transverse, and vertical directions averaged over the flume center for $1/3 < z/d < 2/3$ where an actuator disc would be installed.

Grid spacing, M (mm)	location x/M	$\left\langle \frac{u'u'}{U_\infty^2} \right\rangle \times 10^{-2}$ LES	Exp.	$\left\langle \frac{v'v'}{U_\infty^2} \right\rangle \times 10^{-2}$ LES	Exp.	$\left\langle \frac{w'w'}{U_\infty^2} \right\rangle \times 10^{-2}$ LES	Exp.
100	5	2.41	8.91	1.62	10.23	1.69	2.48
100	10	0.23	2.29	0.15	2.23	0.14	0.88
300	5	1.76	5.88	1.32	6.72	1.34	2.62
300	10	0.69	1.41	0.48	1.51	0.46	0.63

Finally, the energy spectrum was compared at 5 x/M as shown in figure 8.18 and at 10 x/M as shown in figure 8.19. It can be seen that the inertial sub-range is captured as the -5/3 gradient for both LES models and experiments, and the experimental energy spectra is capped at the measurement frequency of 50 Hz. For the LES model the energy

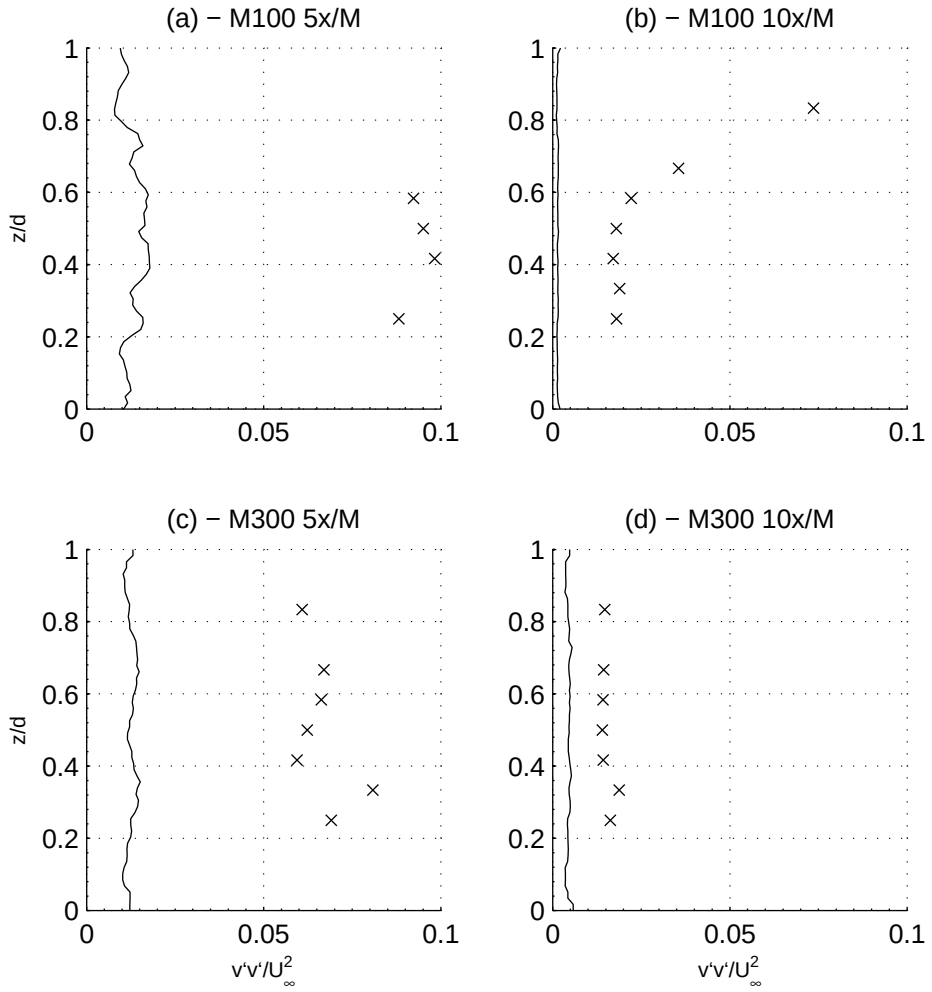

Figure 8.14: Profiles of $v'v'$ behind LES gridInlet and experiments for $M =$ 100 mm and $M = 300$ mm.

Table 8.6: Standard deviation of normalised Reynolds stresses in the axial, transverse, and vertical directions across the flume center for $1/3 < z/d < 2/3$ where an actuator disc would be installed.

Grid spacing, M (mm)	location x/M	Std. $\left\langle \frac{u'u'}{U_\infty^2} \right\rangle \times 10^{-3}$ LES	Exp.	Std. $\left\langle \frac{v'v'}{U_\infty^2} \right\rangle \times 10^{-3}$ LES	Exp.	Std. $\left\langle \frac{w'w'}{U_\infty^2} \right\rangle \times 10^{-3}$ LES	Exp.
100	5	1.40	8.44	1.39	9.97	0.83	2.59
100	10	0.21	10.38	0.08	7.62	0.08	4.49
300	5	2.06	3.34	1.03	8.24	0.86	0.93
300	10	0.41	0.54	0.22	2.06	0.25	0.20

contained in the low frequencies is greater for the M =300 mm grid at both 5 and 10 x/M, which is consistent with larger integral length scale. However, the experimental results show similar energy content for both $M = 100$ mm and $M = 300$ mm grids. Further, It can be seen that the energy contained at low frequencies, less than 10 Hz, is

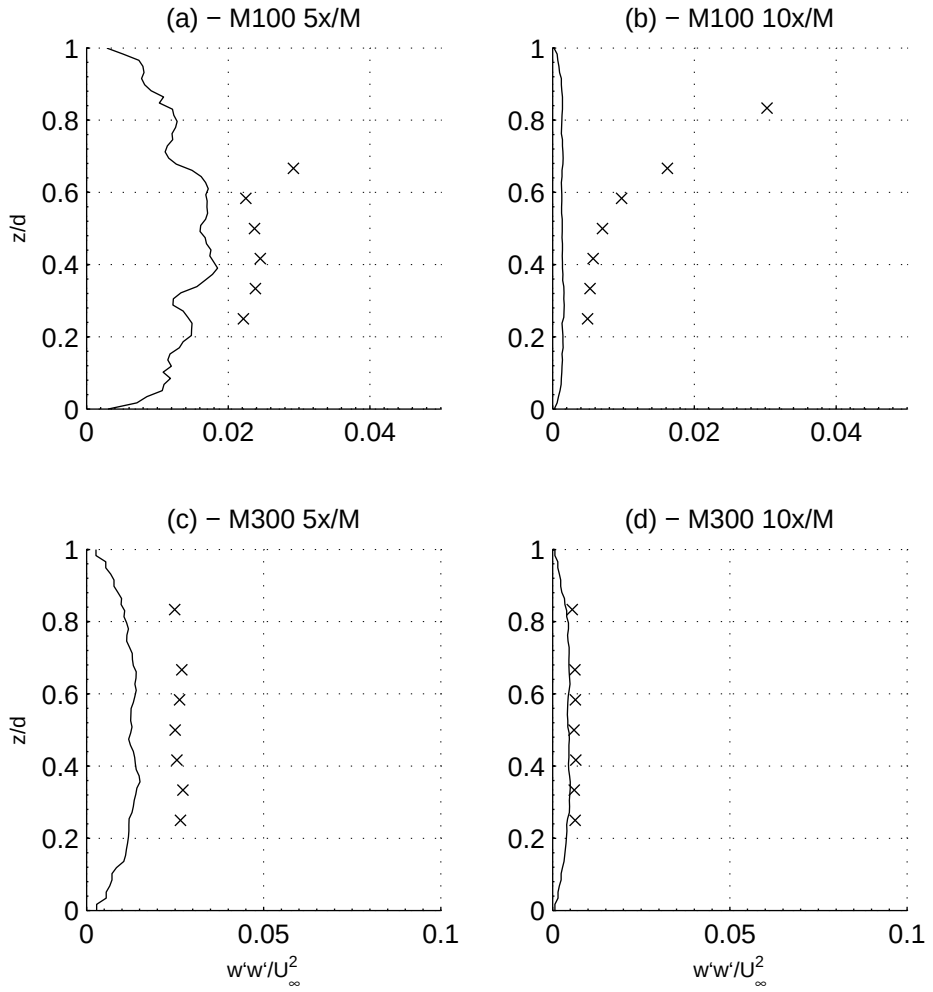

Figure 8.15: Profiles of $w'w'$ behind LES gridInlet and experiments for $M = 100$ mm and $M = 300$ mm.

Table 8.7: Turbulence intensity and integral length scales from experiments and LES gridInlet.

Grid size M (mm)	Distance downstream x/M	Turbulence intensity (%) Exp.	LES	Integral length scale (mm) Exp.	LES
100	5	20.1	11.7	17.5	37.2
100	10	11.9	5.6	28.6	35.3
300	5	18.3	11.3	46.7	81.8
300	10	10.8	6.6	76.0	132

larger in the LES model compared to the experiments. This is consistent with the larger integral length scales simulated in the LES model compared to the experiments. Other factors may also affect the energy levels in the experiments such as greater losses incurred in the experimental set up compared to the LES model, the boundary layer has not been resolved which would dissipate some energy through turbulence close to the boundaries,

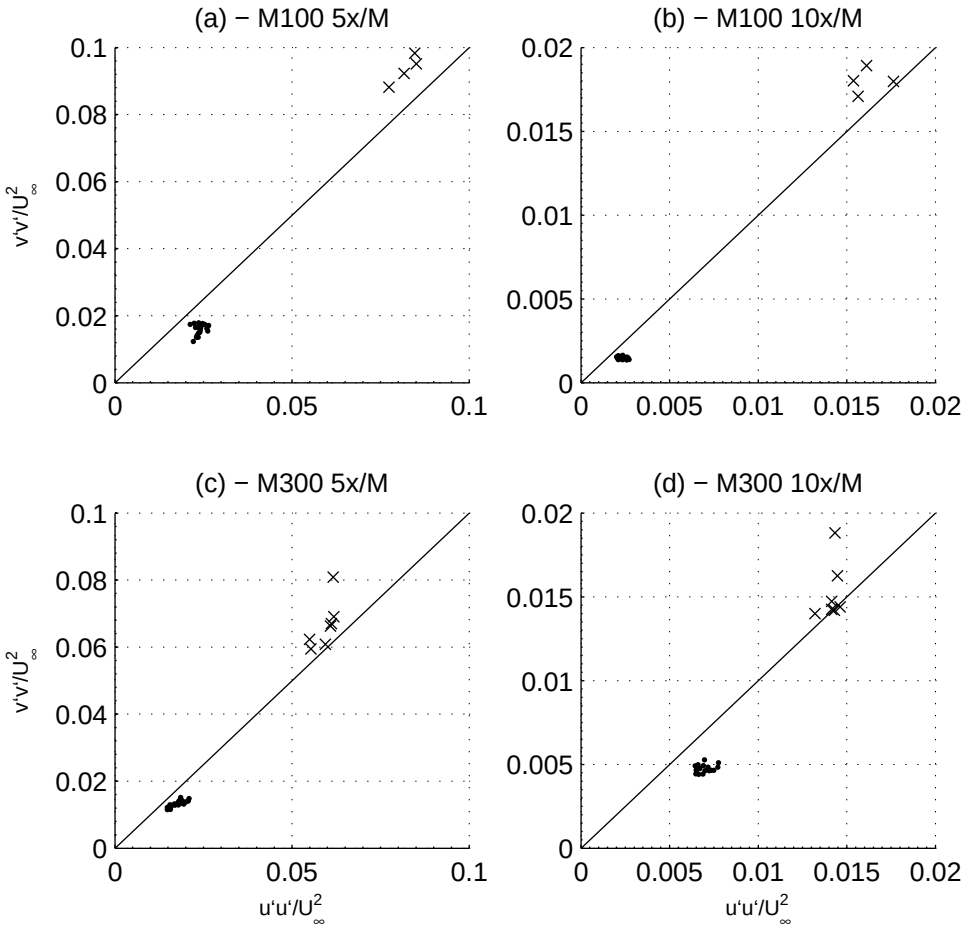

Figure 8.16: Comparison of $u'u'$ and $v'v'$ as a measure of isotropy behind LES gridInlet and experiments for $M = 100$ mm and $M = 300$ mm. $\bullet$ = LES model, $+$ = Experiments

and there is low level turbulence upstream of the grid that may influence the turbulence characteristics downstream in the experiments. However, further investigation would be required into grid generated turbulence in flumes which is beyond the scope of this study.

8.4.3 Summary

Overall the gridInlet method produces approximately isotropic turbulence with a uniform profile across the centre of the flume where an actuator disc would be installed. A larger gridInlet spacing generated larger integral length scales with corresponding higher turbulent energy. However, the turbulence generated did not match the specific characteristics measured experimentally in the flume. This was due to the anisotropy of the experiments which was attributed to free-surface, boundary layer effects, and upstream turbulence entering the grid.

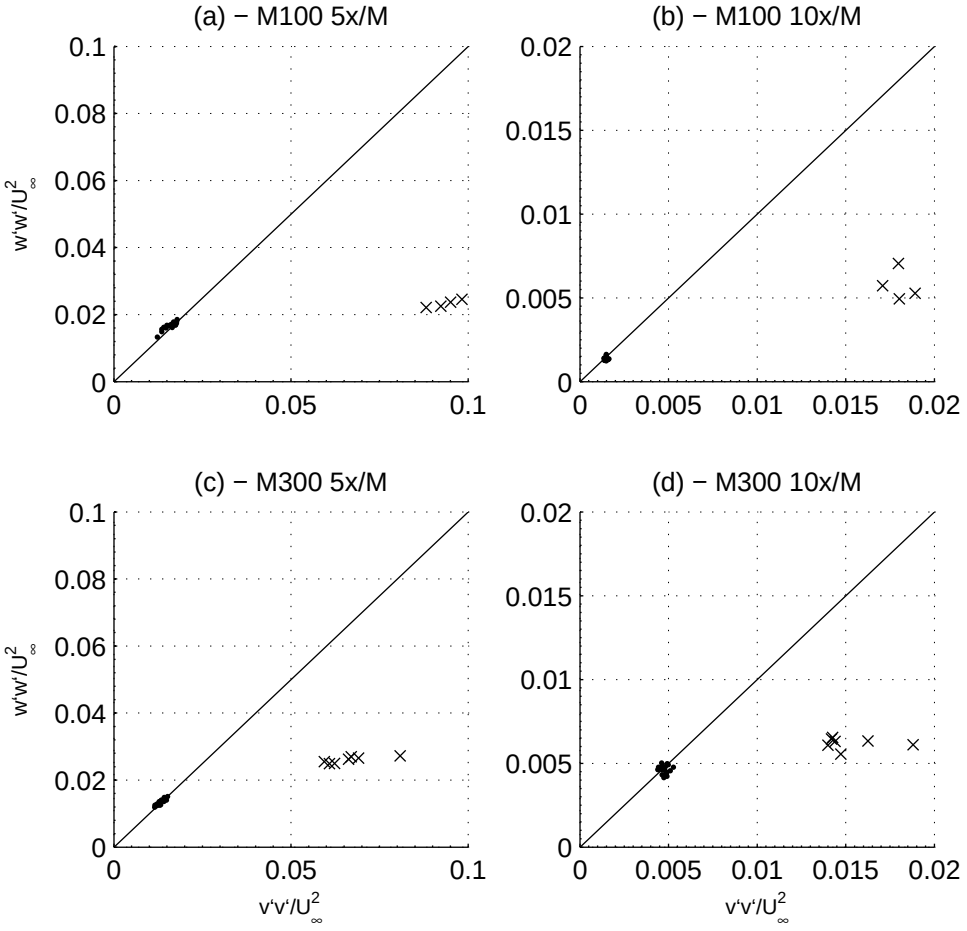

Figure 8.17: Comparison of $v'v'$ and $w'w'$ as a measure of isotropy behind LES gridInlet and experiments for $M = 100$ mm and $M = 300$ mm. $\bullet$ = LES model, $+$ = Experiments

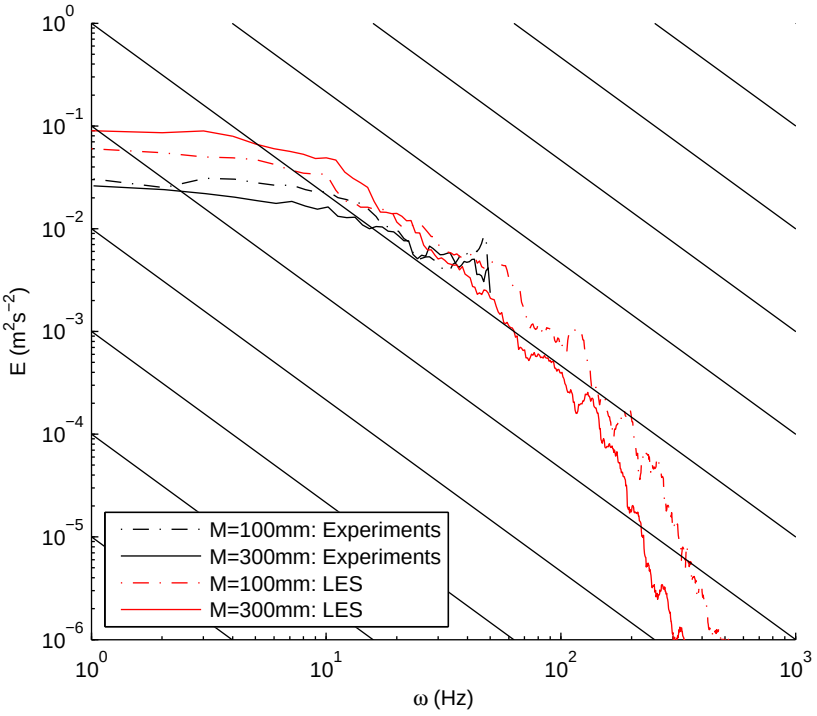

Figure 8.18: Energy spectra at 5 x/M downstream of the gridInlet compared to the experimental conditions.

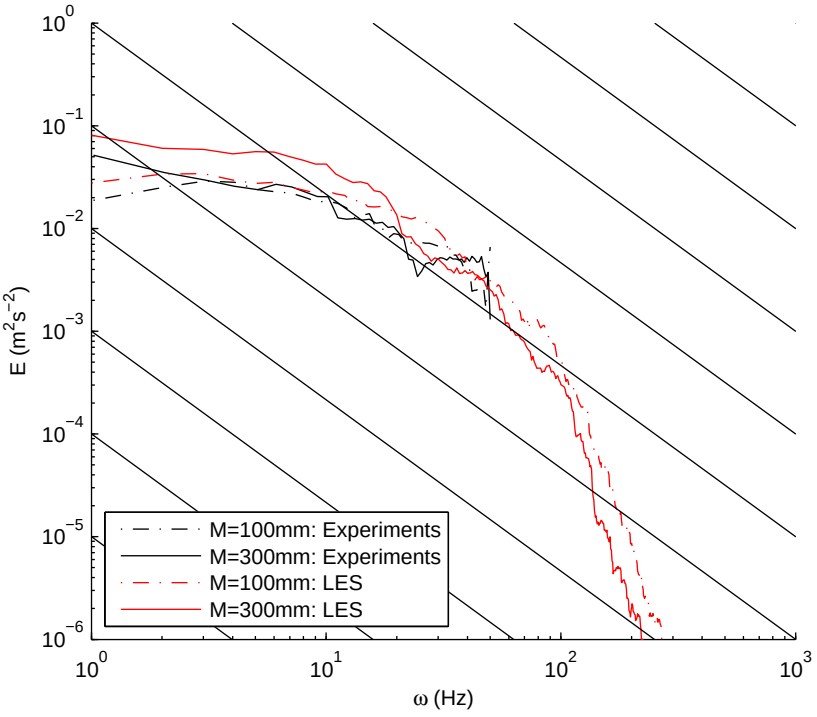

Figure 8.19: Energy spectra at 10 x/M downstream of the gridInlet compared to the experimental conditions.

8.5 Summary and implications

It has been shown how the new gridInlet technique can be used to generate isotropic turbulence with intensities up to 20 % and integral length scales that are dependent on the Reynolds number, or size of the inlet grid. The rate of growth of integral length scales compared well with wind tunnel studies. While the turbulence decay rate was higher than measured experimentally, it compared well with previous LES investigations and found to be independent of Reynolds number. The integral length scales were found to grow faster with increasing Reynolds number. The main findings and considerations of this chapter are summarised below.

- A cell density of 32×32 cells per length M should provide sufficient resolution.
- A triple inlet grid period, corresponding to a domain size of $3M \times 3M$, should be the minimum domain size to avoid constricting the growth of turbulent eddies.
- The turbulence intensity decay rate is independent of Reynolds number.
- Integral length scales are $\approx 0.5M$, with a higher growth rate for higher Reynolds number flows.
- Increasing the Reynolds number increases the energy contained in the lower frequency fluctuations, consistent with an increase in integral length scale.

This study has demonstrated how the gridInlet technique can be used to generate high intensity turbulence with specific length scales for LES. Through careful selection of grid size and inlet length different turbulence intensities and integral length scales may be generated. Comparisons have been made to the grid generated turbulence in the flume from the investigation of chapter 7. It was found that the experiments produced anisotropic turbulence that did not match the LES model due to the effects of upstream turbulence, the free-surface, and the bed boundary layer which increased $u'u'$. However, the LES model was found to produce uniform profiles of turbulence characteristics and is therefore suitable for the investigation of the effects of grid generated turbulence on the wake of an actuator disc.

This chapter has demonstrated how flows with different turbulence characteristics may be generated in LES. The next chapter builds on this method to develop a new technique for generating turbulence in LES actuator disc simulations where the structure of the generated turbulence may be controlled. This would be an extension of chapter 6 where turbulence sources were added in actuator disc RANS simulations.

Chapter 9

Turbulence generation in LES approximations of tidal turbines

9.1 Introduction

An extension of the uniform actuator disc rotor model has been developed to generate turbulence in large eddy simulations (LES), based on the principles of grid generated turbulence as discussed in the previous chapter. The characteristics of the generated turbulence may be controlled to study the effects of turbulence on the performance and wake profile of a device. The objective of this chapter is to demonstrate this new method and to provide a verification study on how the turbulence characteristics can be controlled, demonstrating the effects of device generated turbulence. This chapter has been published and was presented at the 10th European Wave and Tidal Energy Conference (Blackmore, Batten & Bahaj 2013*b*). The final results chapter incorporates the methods described in this chapter with the previous chapter to investigate the effects of free-stream turbulence on the wake profile of an actuator disc.

9.2 Turbine rotor modelling

The different methods of modelling turbine rotors within CFD simulations have been discussed in section 3.5. Full rotor and actuator line representations are impractical due to the vast computational requirements, while BEM actuator discs are limited by the availability of hydrofoil data sets when considering different turbulent flows. The uniform actuator disc has been used in RANS simulations and found to agree well with experimental data when a turbulence source is added. However, to investigate the effects of turbulent structure on the wake of a turbine an LES model is required. As discussed in the previous chapter, specifying turbulence sources in LES is difficult.

The proposed method to generates turbulence in LES actuator disc models is based on the idea of the gridded inlet discussed in the previous chapter. It is proposed that the momentum sink term is applied on a grid pattern across the actuator disc where the area averaged value is equal to the uniform actuator disc. Figure 9.1 shows the distribution of maximum and minimum momentum sink terms in the gridded actuator disc. The resulting shear between the maximum and minimum values of the momentum sink generate turbulence. The turbulence characteristics in the wake may be controlled be changing the grid parameters, such as the grid width, b. This allows the effects of device generated turbulence on the wake profile to be investigated.

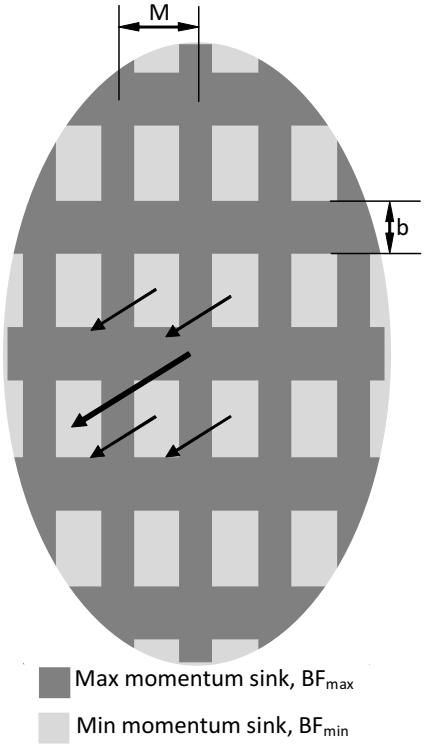

Figure 9.1: Graphical representation of the gridded actuator disc.

Table 9.1 compares the turbulence characteristics of the gridded actuator, uniform, BEM, actuator line and full rotor models. The actuator disc methods have the lowest computational requirements which becomes important for LES models that requirer finer meshes than RANS. Full rotor or actuator line representations are only feasible for single devices due to the computational requirements. The body forces for the BEM actuator disc are derived from 2D lift and drag data and is therefore limited by the availability of hydrofoil data sets for different flow conditions. The BEM actuator disc is therefore unable to show the effects of different turbulent flows on the wake and thrust of a device. Further, it is not possible to control the turbulence generated by the BEM actuator disc, which may differ in scale and intensity compared to the turbine rotor due to the above assumption. While the gridded actuator disc does not generate rotation in the flow, the rotation generated by the BEM actuator disc dissipates rapidly, and

beyond 4-5 diameters there is little rotation in the developed turbulence Wu & Porte-Agel (2011). The gridded actuator disc does allow the turbulent scale and intensity to be controlled by changing the bar width of the grid. This method could therefore be used to investigate the effects of different turbulence characteristics, generated by a device, for the optimisation of device spacing within arrays.

Table 9.1: Comparison of actuator disc models.

Turbulence characteristic	Actuator disc model				
	Gridded	Uniform	BEM	Actuator line	Full rotor
Generation	from shear generated between grid bars.	none	from rotation introduced at the disc.	from rotation of actuator line and body forces.	from rotation of blades and and flow separation from blade surface.
Control	length scales and intensities controlled with grid parameters (e.g. bar width).	none	none	none	none
Structure	approximately isotropic	none	with rotation up to $\approx$ 4 diameters downstream Wu & Porte-Agel (2011)	tip vortices and rotation of flow.	tip vortices and rotation of flow.
Required data	axial induction factor, grid parameters.	axial induction factor.	blade geometry, lift and drag data of blade sections.	blade geometry, lift and drag data of blade sections.	full blade geometry.

9.3 Numerical Domain and Method

The numerical domain is shown in figure 9.2 and has a low blockage ratio of $\approx 1.5\%$, where the blockage ratio is defined as the ratio of actuator disc area to total cross-sectional area. The inlet was uniform with inlet velocity of $U_\infty = 0.3$ m/s, the pipe walls were set as free slip, and the outlet was set to zero gradient. The domain was split into a mesh of hexahedral cells using the OpenFOAM® native meshing software blockMesh and snappyHexMesh OpenCFD (2012). Simulations were performed with an actuator disc on different mesh densities refined from 1 cell across the actuator disc region to 11 cells across the actuator disc thickness. It was found that a mesh density with a minimum of 4 cells across the disc thickness was required for mesh independence, as shown in figure 9.3, resulting in a mesh with a cell size of 0.5 mm in the disc region. The mesh expands to 1 mm cell size up to 6 D downstream and 2 mm cell size in the far wake resulting in a mesh with a total of 3.5×10^6 cells which are the same size in the x, y, z coordinate directions.

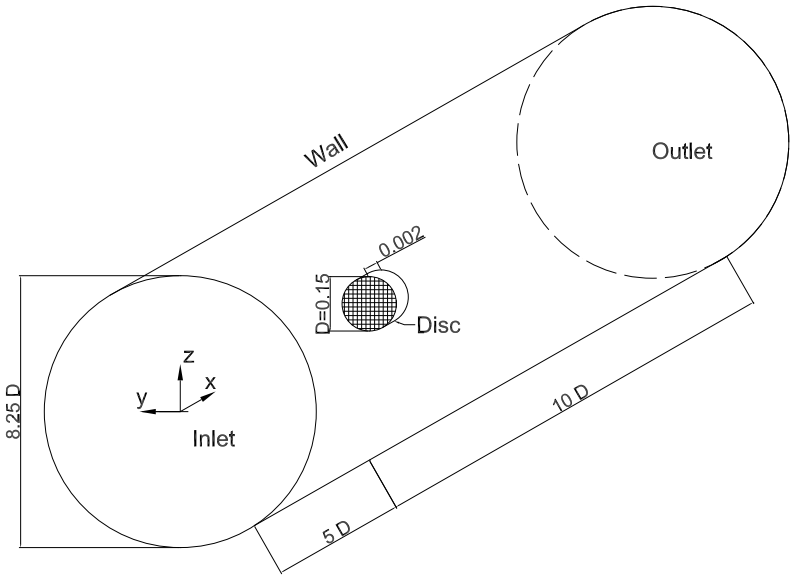

Figure 9.2: Schematic of numerical domain with low blockage ratio of less than 1.5 %.

Simulations were run using a steady-state, Reynolds Averaged Naviers-Stokes (RANS) simulation to solve the mean flow field. This was then used as the initial condition for transient Large Eddy Simulations (LES) to reduce convergence time. Simulations were run on 12 cores for 48 h on the IRIDIS high performance computer at the University of Southampton. A time step of $\Delta t = 0.08$ s was used and simulations run until the turbulence statistics converged, approximately 40 s. Comparisons have also been made between the steady state RANS and transient LES simulations which were run on the

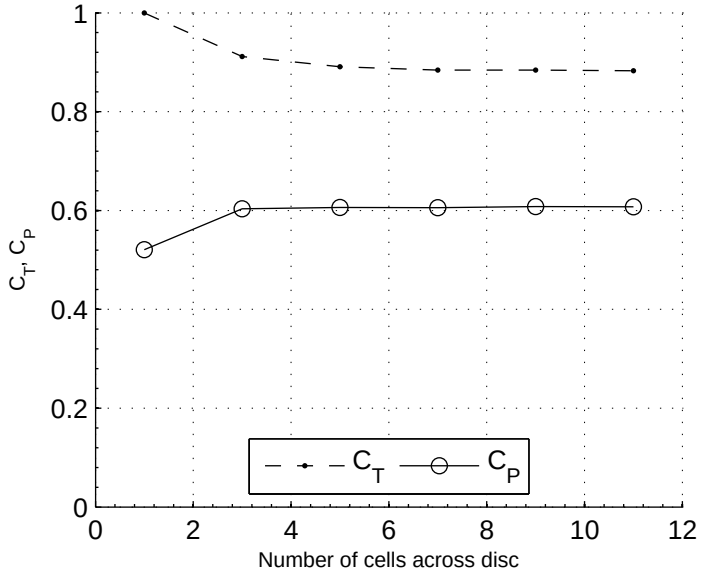

Figure 9.3: The effect of the number of cells across an actuator disc on thrust and power coefficients.

same mesh. The open source code OpenFOAM® 2.0.1 was used to solve the incompressible finite volume discretisation of the Reynolds Averaged (RANS) and filtered (LES) Navier-Stokes equations OpenCFD (2012).

9.3.1 Reynolds Averaged Navier-Stokes

A RANS simulation was performed using the $k - \epsilon$ turbulence model with the simpleFoam solver, which uses the SIMPLE algorithm for pressure-velocity coupling (Versteeg & Malalasekera 1995). Discretisation was performed using the second order central differencing method. This solution was then used as the initial condition for the LES model to reduce computational time.

9.3.2 Large Eddy Simulation

The pimpleFoam solver was used with a Smagorinsky turbulence model (OpenCFD 2012). The equations were spatially discretised using second order central differencing and temporally discretised using backward differencing. Refer to chapter 3 for full details of the governing equations and LES methodology.

9.3.3 Turbine momentum sink term and performance coefficients

For a uniform actuator disc the momentum sink term, F_B, is applied uniformly throughout the volume occupied by the turbine rotor as discussed in section 3.5. However, for

the proposed gridded actuator disc the momentum sink term is split into a maximum and minimum value and applied on a grid pattern as shown in figure 3.3(a) such that the average momentum sink is equivalent to the uniform case.

$$F_{B_{max}} = \alpha F_B. \tag{9.1}$$

$$F_{B_{min}} = \beta F_B. \tag{9.2}$$

where α and β are the maximum and minimum momentum sink factors respectively. The porosity, θ, or open area ratio of the grid pattern is defined as the ratio of area with minimum momentum sink to the total area of the disc as described by equation 2.30. A porosity of $\theta = 0.5$ was used which results in the momentum sink factors being related by:

$$\frac{\alpha + \beta}{2} = 1. \tag{9.3}$$

The momentum sink ratio, r, is defined as:

$$r = \frac{\alpha}{\beta}. \tag{9.4}$$

9.3.4 Investigation plan

The results in this chapter are verification results to show how the different parameters affect the gridded actuator. Table 9.2 shows the parameters and values used for each part of the results section. In each case simulations were first run using the RANS solver to obtain the steady state solution. This solution was then used as the initial condition for the LES solver to obtain the turbulence characteristics generated by the gridded disc. Thrust coefficients and axial induction factors from the RANS and LES models are compared.

Table 9.2: Investigation plan and parameter settings.

Results section	r	a	b (mm)
Momentum sink ratio	1-3	0.3	5
Axial induction factor	2	0.1-0.35	5
Bar width	2	0.3	5-15

9.4 Results and Discussion

This section presents the results from running gridded actuator disc simulations. The results in this chapter are for the verification of this method to show how the parameters controlling the gridded actuator disc affect the thrust, velocity deficit, turbulence intensity and integral length scale. The results have been split into three sections covering the effects of momentum sink ratio, axial induction factor and grid bar width as detailed in table 9.2. Each section considers the effects on thrust coefficient and axial induction factor (for both RANS and LES), the effects on the velocity deficit, turbulence intensity and integral length scale in the wake (for LES only).

9.4.1 Momentum sink ratio, r

The set axial induction factor was set at 0.3 with a bar width of 10 mm, or $b = D/15$. The momentum sink ratio was then varied for $1.04 < r < 3.00$ where $r = 1$ corresponds to a uniform disc. Figure 9.4 shows that the thrust coefficient is approximately constant up to a momentum sink ratio of 1.70. For ratios above 1.70 the thrust coefficient increases from approx 0.85 to 0.94. The thrust coefficient was higher for LES than RANS.

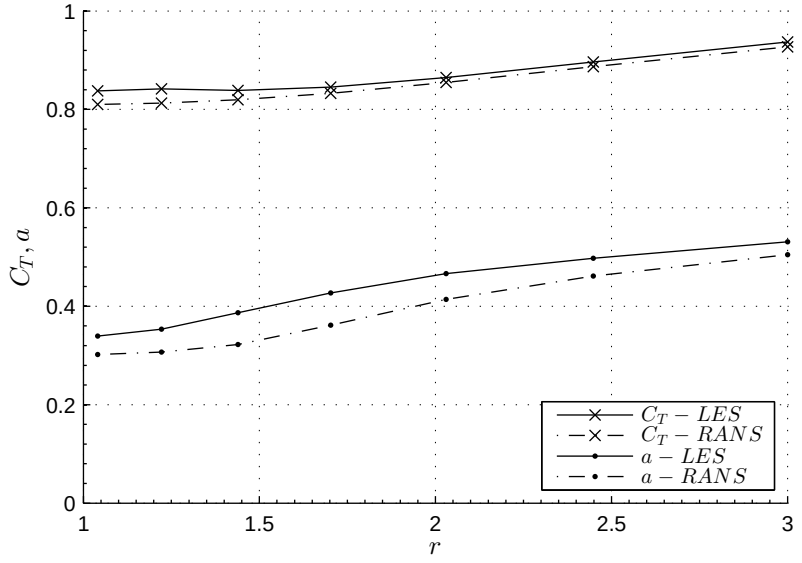

Figure 9.4: Effects of momentum sink range on the thrust coefficient and axial induction factor for RANS and LES gridded actuator disc simulations.

The measured axial induction factors were typically 10 % higher for LES than RANS. This implies the flow is slowed more though the gridded actuator disc for LES than RANS. The axial induction factor increases with momentum sink ratio, although the measured axial induction factor increases more rapidly for $r > 1.4$. This can be seen in figure 9.5 where there is a larger deficit in the near wake, less than 4 diameters, as the momentum sink ratio increases. Note, for the largest momentum sink ratios the velocity

deficit exceeds 1 indicating flow reversal. However, further downstream the velocity deficit is lower for larger ranges.

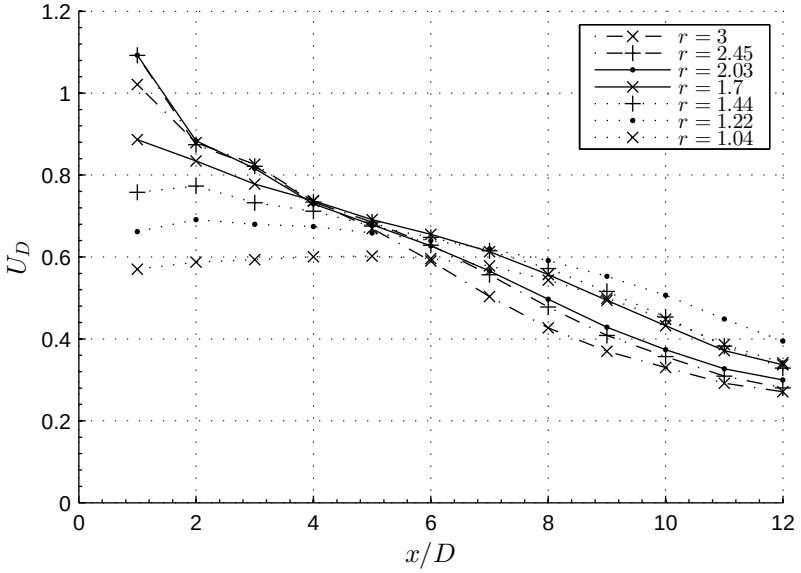

Figure 9.5: Effects of momentum sink range on the velocity deficit of LES gridded actuator disc simulations.

The differences in velocity deficit can be explained by considering the turbulence intensity behind the gridded actuator disc in figure 9.6. It can be seen the turbulence intensity is higher for a larger ratio, which would increase the rate of mixing between the wake and free-stream causing the wake to recover more quickly. 10-12 diameters downstream the decay rate of turbulence, gradient, is similar for all ranges with intensities of 10 ± 2.5 %. It can also be seen that the turbulence intensities for the larger momentum sink ratios become very large close to the disc. This is due to the velocity being close to zero as represented by velocity deficits close to one for these cases.

It can be seen in figure 9.7 that the momentum sink ratio has little effect on the integral length scale which has grown from $\ell_x/D = 0.16 \pm 0.04$ at $5x/D$ to $\ell_x/D = 0.31 \pm 0.04$ at $10x/D$.

Overall, increasing the momentum sink ratio increases the turbulence intensity in the near wake increasing the velocity deficit, but has no effect on the integral length scale. However, as the turbulence intensity is higher the wake recovers more quickly resulting in lower velocity deficits in the far wake. The increase in momentum sink ratio results in larger thrust coefficients and axial induction factors. It is postulated that this is an effect of the increased generation of turbulence energy at the expense of fluid momentum increasing the velocity drop across the disc, hence increasing the thrust. The LES model showed higher axial induction factors than the RANS model which is likely to be a result of the resolved turbulence dissipating more energy, reducing the velocity and hence increasing thrust.

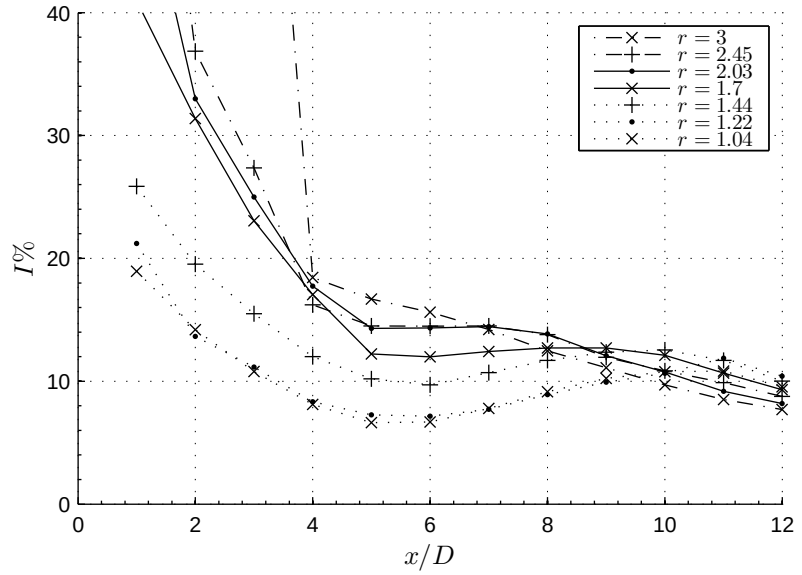

Figure 9.6: Effects of momentum sink range on the turbulence intensity of LES gridded actuator disc simulations.

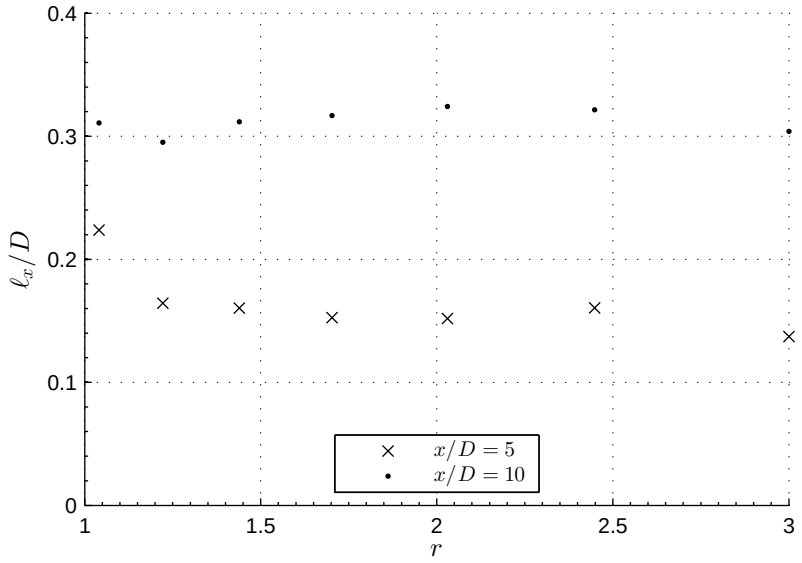

Figure 9.7: Effects of momentum sink ratio on the integral length scale of LES gridded actuator disc simulations.

9.4.2 Axial induction, a

This section presents results on the effects of the set axial induction factor used to calculate the momentum sink term. The momentum sink ratio is constant, $r = 2$, throughout the simulation allowing different flow conditions, such as turbulence or blockage effects, to cause the measured axial induction factor to differ from the set value.

Figure 9.8 shows the thrust coefficient increases with increasing set axial induction factor. The thrust measured for the LES model is greater than the RANS model for axial

induction factors less than 0.25. The measured axial induction factor is approximately equal to the set value for $a < 0.2$. As the set axial induction factor increases the measured axial induction becomes greater than the set value, with the LES model producing higher axial induction factors than the RANS model. This is consistent with an increase in velocity deficit with increasing set axial induction factor showing a greater reduction in velocity across the disc. For large axial induction factors flow reversal occurs at $x/D = 1$ in the near wake. However, for axial induction factors less than 0.2 there is little wake recovery and the velocity deficit is almost constant to 12 diameters downstream. The cause of this is very low turbulence generation for axial induction factors less than 0.2, as seen in figure 9.10, resulting in little wake mixing. Increasing the set axial induction factor increases the turbulence intensity, dissipating more of the fluids energy as turbulence and the velocity across the disc is further reduced. Therefore the measured axial induction factor increases and is larger than the set value.

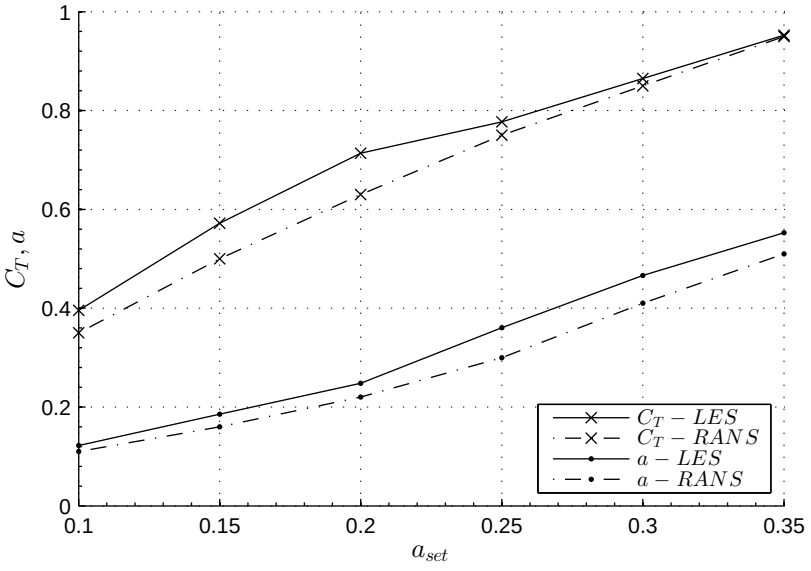

Figure 9.8: Effects of set axial induction factor on the thrust coefficient and axial induction factor for RANS and LES gridded actuator disc simulations.

Figure 9.11 shows the integral length scales for $a < 0.2$ produced unrealistic values of ℓ_x/D up to 15.5. The cause of this is unknown but likely to be due to the low levels of turbulence fluctuations. It is likely that the momentum sink ratio would need to be increased for low axial induction factors to increase the turbulence generation. However, for most cases the axial induction factor would be higher. Setting $a = 0.3$ produces axial induction factors of 0.4 and 0.47 for RANS and LES models respectively.

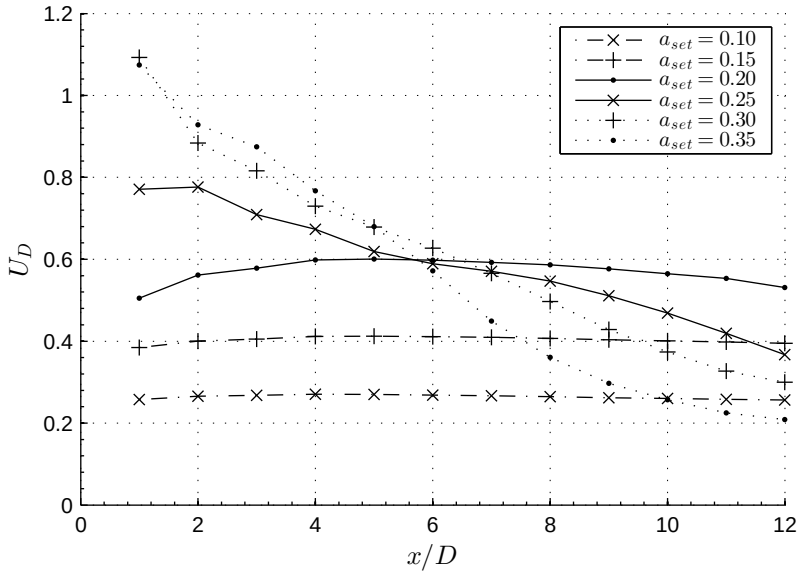

Figure 9.9: Effects of set axial induction factor on the velocity deficit of LES gridded actuator disc simulations.

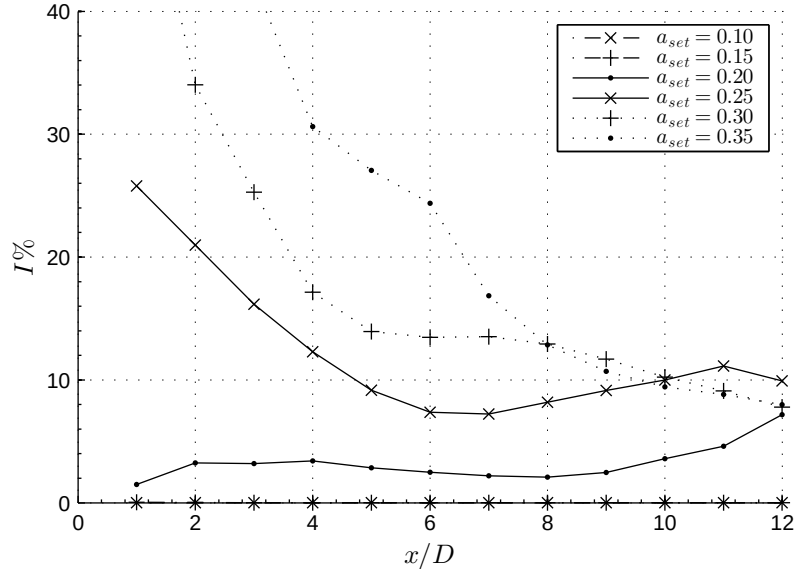

Figure 9.10: Effects of set axial induction factor on the turbulence intensity of LES gridded actuator disc simulations.

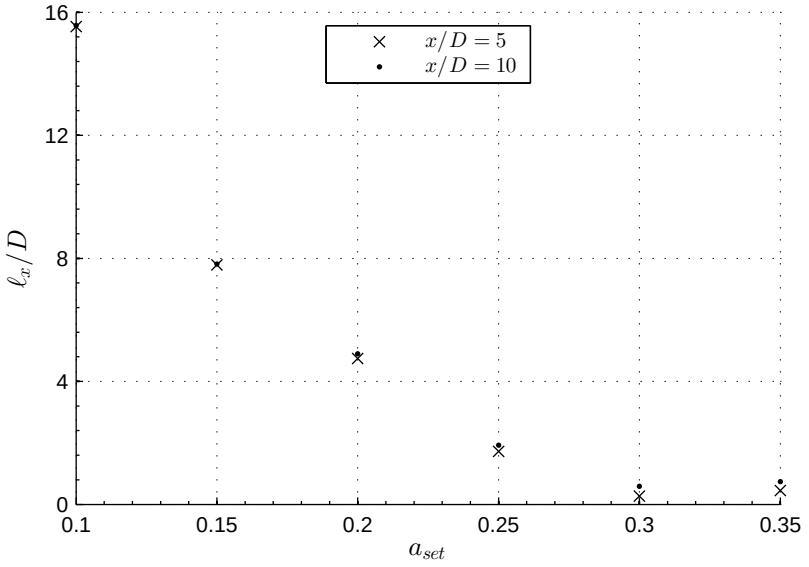

Figure 9.11: Effects of set axial induction factor on the integral length scale of LES gridded actuator disc simulations.

9.4.3 Grid bar size, b

Using an axial induction factor of 0.3 and a momentum sink ratio of 2, the grid bar width was varied. Figure 9.12 shows 3D contours of vorticity with magnitude 8 Hz and a centre plane showing contours of velocity deficit for the two cases with $b = 5$ mm and $b = 15$ mm representing the cases with small scale turbulence generation and large scale turbulence generation respectively. The effects of the grid pattern can be seen in the velocity deficit in the near wake just behind the disc. It can be seen in figure 9.12(a) with small scale turbulence that the velocity deficit is higher further downstream with less spreading and breaking up of vortices when compared to 9.12(b) with larger scale turbulence. This figure demonstrates the capabilities of this modelling technique showing the resolved turbulent structure and the time-averaged wake profile that is typical of a RANS model.

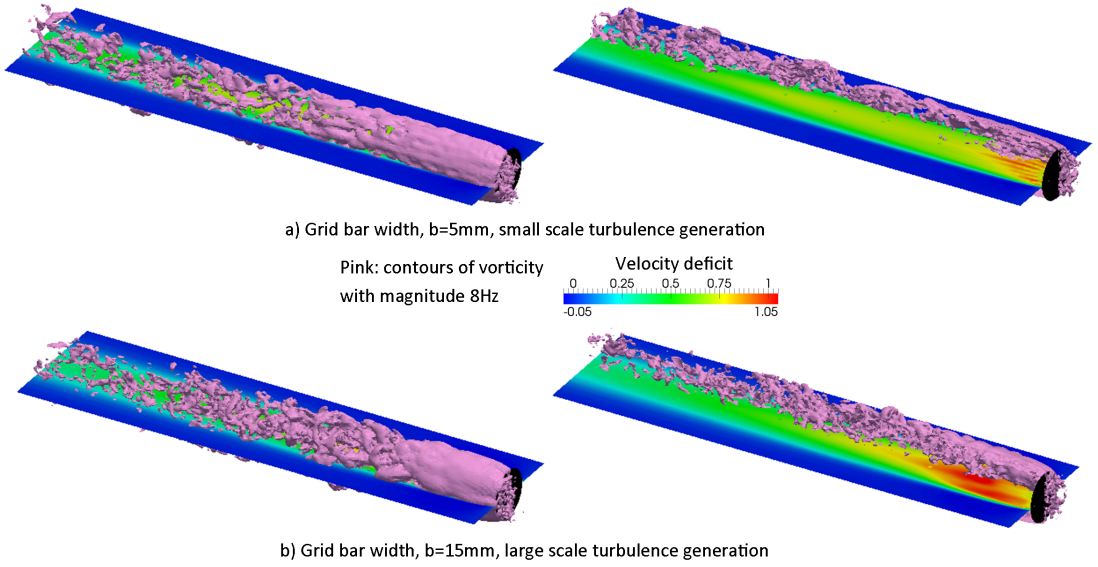

Figure 9.12: Contours of vorticity with magnitude 8 Hz and velocity deficit for bar widths of $b = 5$ mm and $b = 15$ mm.

It can be seen in figure 9.13 that the thrust coefficient is approximately constant at 0.86 for both RANS and LES, but the axial induction factor increases by $\approx 12\%$ as the bar width increases from 5-15 mm. Again, the LES model produces higher axial induction factors than the RANS model by approximately 10%.

Figure 9.14 shows that the wake recovery is faster for a larger grid bar resulting in lower velocity deficits after 4 diameters downstream. Again, there is flow reversal indicated by $U_D > 1$ at $x/D = 1$ which could be a result of the measurement point being directly downstream of a grid bar. Figure 9.15 shows that the turbulence intensity less than 6 diameters downstream is greater for larger grid bars. Note, the turbulence intensity tends to very large values close to the disc due to the velocity being close to zero represented by velocity deficits close to one. Further, the integral length scales grow

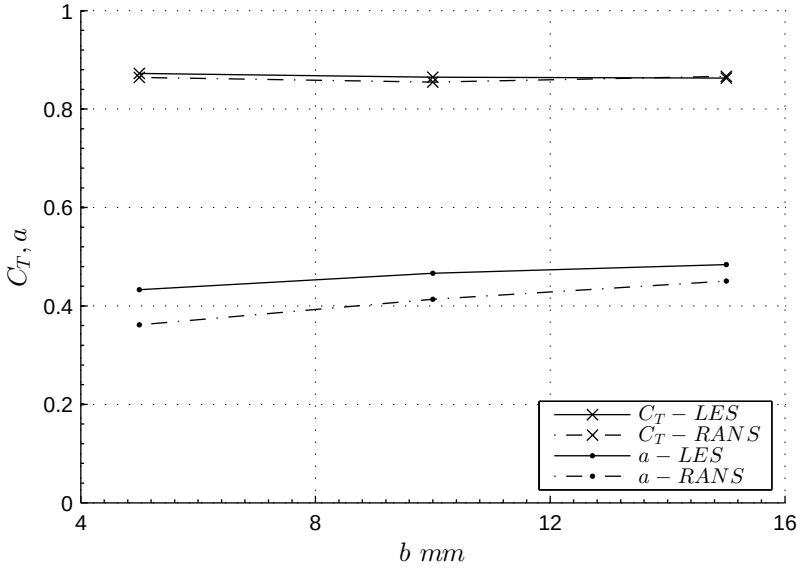

Figure 9.13: Effects of grid bar width on the thrust coefficient and axial induction factor for RANS and LES gridded actuator disc simulations.

larger downstream for a wider bar, as seen in figure 9.16 and in figure 9.12 with larger spreading of the vortices for a larger grid bar. It is the increase in turbulence, increasing the rate of mixing between the wake and free-stream that causes the wake to recover faster.

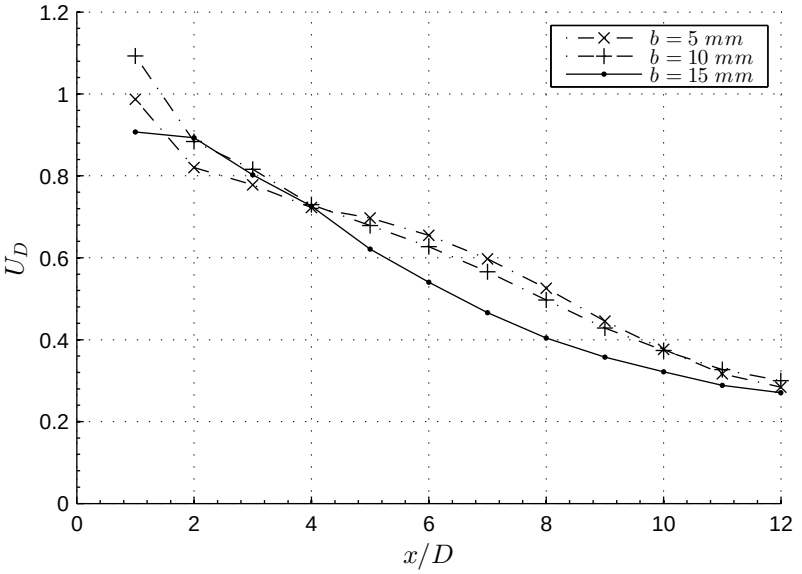

Figure 9.14: Effects of grid bar width on the velocity deficit of LES gridded actuator disc simulations.

The significance of this result may be considered with reference to the tip-speed ratio (TSR) of a turbine. A turbine operating at a low TSR will generate low frequency turbulent fluctuations and therefore larger integral length scales. A turbine operating at high TSR would generate higher frequency fluctuations and lower integral length scales.

Therefore a turbine operating at a lower TSR would generate larger scales of turbulence and may be positioned closer together within an array, which would increase the power output of the array for a given area.

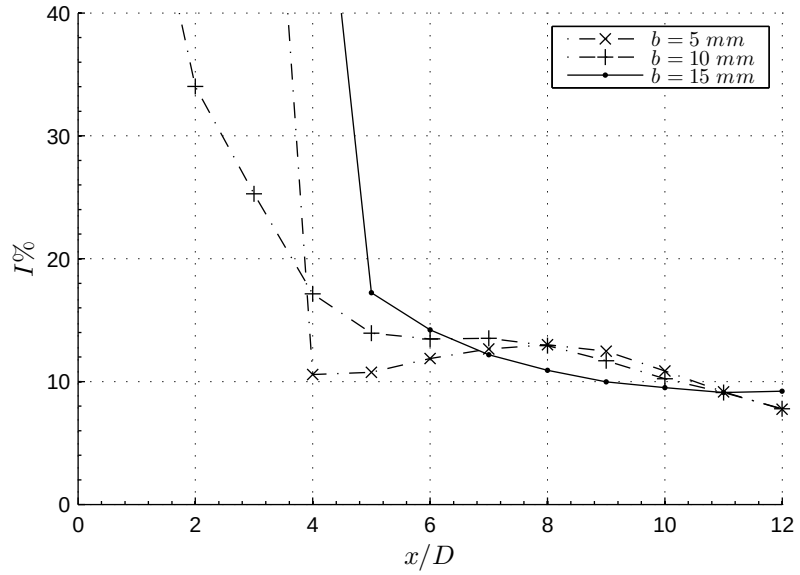

Figure 9.15: Effects of grid bar width on the turbulence intensity of LES gridded actuator disc simulations.

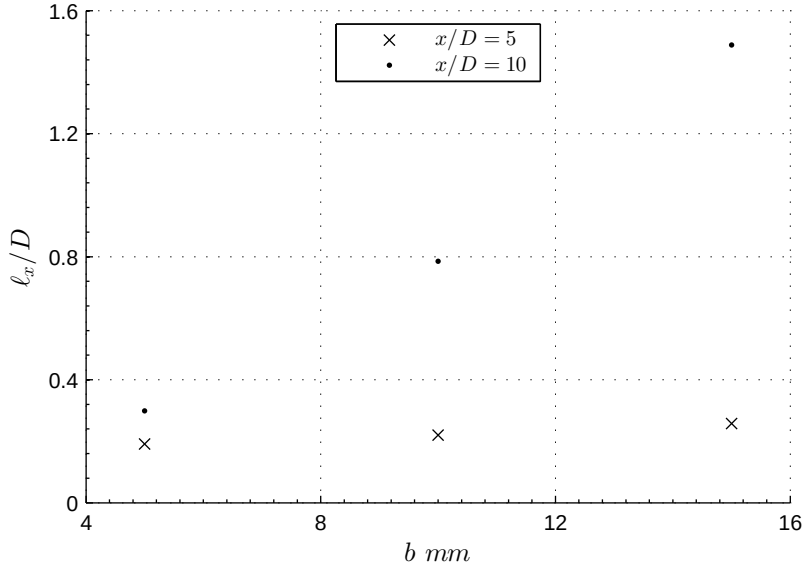

Figure 9.16: Effects of grid bar width on the integral length scale of LES gridded actuator disc simulations.

9.5 Summary and implications

It has been shown that turbulence may be generated in LES actuator disc simulations by applying the momentum sink on a grid pattern, defined as a gridded actuator disc. The

advantage of this method is that the turbulence characteristics generated by the disc may be controlled by changing the grid parameters. It was shown that a device generating higher turbulence intensities and larger length scales, corresponding to a device operating at a lower tip-speed ratio, results in a faster wake recovery. This allows devices to be located closer together, increasing the number of devices in an array for a given area. The results also show that higher thrust and axial induction factors are measured for transient large eddy simulations compared to steady state Reynolds averaged Navier-Stokes simulations. It is postulated that this effect is due to the resolved turbulence dissipating more energy resulting in the flow being more greatly retarded through the disc.

This chapter has shown how turbulence can be generated in an LES actuator disc model and how the generated turbulence can affect the wake recovery. The next chapter considers the effects of ambient turbulence on the wake of a gridded actuator disc to explain how turbulence affects the wake recovery.

Chapter 10

Influence of turbulence intensity and integral length scale on the wake of an actuator disc

10.1 Introduction

This chapter brings together the developments of the previous two chapters to investigate the effects of turbulent structure on the wake profile of an actuator disc. Limited wake data was obtained from the experimental investigation presented in chapter 7, but CFD models can provide vast amounts of information on the wake profile and velocity measurements across the whole domain that would be infeasible to obtain experimentally. The gridInlet is used, as described in chapter 8, to generate inlet conditions with different integral length scales and turbulence intensities. The gridInlets are based on those used in the experiments with mesh spacings of $M = 100$ mm and $M = 300$ mm. A gridded actuator disc, as described in chapter 9, was introduced into the isotropic turbulent flows so the effects of ambient turbulence intensity and integral length scale could be assessed. Comparisons have then been made to the experimental results of chapter 7 to assess the effects of anisotropic turbulence in comparison to isotropic turbulence. Finally, comparisons have been made to published experimental data to validate the results of this model.

10.2 Numerical Domain and Method

The numerical domain is shown in Fig. 10.1 and is based on the flume experiments from chapter 7. The domain has a low blockage ratio of less than 1.5 %, where the blockage ratio is defined as the ratio of actuator disc area to total cross-sectional area, this is the

same blockage ratio as used to develop the gridded actuator disc presented in chapter 9. Two different inlets were used, the first was a uniform inlet with velocity of $U_\infty = 0.3$ m/s, and the second a gridInlet with spacings of $M = 100$ mm and $M = 300$ mm comparable to the grids used for the experimental investigation as discussed in chapter 8. The walls, bottom and surface were set as free slip due to the uniform velocity profiles recorded behind the grids in the experiments, therefore the effects of the boundary were assumed to be negligible. Finally the the outlet was set to zero gradient.

The domain was split into a mesh of hexahedral cells using the OpenFOAM® native meshing software blockMesh and snappyHexMesh OpenCFD (2012). The meshes were generated based on the findings of the previous two chapters and used 4 cells across the disc thickness, as required for mesh independence, resulting in a mesh with minimum cell size of 0.5 mm. A gridded disc was used with set axial induction factor of 0.3, body force ratio of 2, a bar width of 0.01 with bar porosity of 0.5 as found from the previous chapter.

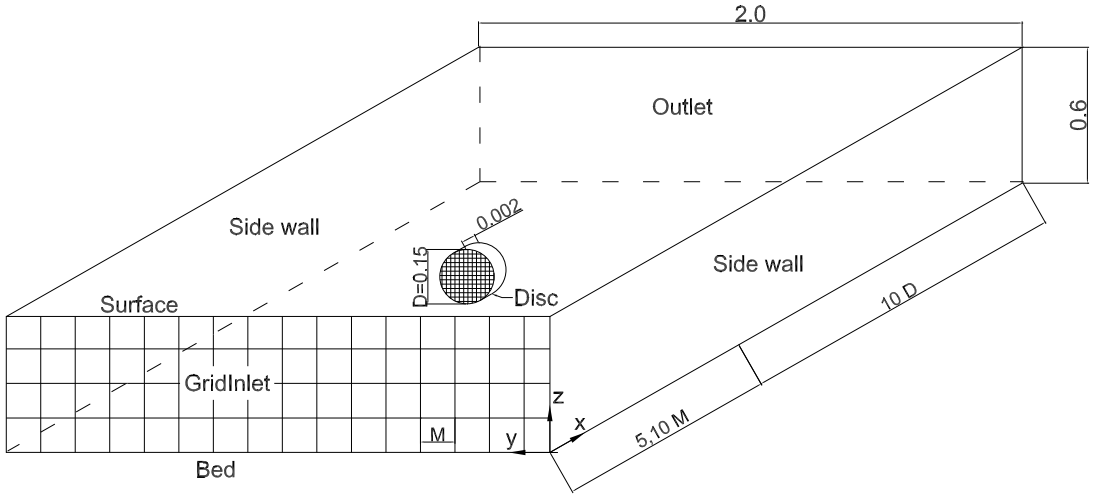

Figure 10.1: Numerical domain for investigating the effects of turbulence on the wake of an actuator disc. All dimensions in meters.

Simulations were run using a steady-state RANS simulation to obtain an initial condition for the LES model to reduce simulation time. A time step of $\Delta t = 0.001$ s was used and simulations run until the turbulence statistics converged, approximately 40 s. The open source code OpenFOAM® 2.0.1 was used solve the incompressible finite volume discretisation of the RANS and LES equations OpenCFD (2012). The $k - \epsilon$ turbulence model with the simpleFoam solver which uses the SIMPLE algorithm for pressure-velocity coupling to numerically solve the RANS equations. Discretisation was performed using the second order central differencing method. This solution was then used as the initial condition for the LES model to reduce computational time. The pimpleFoam solver was used with a Smagorinsky turbulence model (OpenCFD 2012) to numerically solve the LES equations. The equations were spatially discretised using second order central

differencing and temporally discretised using backward differencing. Refer to chapter 3 for full details of the governing equations and CFD methodology.

The effects of integral length scale and turbulence intensity on the wake profile are investigated with isotropic turbulence behind the gridInlet for five different cases detailed in table 10.1. The results are then compared to the experimental investigation of chapter 7 with anisotropic turbulence. Finally, comparisons are made to published experimental data obtained behind model turbines and porous discs to demonstrate the validity of this model.

Table 10.1: Details of numerical domain and gridInlet for different cases run.

Case	GridInlet size M (mm)	Downstream location, x/M	Turbulence intensity, I	Integral length scale, ℓ_x/D	Number of cells
1	-	-	0	0	$\approx 8.7 \times 10^6$
2	100	5	11.7	0.25	$\approx 8.7 \times 10^6$
3	100	10	5.6	0.27	$\approx 10 \times 10^6$
4	300	5	11.3	0.55	$\approx 9.5 \times 10^6$
5	300	10	6.6	0.82	$\approx 12 \times 10^6$

10.3 Effects of isotropic turbulence

This section presents the results and discussion on how isotropic ambient turbulence affects the wake profile behind a gridded actuator disc. Figure 10.2 shows the mean velocity deficit for the three cases with zero, low and high levels of turbulence and the resolved turbulent structure as 3D contours of vorticity magnitude. It can be seen that increasing the turbulence intensity with small length scales (figure 10.2(b)) reduces the velocity deficit in the wake, but the wake width does not significantly increase over the zero turbulence case (figure 10.2(a)). However, increasing the integral length scale (figure 10.2(c)) initially increases the velocity deficit in the near wake but the wake width is increased resulting in a lower velocity deficit in the far wake and faster wake recovery. This can also be seen by the vorticity contours breaking up and spreading with larger scale turbulence over the zero turbulence case. The following results sections first consider the centreline profile before specific consideration of how the turbulence intensity and integral length scale affect the wake behind an actuator disc.

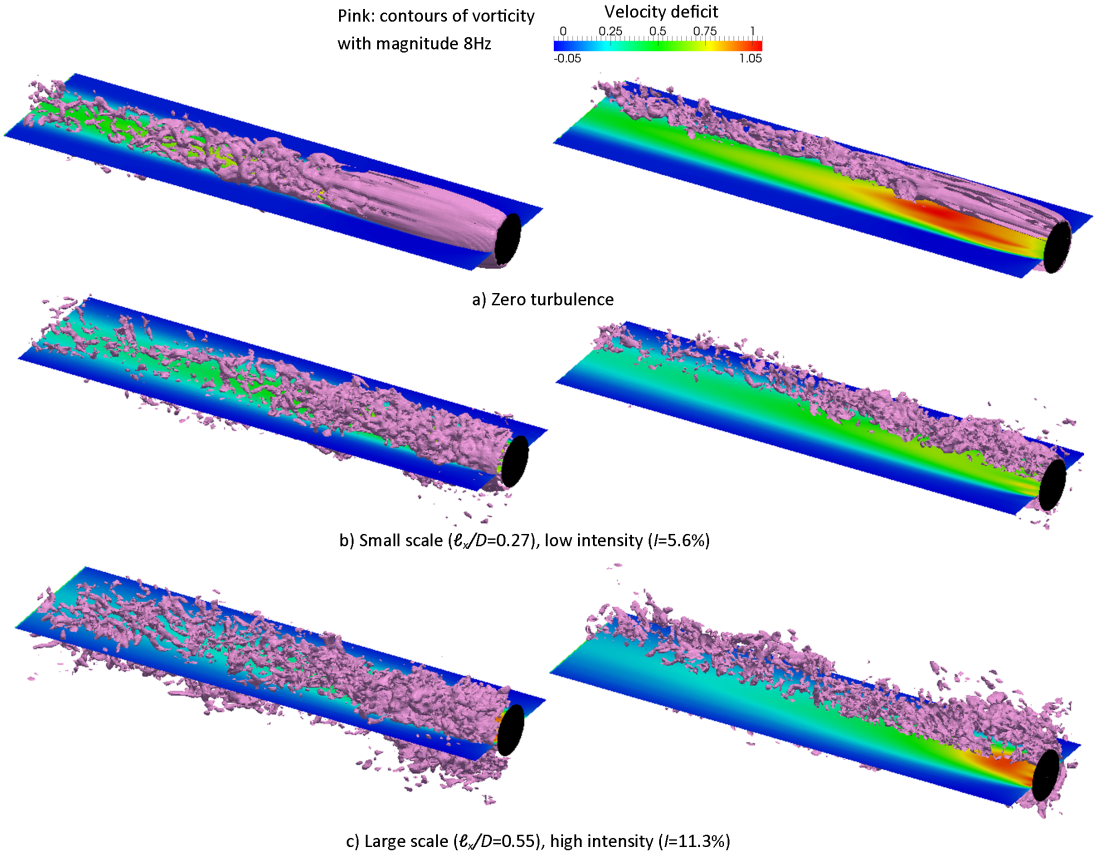

Figure 10.2: Contours of mean velocity deficit and 3D contours of vorticity magnitude for zero turbulence (top), small length scale low intensity turbulence (middle) and high intensity large length scales (bottom).

10.3.1 Centreline profiles for cases 1 - 5

Figure 10.3 shows the centreline profiles of velocity deficit, turbulence intensity and integral length scale for cases 1-5. It can be seen in figure 10.3(a) that the greatest velocity deficit, $U_D > 1$ at 2.7D, is recorded for case 1 with zero ambient turbulence and $U_D > 0.4$ at 10D downstream. Note, a velocity deficit greater than 1 indicates flow reversal. In all other cases with ambient turbulence the maximum velocity deficit is less than 1 and the wake recovery is much faster, $U_D \approx 0.1 - 0.3$ at 10D downstream. This shows that tests performed with very low or zero turbulence, such as in a towing tank, may produce significantly different flow regimes and wake profiles than expected in a turbulent flow, as also seen by the spreading of vortices behind the gridded actuator disc in figure 10.2.

Comparing cases 2 and 3 it can be seen that reducing the turbulence intensity increases the velocity deficit and shifts the point of maximum deficit further downstream of the gridded actuator disc. It can also be seen that increasing the integral length scale, cases 2 and 4, increases the maximum velocity deficit and shifts the point of maximum

velocity deficit closer to the gridded actuator disc. However, increasing the integral length scale speeds up the wake recovery such that further downstream the velocity deficit is lower for larger integral length scales. So high intensity flows with large integral length scales produce the fastest wake recovery with the point of maximum deficit closer to the actuator disc. These results are consistent with the findings of Harrison (2011) where higher power outputs were recorded in an array of turbines when the ambient turbulence intensity was increased suggesting the wake recovery was faster.

Figure 10.3(b) shows the turbulence intensity downstream of the gridded actuator disc. Although differences exist close to the disc in the near wake, for $x/D < 5$, further downstream the turbulence intensity is comparable for each case. However, it can be seen in figure 10.3(c) that the integral length scales in the wake of the actuator disc are comparable for ambient flows with similar ambient turbulence intensities. For ambient flows with $I \approx 5$ % the length scales grow to $\ell_x/D \approx 0.35$ at 10D downstream. For $I \approx 10$ % the length scales behind tha actuator discs grow to $\ell_x/D \approx 0.55$ at 10D. This suggests that the turbulence intensity in the wake is controlled by the actuator disc only, while the integral length scales in the wake are a function of the actuator disc and turbulence intensity of the ambient flow. This makes sense considering the wake mainly contains the low momentum fluid that has passed through the actuator disc, as such the actuator disc would directly influence the turbulence characteristics in the wake. This is in agreement with the results of the previous chapter where it was found the wake recovery was faster for a gridded actuator disc with larger bar size as it produced larger integral length scales in the wake. Further downstream as the wake continues to mix with the ambient flow the turbulence characteristics would start to resemble those of the ambient conditions.

The next sections further consider the effects of turbulence intensity and integral length scale to explain why the wake profiles are affected by the ambient turbulence conditions.

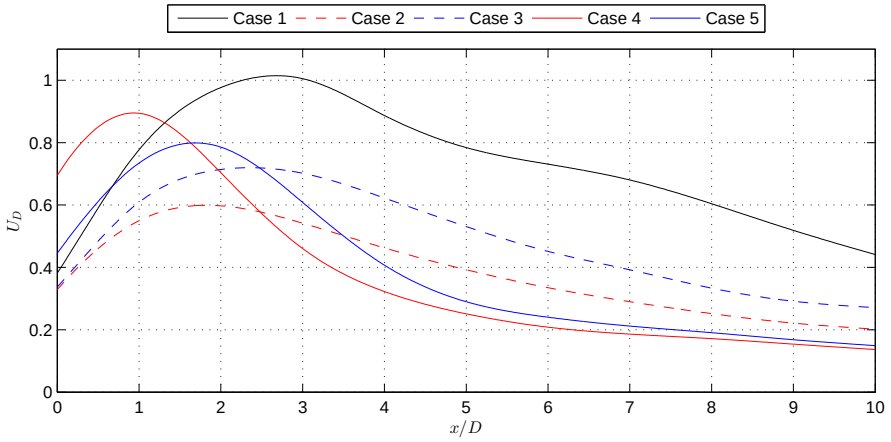

(a) Velocity deficit

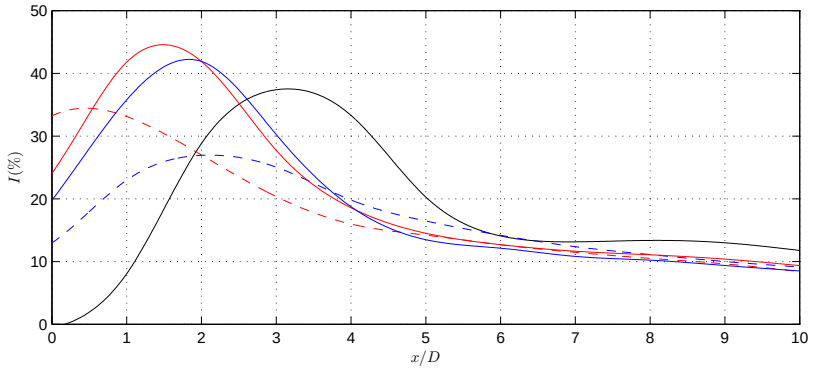

(b) Turbulence intnesity

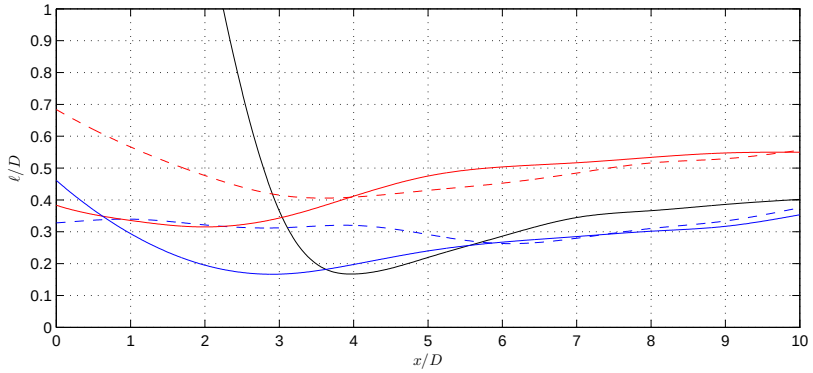

(c) Integral length scale

Figure 10.3: Velocity deficit, turbulence intensity and integral length scale downstream of a gridded actuator disc with different turbulence conditions.

10.3.2 Effects of turbulence intensity on wake profile, cases 1-3

The previous section showed that increasing the turbulence intensity reduced the velocity deficit and shifted the position of maximum deficit closer to the disc. Figure 10.4 shows the velocity profiles parallel to the z-axis at 2,4,6, and 10D downstream of the disc for

cases 1-3 with $\approx 0, 5, 10$ % turbulence intensity respectively. It can be seen that, in all locations downstream, increasing the turbulence intensity reduces the velocity deficit.

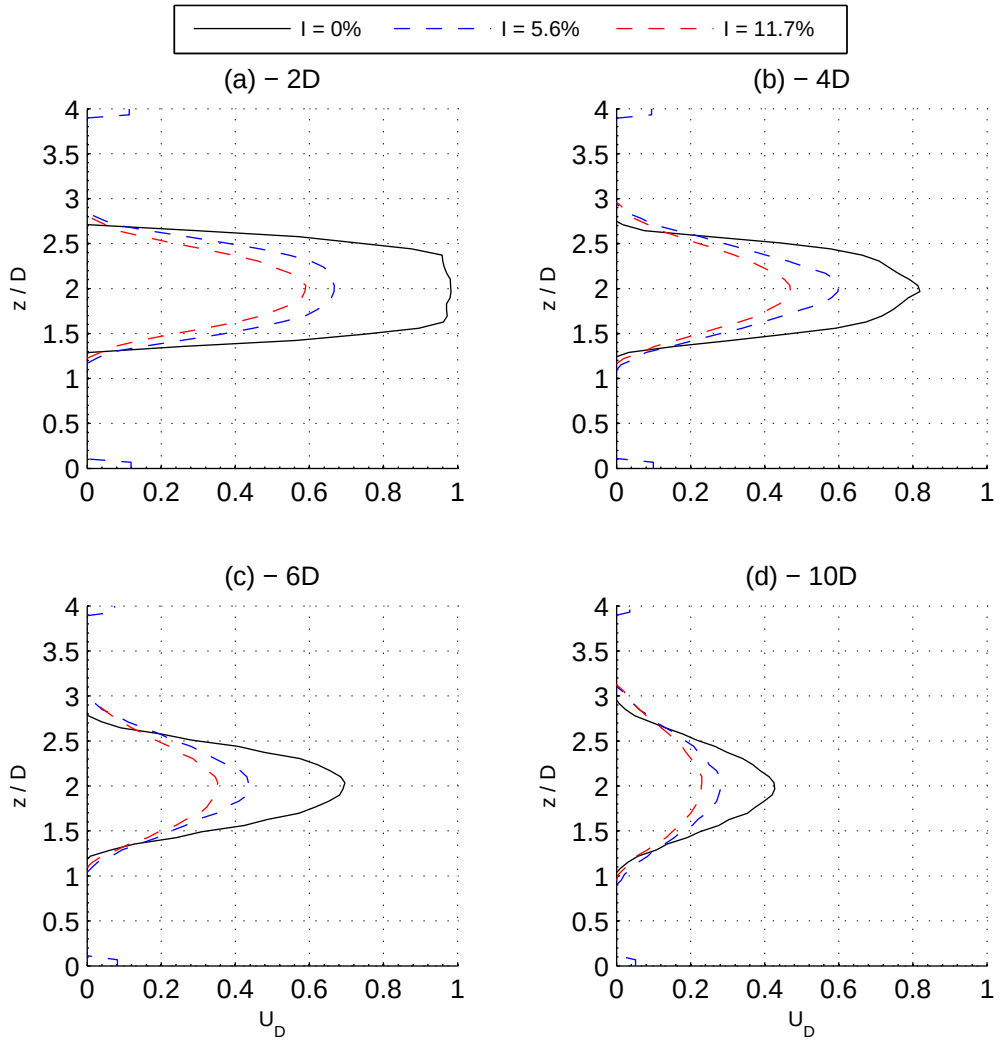

Figure 10.4: Velocity deficit at 2,4,6,10D downstream of an actuator disc with different turbulence intensity.

Figure 10.5 shows profiles of $u'u'$ for cases 1-3. It can be seen that initially $u'u'$ is larger across the center of the disc for higher ambient turbulence intensity, but further downstream $u'u'$ becomes lower for for the higher ambient turbulence intensity case. Profiles of $v'v'$ and $w'w'$ show similar trends due to the isotropic turbulence. Refer to appendix C.2 for all 6 components of Reynolds stress. While $u'v'$ and $v'w'$ are approximately zero, the profiles of $u'w'$ shows similar trends to the profile of $u'u'$ as shown in figure 10.6. Initially $u'w'$ is comparable for both cases with ambient turbulence but further downstream $u'w'$ becomes lower for the higher ambient turbulence intensity case. A faster wake recovery is observed for higher turbulence intensities due to the larger $v'v'$ and $w'w'$ components that are responsible for mixing the high momentum fluid of the free stream with the low momentum fluid in the wake. However, considering

the width of the wake as seen by the peaks in the profiles of $u'w'$, and shown in figure 10.7 as the edge of the wake where $U_w = 0.95U_\infty$ or $U_D = 0.05$, it can be seen that increasing turbulence intensity has little effect on the width of the wake, although the wake width is slightly increased over the zero turbulence case which is consistent with the RANS investigation of Nishino & Willden (2012).

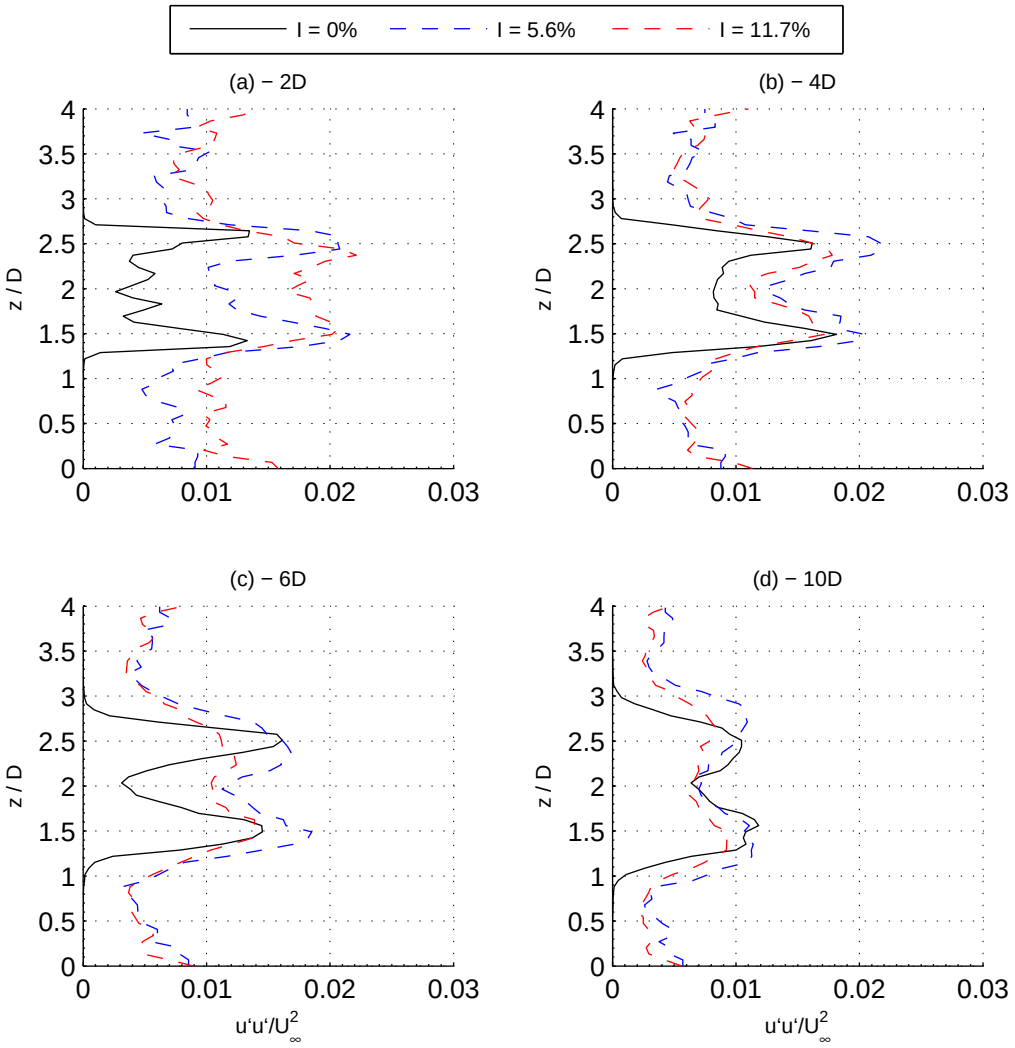

Figure 10.5: Velocity fluctuations ($u'u'$) at 2,4,6,10D downstream of an actuator disc with different turbulence intensity.

Overall it has been shown that increasing the turbulence intensity reduces the velocity deficit in the wake due to larger $v'v'$ and $w'w'$ components resulting in faster wake mixing with the high momentum free stream flow. However, the wake width is largely unaffected by turbulence intensity. The next section considers the affects of integral length scale on the wake profile behind a gridded actuator disc.

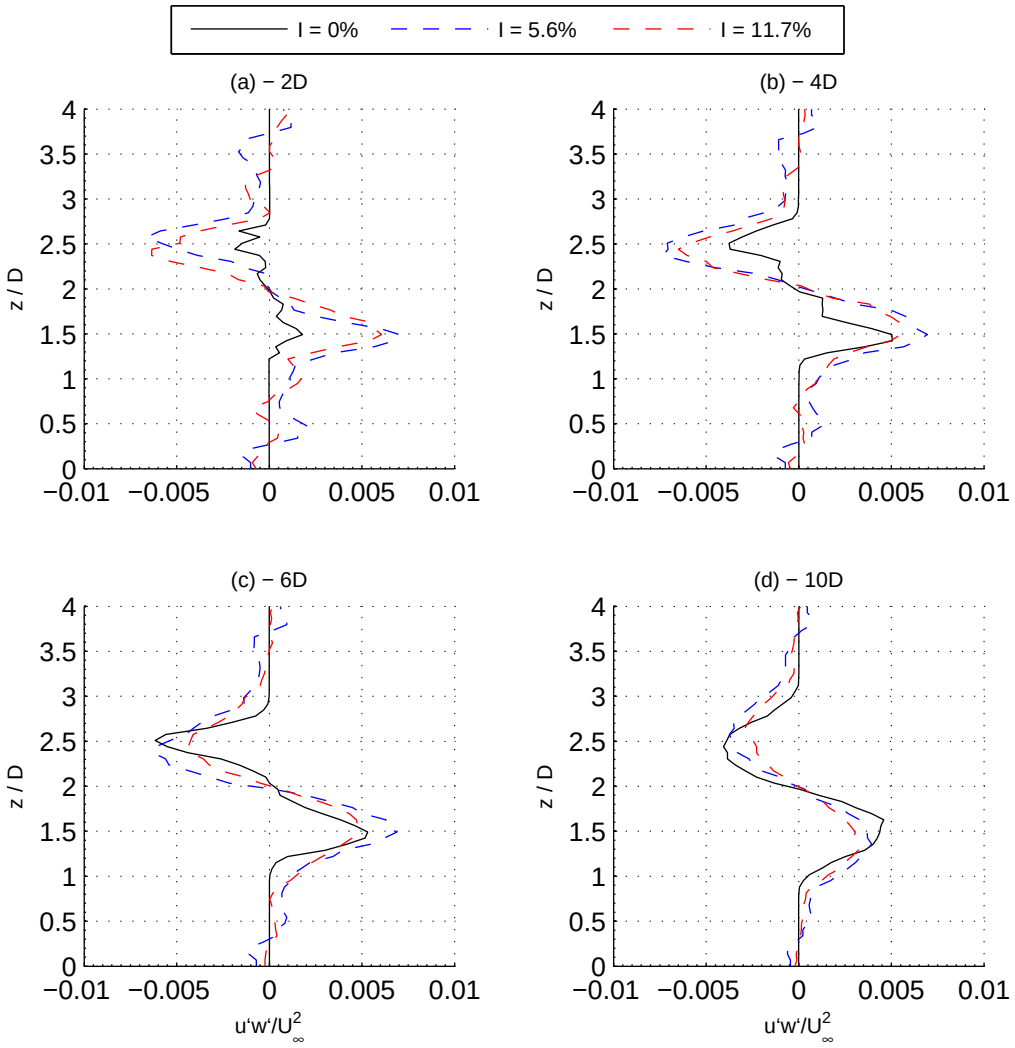

Figure 10.6: Velocity fluctuations ($u'w'$) at 2,4,6,10D downstream of an actuator disc with different turbulence intensity.

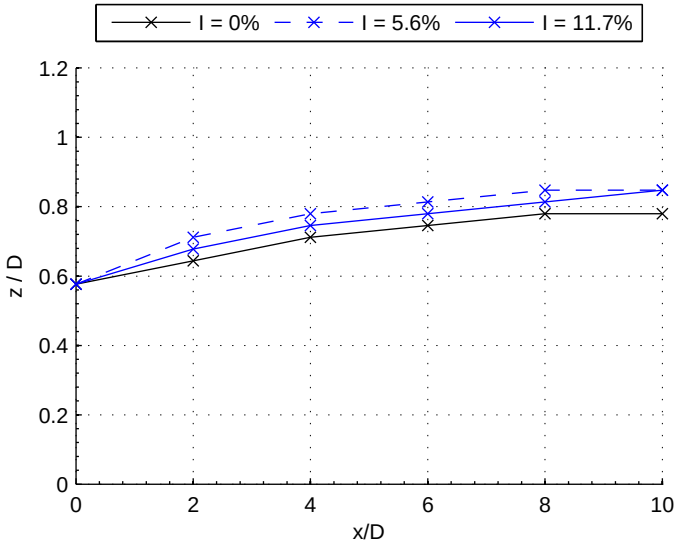

Figure 10.7: Wake edge defined by $U_w = 0.95U_\infty$, with increasing turbulence intensity.

10.3.3 Effects of integral length scale on wake profile, cases 1,2,4

It was shown earlier that increasing the integral length scale increased the maximum velocity deficit and shifted the point of maximum deficit closer to the disc. Figure 10.8 shows the vertical profiles of axial velocity at 2,4,6, and 10D downstream of the disc. It can be seen for case 1 with zero turbulence that the wake persists far downstream with minimal spreading. The wake recovery is faster with larger scale turbulence, at $2D$ $U_D = 0.7$ for case 4 and $U_D = 0.6$ for case 2 but further downstream the velocity deficit is lower for case 4 due to the faster wake recovery with larger length scales.

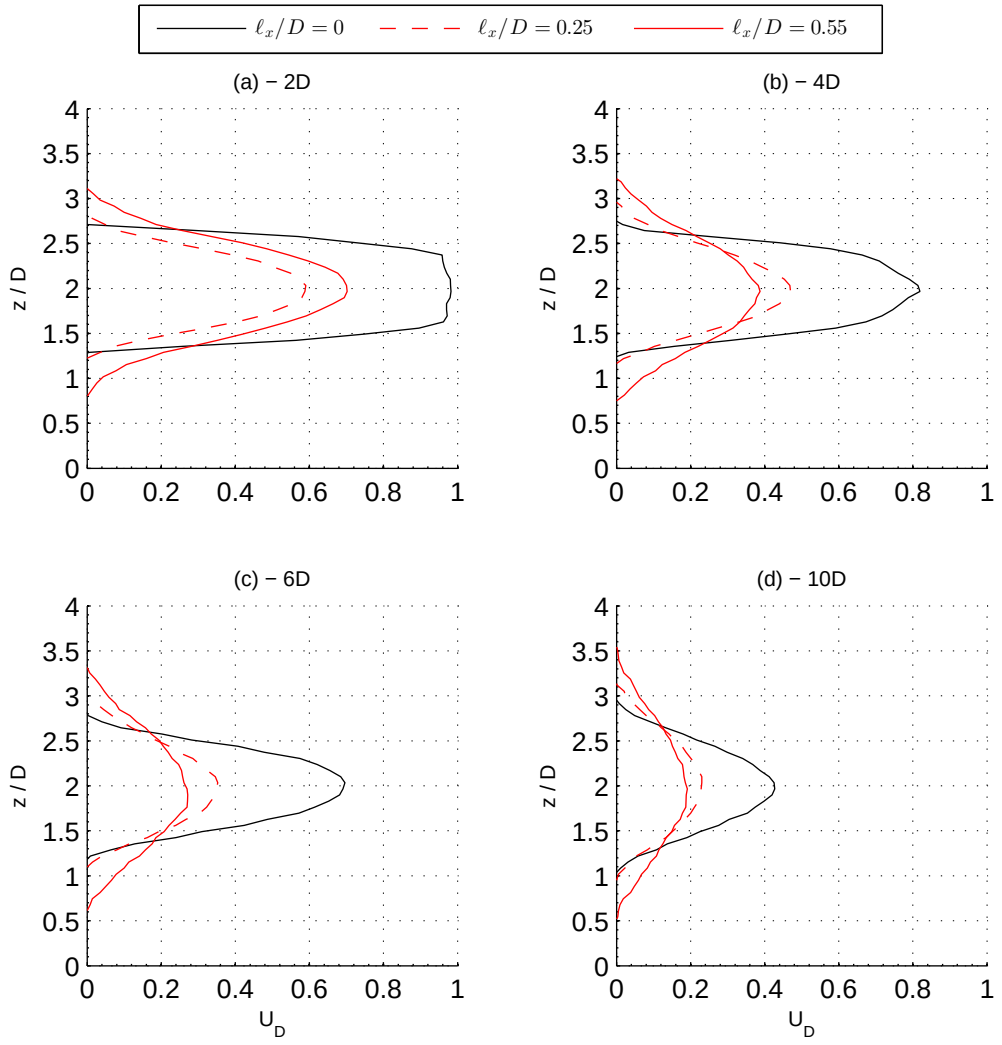

Figure 10.8: Velocity deficit at 2,4,6,10D downstream of an actuator disc with different integral length scales.

Considering the turbulence fluctuations it can be seen in figure 10.9 that the component $u'u'$ is greatest for case 4 with the larger integral length scales. By 10D the profile is almost uniform for case 4 whereas the wake profile is still visible for case 2 with small scale turbulence and still very pronounced for case 1 with zero turbulence. It

can also be seen that the profile of $u'u'$ spreads more rapidly for case 4 than the case with small scale or zero turbulence. Further, the increase in $u'u'$ is greater for larger scale turbulence, approximately four times the increase in $u'u'$ over ambient conditions, at 2D downstream, for case 4 with large scale turbulence over case 2 with small scale turbulence. Similar trends are seen in the profiles of $v'v'$ and $w'w'$ due to the isotropic structure of the turbulence. Refer to appendix C.3 for all 6 components of Reynolds stress. As $u'u'$ is equivalent to twice the axial component of turbulent kinetic energy this shows that a greater proportion of the flows energy, or momentum, is being converted to turbulence with larger length scales in the ambient flow. This explains why the velocity deficit is greater for flows with larger integral length scales as a greater proportion of the fluids momentum is being converted to turbulent energy.

Considering the cross component velocity fluctuation $u'v'$ and $v'w'$ are approximately zero as seen in appendix C.3. It can be seen in figure 10.10 that $u'w'$ for case 4 with large scale turbulence is over three times that of case 2 with small scale turbulence, while significantly larger than case 1 with zero turbulence. This shows that the rate of mixing of high momentum fluid from the ambient flow with the low momentum fluid in the wake is much higher with larger scale turbulence. Considering the edge of the wake as defined by $U_w = 0.95U_\infty$ or $U_D = 0.05$, it can be seen in figure 10.11 that larger length scales cause the wake to spread to a greater width than the case with smaller scale turbulence. This further demonstrates the increase in mixing between the low momentum wake and high momentum free stream flow with larger length scale turbulence.

Overall, it has been shown that larger scales of turbulence cause a greater increase in $u'u'$ and $u'w'$ across the disc and the initial velocity deficit is increased. This is due to the increased generation of turbulent energy further reducing the momentum of the fluid in the wake. However, due to the increase in $u'w'$, which is responsible for mixing the high momentum fluid of the ambient flow with the low momentum fluid of the wake, the wake width is increased and the wake recovery occurs at a faster rate with larger scales of turbulence. Therefore the velocity deficit is lower further downstream with larger scale turbulent flows.

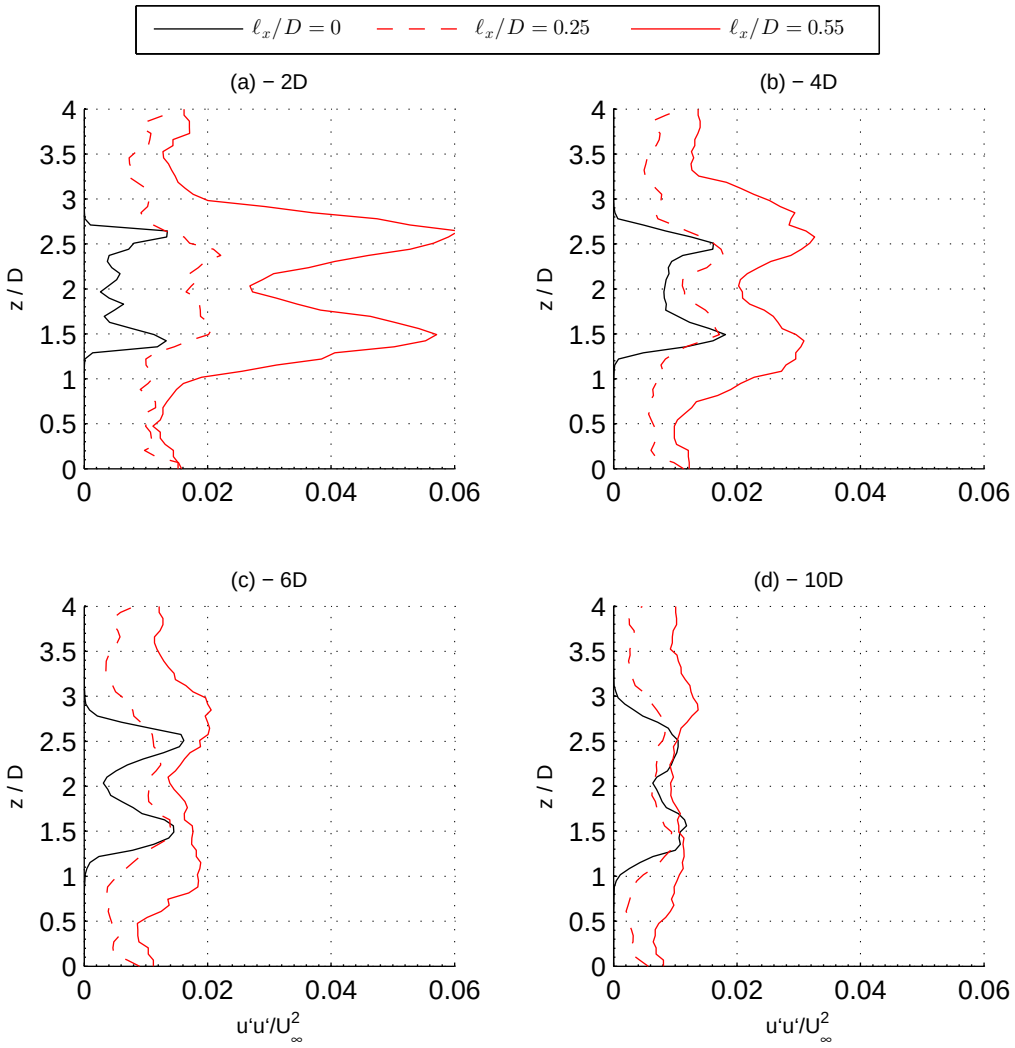

Figure 10.9: Velocity fluctuations ($u'u'$) at 2,4,6,10D downstream of an actuator disc with different integral length scales.

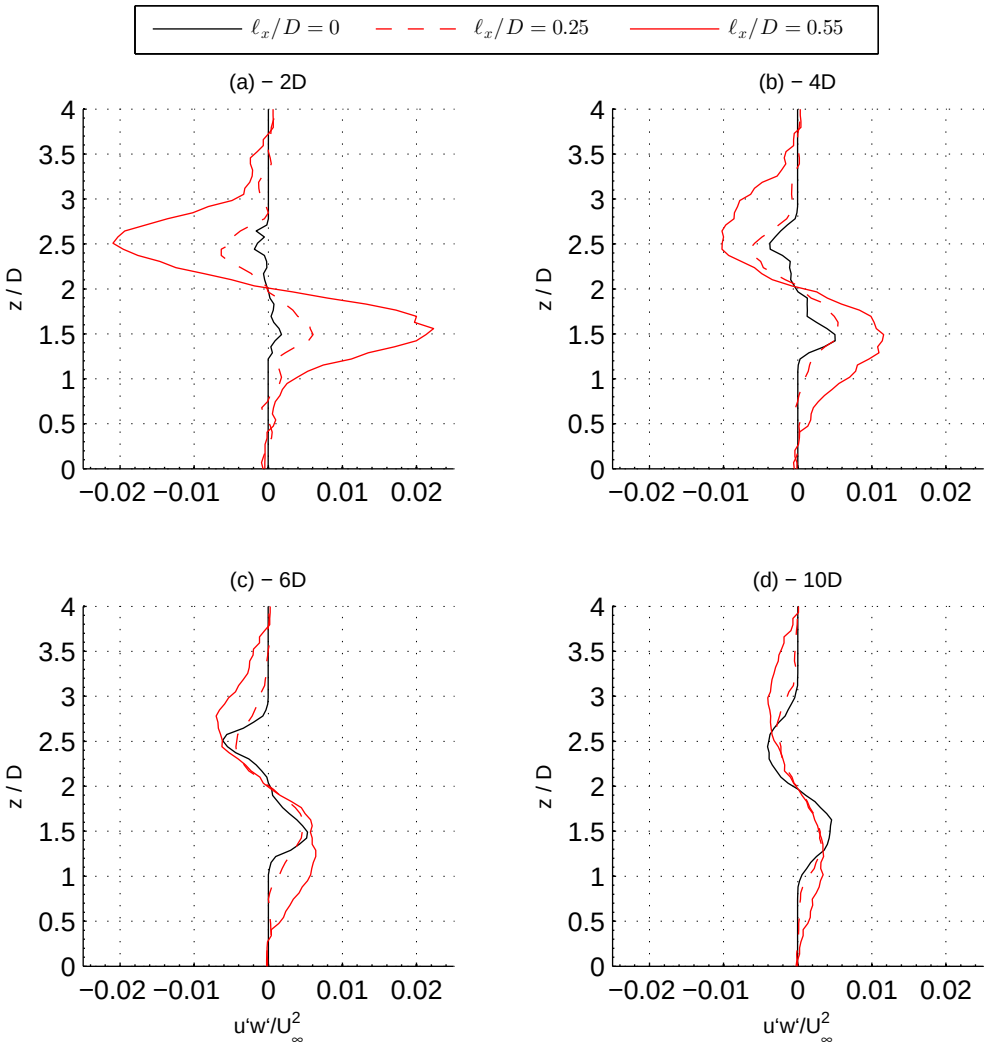

Figure 10.10: Velocity fluctuations ($u'w'$) at 2,4,6,10D downstream of an actuator disc with different integral length scales.

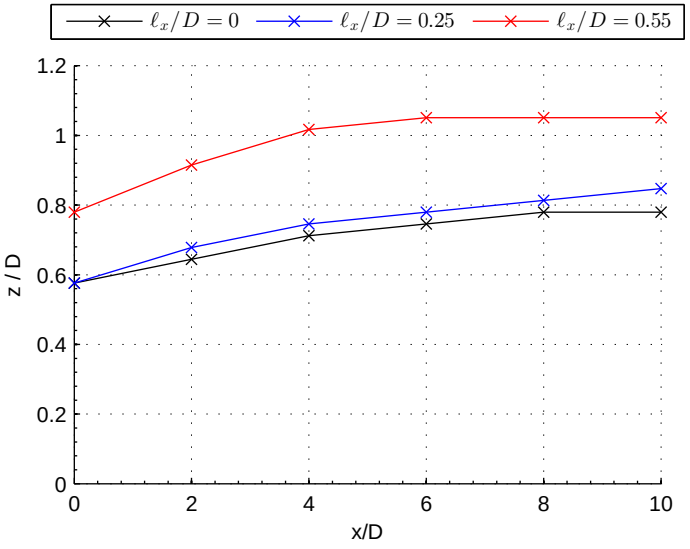

Figure 10.11: Wake edge defined by $U_w = 0.95U_\infty$, with increasing integral length scale.

10.4 Comparison with anisotropic turbulence

This section compares the results from the LES model with the experimental investigation to consider the effects of anisotropic turbulence. The final section of chapter 8 compares the ambient turbulence generated in the experimental investigation with the LES gridInlet. It was found that the turbulence in experiments was anisotropic whereas the LES model isotropic. The cause of the anisotropy in experiments was attributed to effects of upstream turbulence entering the grid, and effects of the bed boundary layer and the free-surface.

Table 10.2 compares the thrust coefficients of the five cases from the LES model with the experimental values of the 0.4 porosity disc from chapter 7 with the same turbulence intensities and integral length scales. For cases 2 and 3 with small scale turbulence ($\ell_x/D \approx 0.25$) the thrust coefficients recorded from the LES model agree well with the experimental data with an error of less than 3 %. For high turbulence intensity and larger scale turbulence, case 4 ($\ell_x/D = 0.55, I = 11.3$ %), the agreement was 7.28 % error compared to the experiments, but the agreement improved for case 5 to ≈ 3 % error, with lower intensity large scale turbulence for which $\ell_x/D = 0.88$.

Table 10.2: Thrust coefficients from 0.4 porous disc used in experiments with anisotropic turbulence and from the LES model with isotropic turbulence.

Case	Turbulence Intensity, I	Integral length scale ratio, ℓ_x/D	Thrust coefficient, C_T LES	Experiment	Percentage error
1	0	0	0.94	-	-
2	11.7	0.25	0.95	0.97	1.50
3	5.6	0.27	0.88	0.91	2.95
4	11.3	0.55	0.97	0.90	7.28
5	6.6	0.82	0.91	0.88	3.06

Comparison of the velocity profiles $3D$ downstream of the 0.4 porosity disc for ≈ 10 % turbulence intensity, cases 2 and 4, showed there are significant differences in the velocity deficit as shown in figure 10.12, although the general trends are the same. Note, the experimental data is plotted as a continuous profile due to the fine resolution of measurements (≈ 1 mm) made with a profiling ADV. It can be seen that the velocity deficit is between 0.7-0.9 for experiments and 0.5-0.6 for the LES model, although in both cases the velocity deficit is larger for the $M = 100$ mm grid than the $M = 300$ mm grid. The profiles of velocity fluctuations were considered to explain these differences in velocity profile. Figure 10.13 compares the velocity fluctuations in the axial direction $u'u'$, transverse direction $v'v'$, and vertical direction $w'w'$. The transverse and vertical components $v'v'$ and $w'w'$ are a measure of the rate of mixing between the free-stream flow and the wake. A flow with a larger $v'v'$ and $w'w'$ component would mix high momentum fluid from the free-stream with the low momentum wake more rapidly, and hence the wake would recover more quickly. It can be seen in figure 10.13(a) that the

axial and transverse components are much larger in experiments than in the LES model, approximately double. However, the component $w'w'$, figure 10.13(c), shows that the LES component is comparable to that of the experiments. This is due to the anisotropy measured in the ambient flow of the experiments as discussed in chapter 8. These differences in the turbulent fluctuations between the LES and experiments would explain why the velocity deficit is lower in the LES model due to the higher rate of mixing between the free-stream and the wake in the transverse direction relative to the axial direction causing the wake to recover more quickly. This further highlights the need to consider the site specific turbulence characteristics for accurate device modelling as the level of isotropy and $v'v'$ or $w'w'$ can also affect the wake profile behind a tidal turbine.

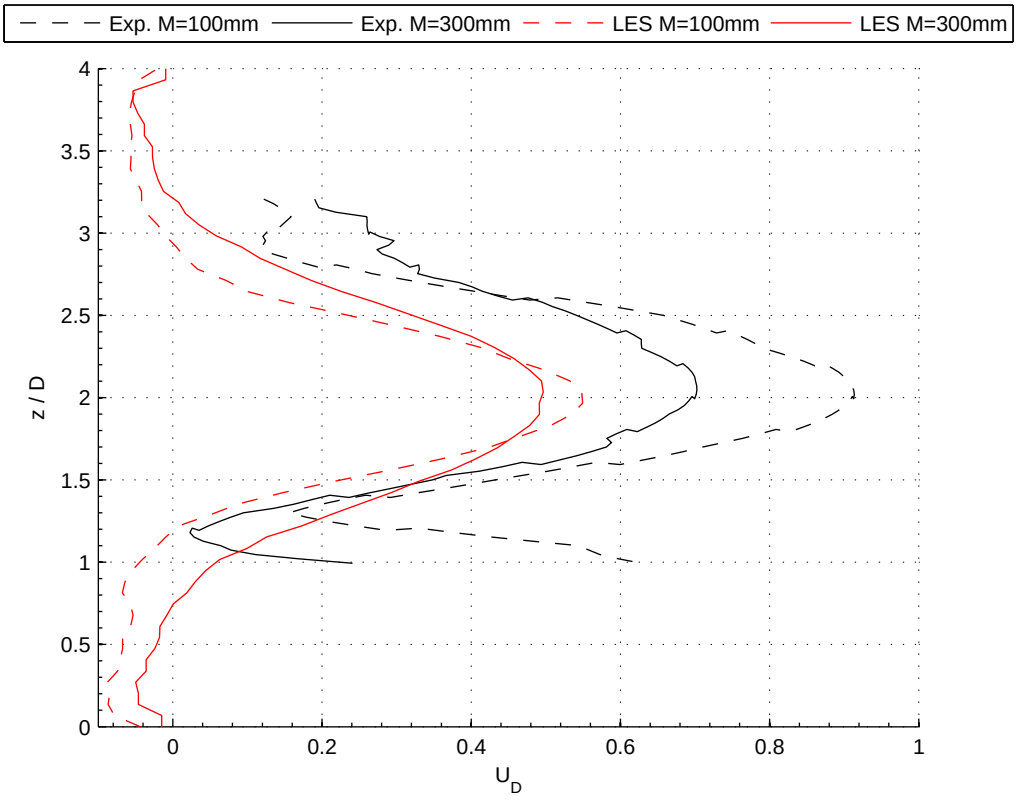

Figure 10.12: Comparison of velocity deficit from experiments and LES model $3D$ behind an actuator disc located $5x/D$ downstream of the grid.

Overall, the turbulence characteristics in the ambient flow of the anisotropic experiments and isotropic LES model show differences that explain the discrepancies in wake profile behind the actuator disc. This further highlights the sensitivity of turbine wakes to the turbulence characteristics of the flow and demonstrates that the level of isotropy of $v'v'$ and $w'w'$ is important. It is therefore crucial that the site specific turbulence characteristics are considered for the accurate modelling and optimisation of turbine array performance.

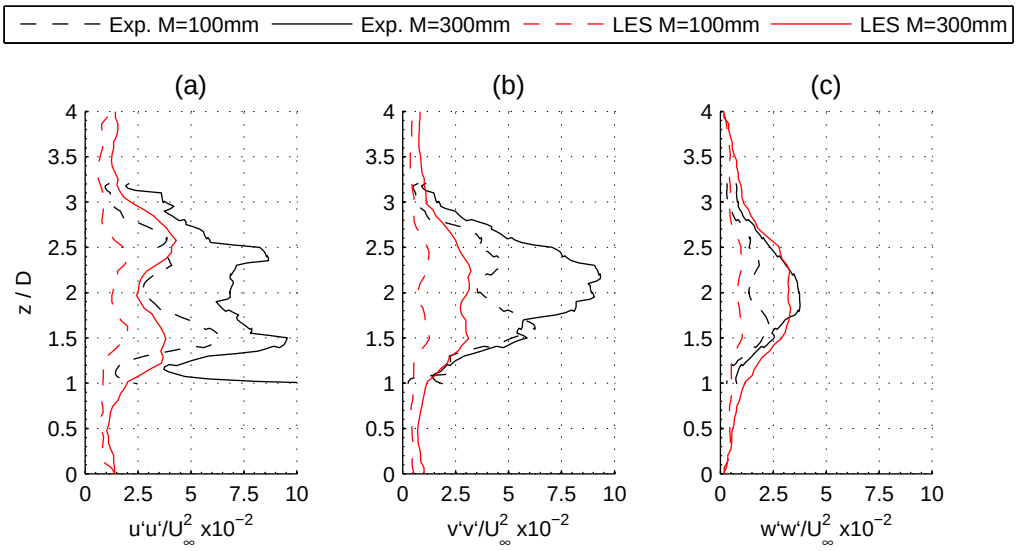

Figure 10.13: Comparison of velocity fluctuations from experiments and LES model $3D$ behind an actuator disc located $5x/D$ downstream of the grid.

10.5 Comparison with published data from experimental studies on turbine rotors and porous discs

Due to the limited wake data obtained in the experimental investigation comprehensive comparison of wake profiles was not possible. Comparisons have therefore been made with the published centreline velocity deficits from different studies using turbine rotors and porous discs. It can be seen in figure 10.14 that the results from cases 3 and 5 with turbulence intensities of approximately 5 % compare well with the published experimental data of Chamorro & Porté-Agel (2009), Mycek et al. (2013), Myers et al. (2013) from 3D downstream. Figure 10.15 shows comparisons of centreline velocity deficits with high levels of ambient turbulence intensity, cases 2 and 4, with $I \approx 10-15$ %. Good agreement is again seen with the published data demonstrating the significance of the ambient turbulence length scale on the wake profile, explaining some of the scatter in the published data. Larger deficits are seen in cases 4 with larger body scale turbulence in the near wake, less than 3D downstream. This suggests that body scale turbulence does have the greatest effect on the wake profile, but none of the experimental cases considered these scales. Further experimental investigation is required to confirm these trends on a turbine rotor.

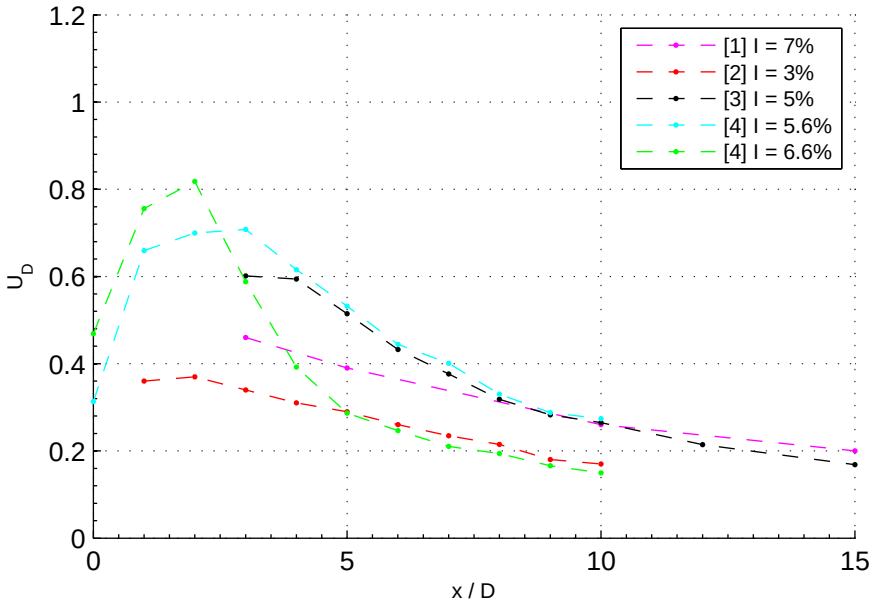

Figure 10.14: Comparison of centreline velocity deficit with published experimental data with $C_T \approx 0.9$ and low turbulence intensities of $I \approx 5$ %. [1]: Chamorro & Porté-Agel (2009) [2]: Mycek et al. (2013) [3]: Myers et al. (2013) [4]: present study (small scales blue, large scales green).

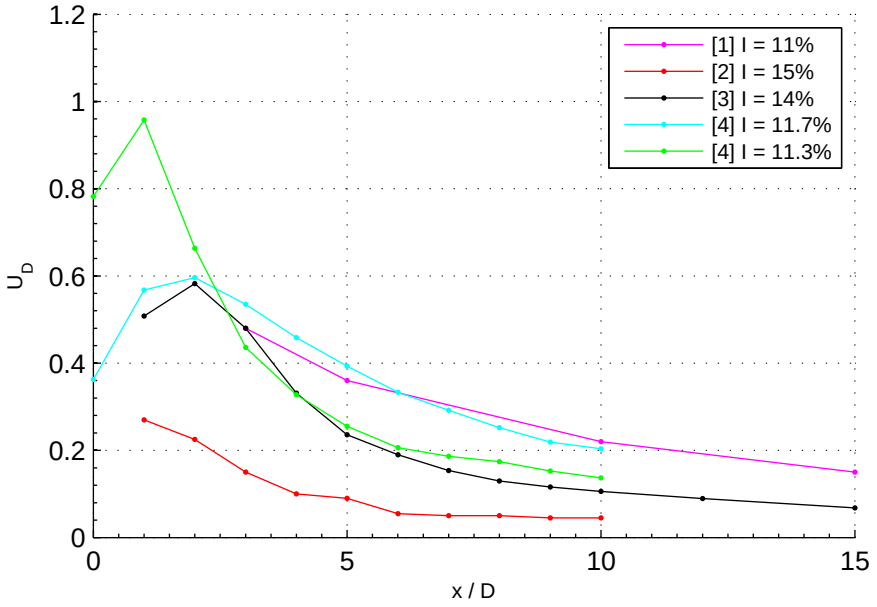

Figure 10.15: Comparison of centreline velocity deficit with published experimental data with $C_T \approx 0.9$ and high turbulence intensities of $I \approx 10 - 15$ %. [1]: Chamorro & Porté-Agel (2009) [2]: Mycek et al. (2013) [3]: Myers et al. (2013) [4]: present study (small scales blue, large scales green).

10.6 Summary and implications

The results demonstrate and explain the effects of turbulence intensity and integral length scale on the wake profile behind a gridded actuator disc. It was shown that the gridded actuator disc LES model produces results that compare well with published experimental data. The gridded actuator disc LES model provides information on the mean velocity field, but also provides information on the turbulent structure. In summary, the findings of this chapter are:

- Increasing the turbulence intensity of the ambient flow reduces the velocity deficit, shifts the location of maximum deficit closer to the disc, with an increases thrust. Turbulence intensity does not affect the wake width.
- Increasing the integral length scale increases the velocity deficit, shifts the location of maximum deficit closer to the disc, speeds up wake recovery, increases the wake width, with minimal increase in thrust.
- The turbulence intensity in the wake is a function of the actuator disc only and independent of the ambient turbulence characteristics.
- The integral length scale in the wake is affected by the actuator disc and turbulence intensity of the ambient flow. Increasing the turbulence intensity increases the integral length scale in the wake.
- Anisotropic turbulence further affects the wake profile due to differences in cross-component velocity fluctuations which further affect the rate of mixing between the wake and free-stream.

Chapter 11

Overall conclusions and engineering application

The demand for energy generated from renewable sources is ever increasing and energy from the tides provides a predictable and substantial resource. However, as the technology is still in its infancy further development is required to prove the robustness of current designs when operating in highly turbulent tidal flows. From reviewing the current literature it was found that tidal flows are highly turbulent and the characteristics site dependent, but the effects of such turbulent flows on the wake, thrust and power is unclear. Small scale laboratory experiments with porous disc rotor simulators are commonly used to represent the wake generated by a tidal turbine and actuator discs are often used to represent turbines in CFD models. However, the turbulence characteristics of the inflow to these simulations and experiments is often poorly reported and their effects little understood.

Initially a RANS model was used to investigate the sensitivity of actuator disc RANS simulations to characteristic length scale assumptions. It was found that the wake profile is sensitive to the assumed characteristic length scale, which had not previously been considered. Within RANS simulations the characteristic length scale controls the rate of turbulence dissipation, but the structure of the turbulent eddies are not resolved. Due to this limitation further work was required to understand the effect of turbulent eddy size, or integral length scale, on actuator discs.

An experimental investigation was performed to investigate the effects of grid generated turbulence on the thrust of porous discs. It was found that variations in thrust coefficient of over 20 % were possible with different turbulent conditions. Increasing turbulence intensity increased the thrust, which tended to a constant value for intensities greater than 13 %, while a strong dependence of the thrust on the integral length scale was found. Minimum thrusts were recorded for integral length scale to disc diameter ratios of 0.5.

New techniques were developed, based on the principle of grid generated turbulence, to generate inlet turbulence and turbulence within an actuator disc for LES models where the turbulent structure of the larger energy containing eddies is resolved. This model was used to investigate the effects of both ambient and device generated turbulence intensity and integral length scale on the wake of an actuator disc. Using these new techniques it was found that a device generating larger length scales and higher intensity turbulence results in a faster wake recovery. This is analogous to a turbine operating at low tip-speed ratios generating low frequency fluctuations, or turbulence. The ambient turbulence conditions were also found to significantly affect the wake where increasing turbulence intensity reduced the velocity deficit but did not affect the wake width. Increasing the integral length scale increased the velocity deficit but dramatically increased the wake width and recovery due to increased mixing between the wake and free stream. Finally, the effects of anisotropic turbulence were considered and found to affect the wake profile due to changes in the level of mixing between the wake and free stream.

11.1 Contributions to knowledge

The new contributions to knowledge from this study are summarised below:

- **Actuator disc RANS simulations are sensitive to characteristic length scale assumptions of the turbulence source.** This work demonstrated the significance of the characteristic length scale assumed for turbulence sources in actuator disc RANS models. It also raised the need to resolve the turbulent structures to further understand the interaction of eddy size on tidal turbines. It was shown that the velocity deficit in the wake was severely underestimated with no turbulence source while a small length scale overestimated the velocity deficit and delayed the wake recovery due to increased turbulence dissipation. A characteristic length scale equivalent to the porous disc hole diameter ($L_s = 5$ mm) showed the best agreement with experiments, although the turbulence intensity in the near wake was still underestimated suggesting a larger turbulence source term was required.

- **The thrust of porous discs are sensitive to the integral length scale, while increasing turbulence intensity increases thrust.** This study showed that the thrust forces acting on solid and porous discs are sensitive to the turbulence characteristics of the flow. Overall variations in thrust coefficient of 20 % were recorded and increasing turbulence intensity increased thrust; although the thrust coefficient tended to a constant value for intensities greater than 13 %. The effects of integral length scale showed a minimum thrust for length scale to disc diameter ratios of 0.5 which increased with intensity.

- **A new technique for generating isotropic turbulence in LES models has been developed.** The developed gridInlet technique can be used to generate isotropic turbulence with intensities up to 20 % with integral length scales of approximately half the grid size and dependent on Reynolds number. A cell density of 32×32 cells per grid size M should provide sufficient resolution and a triple inlet grid period was found to be the minimum to avoid constraining the growth of turbulent eddies.

- **A new technique for generating turbulence in actuator disc LES models has been developed.** The developed gridded actuator disc was shown to generate turbulence in LES models where the turbulence characteristics in the wake may be controlled by the grid parameters. It was also shown that a device generating higher turbulence intensity and larger integral length scales, analogous to a turbine operating at low tip-speed ratios, results in a faster wake recovery.

- **Increasing turbulence intensity reduces the velocity deficit, while increasing the integral length scale increases the velocity deficit in the near wake but results in lower velocity deficits in the far wake through increased mixing with the free stream flow.** This study showed that increasing the turbulence intensity of the ambient flow reduces the velocity deficit, and shifts the location of maximum deficit closer to the disc with an increase in thrust. Increasing the integral length scale increases the velocity deficit, shifts the location of maximum deficit closer to the disc, speeds up wake recovery, increases the wake width, with a small increase in thrust.

11.2 Engineering application - what do these results mean for the tidal energy industry?

It has been shown that both the integral length scale and turbulence intensity significantly affect the wake profile and thrust loads on an actuator disc. Many of the wake models used to predict the performance and device spacing of tidal arrays (both analytical models and RANS models) do not consider the effects of integral length scale of the turbulent flow. This could result in arrays being designed with devices spaced further apart and the power output of the array would be sub-optimal. By considering the turbulence characteristics of the ambient flow, including the integral length scale and intensity, tidal arrays may be optimised to the site specific turbulence conditions.

It was also shown that the turbulence characteristics in the wake are directly related to the device generated turbulence. Therefore if a tidal turbine was designed to produce larger length scales of turbulence (potentially by operating at a lower tip-speed ratio) its wake recovery would be faster. The turbine spacing in an array would therefore be

reduced and more turbines installed per unit area, increasing the power output of the array. This work therefore demonstrates the need to consider both turbulence intensity and integral length scale in the design and optimisation of both single turbines and arrays. Further, the specific characteristics of turbulence at each site must be considered as differences in isotropy were also shown to affect the wake recovery due to changes in mixing with the high momentum fluid in the free stream flow. By considering the turbulence characteristics in the flow at a tidal site the power output of the array may be increased due to optimised turbine spacing. Finally, the developed gridded actuator disc technique may be used to model tidal turbines in LES models of tidal sites as commonly performed with RANS models but provide an extra level of detail by resolving the turbulent structures.

11.2.1 Recommendations

For the optimisation and accurate modelling of tidal turbine wakes, thrust loads, and power outputs, the specific turbulence characteristics of the ambient flow must be considered. While simpler RANS or analytical models may give a good first approximation to wake profiles and performance of a turbine or array, it is necessary to consider the specific turbulence characteristics as high intensity flows with large length scales will result in faster wake recovery and larger loads than lower intensity flows with smaller length scales. Arrays may therefore be sub-optimal due to devices being spaced further apart with performance estimates being up to 20 % out[1] - this could be the difference between the economic success or failure of a tidal array.

By considering a single turbine it may be possible to optimise the characteristics of its generated turbulence to maximise its performance in an array. Turbines generating larger length scales and higher intensity turbulence may be placed closer together within an array, further increasing the number or devices per unit area and increasing the power output of the array.

The developed gridInlet and gridded actuator disc may be used to represent turbines in LES models. By further changing the pattern of patches on the gridInlet different profiles and turbulence characteristics may be generated. This method accounts for the turbulent structure of the flow providing an improved prediction over current RANS models.

[1] See section 7.4.3, figure 7.12

11.3 Further work

This study has shown how the turbulence characteristics of the flow affect the wake and thrust of an actuator disc. However, it has also raised more questions that should be considered to further understand the influence of turbulence on a turbine.

Grid generated turbulence was used for this study to simplify the problem and allow the specific effects of integral length scale and intensity to be investigated. However, the effects of anisotropic turbulence were briefly considered and found to further effect the wake due to changes in wake mixing. Further studies are therefore required to assess the effects of anisotropic turbulence as experienced in a tidal flow and also the effects of a boundary layer. The gridInlet technique may be further developed using different patterns on the inlet to develop turbulence with different characteristics and profiles, for example horizontal bars may be applied with varying thickness, instead of a grid, to generate a velocity profile and associated turbulence profile. This would be akin to methods used in wind tunnels to develop simulated atmospheric boundary layers.

Finally, experimental investigations are required with rotating model turbines to confirm the results obtained using actuator discs and porous disc rotor simulators. Full scale measurements from tidal sites would allow further validation of these models and provide a greater understanding of what the turbulence characteristics are at different tidal sites.

Appendices

Appendix A

Integration and Discretisation

A.1 Integration

Details of integration and discretisation procedures for the finite volume method. For further reading refer to Versteeg & Malalasekera (1995)

Integration is performed over each control volume (cell) in the domain. Gauss' divergence theorem is used to convert volume integrals of divergence and gradient operators to surface integrals. The theorem states,

$$\int_V \frac{\partial u}{\partial x} dV = \int_A e.u \; dA \tag{A.1}$$

where $\int_V$ is a volume integral, $\int_A$ is a surface integral, and e is a unit vector normal to surface dA. Thus the volume integral of the divergence of u is equal to the component of u normal to the surface which bounds the volume, summed over the entire bounding surface A (Versteeg & Malalasekera 1995).

A.2 Discretisation

For a function $f(x)$, the value $f(x + \Delta x)$ may be evaluated using a Taylor series,

$$f(x + \Delta x) = f(x) + \left(\frac{\partial f(x)}{\partial x}\right) \Delta x + \left(\frac{\partial^2 f(x)}{\partial x^2}\right) \frac{\Delta x^2}{2} + \ldots \tag{A.2}$$

Rearranging yields an expression for $\partial f(x)/\partial x$,

$$\frac{\partial f(x)}{\partial x} = \frac{f(x + \Delta x) - f(x)}{\Delta x} - \left(\frac{\partial^2 f(x)}{\partial x^2}\right) \frac{\Delta x}{2} - \ldots \tag{A.3}$$

Neglecting the higher order terms that involve a multiplying factor Δx,

$$\frac{\partial f(x)}{\partial x} \approx \frac{f(x+\Delta x) - f(x)}{\Delta x}. \tag{A.4}$$

This is a forward difference as $\partial f(x)/\partial x$ is evaluated using $f(x)$ and $f(x+\Delta x)$. The error is proportional to Δx so reducing the cell size reduces the error, this is a first order approximation.

Similarly, $\partial f(x)/\partial x$ may be evaluated using $f(x)$ and $f(x-\Delta x)$,

$$f(x-\Delta x) = f(x) - \left(\frac{\partial fx}{\partial x}\right)\Delta x + \left(\frac{\partial^2 f(x)}{\partial x^2}\right)\frac{\Delta x^2}{2} + \dots \tag{A.5}$$

Rearranging yields a backward difference approximation,

$$\frac{\partial f(x)}{\partial x} \approx \frac{f(x) - f(x-\Delta x)}{\Delta x}. \tag{A.6}$$

As before this is first order accurate and $\partial f(x)/\partial x$ is evaluated using only one other point. Subtracting equation A.6 from equation A.2 yields,

$$f(x+\Delta x) - f(x-\Delta x) = 2\left(\frac{\partial fx}{\partial x}\right)\Delta x + \left(\frac{\partial^3 f(x)}{\partial x^3}\right)\frac{\Delta x^3}{3!} + \dots \tag{A.7}$$

Rearranging, a third expression for $\partial f(x)/\partial x$ may be found,

$$\frac{\partial f(x)}{\partial x} = \frac{f(x+\Delta x) - f(x-\Delta x)}{2\Delta x} + \left(\frac{\partial^3 f(x)}{\partial x^3}\right)\frac{\Delta x^2}{3!} + \dots \tag{A.8}$$

Here, $\partial f(x)/\partial x$ is evaluated using two neighboring points and is known as a central differencing approximation. The error is proportional to Δx^2 and is therefore a second order method.

Appendix B

Porous disc dimensions

Details of the porous disc hole patterns are shown in table B.1. Figure B.1 shows a photo of disc 4 attached to the mounting beam and figure B.2 shows the load rig with key dimensions.

Table B.1: Porous disc hole patterns.

	Number of 6 mm holes on pitch circle diameter			
	$\theta = 0.4$		$\theta = 0.6$	
Pitch circle diameter	disc 6 $D = 108$ mm	disc 3 $D = 150$ mm	disc 7 $D = 108$ mm	disc 4 $D = 150$ mm
17	6	6	7	7
31	10	10	14	14
45	14	14	21	21
59	18	18	28	28
73	23	23	35	35
87	27	27	41	41
101	31	31	47	47
115	-	36	-	54
129	-	40	-	61
143	-	44	-	67

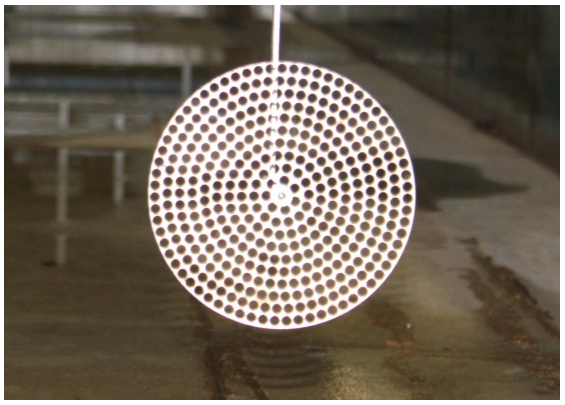

Figure B.1: Photograph of disc 4; 0.6 porosity, 150 mm diameter, porous disc rotor simulator.

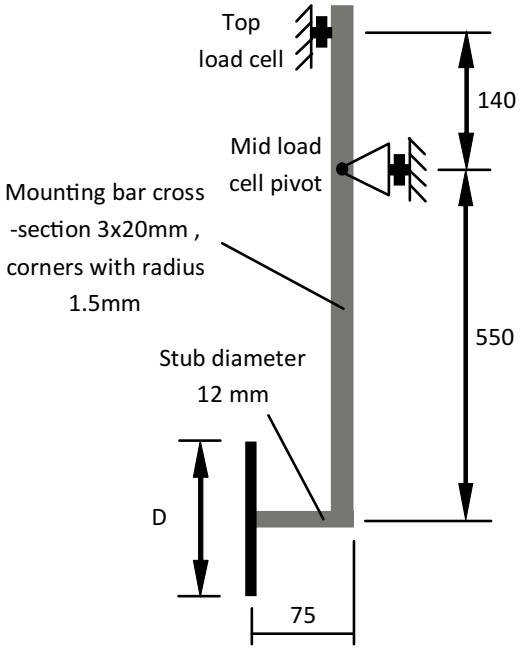

Figure B.2: Details of the load rig and dimensions of the mounting beam.

Appendix C

Reynolds stresses

C.1 Reynolds stresses of ambient flow

The 6 components of Reynolds stress from experiments and LES model.

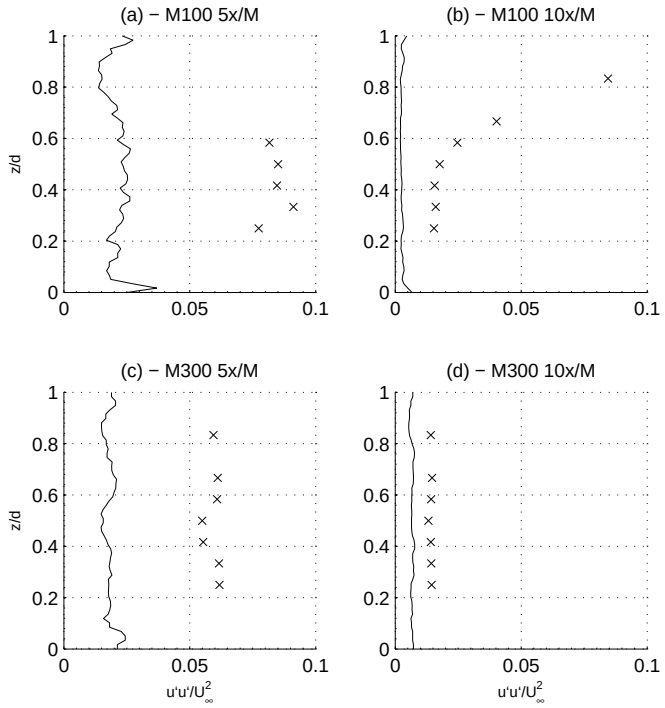

Figure C.1: Profiles of $u'u'$ behind LES gridInlet and experiments for $M = 100$ mm and $M = 300$ mm.

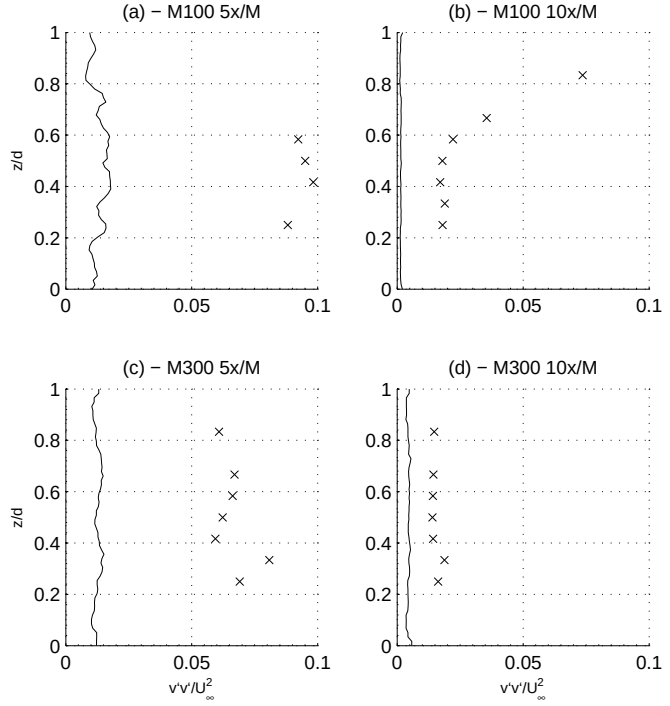

Figure C.2: Profiles of $v'v'$ behind LES gridInlet and experiments for $M =$ 100 mm and $M = 300$ mm.

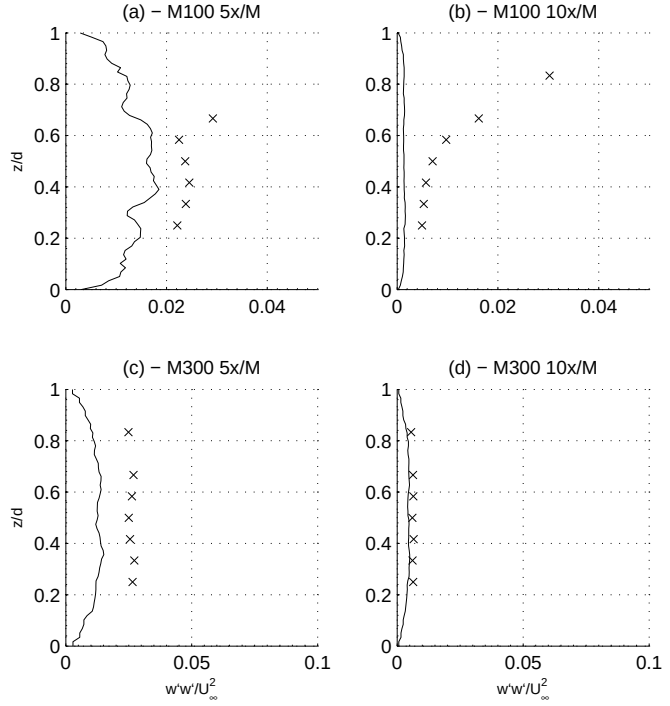

Figure C.3: Profiles of $w'w'$ behind LES gridInlet and experiments for $M =$ 100 mm and $M = 300$ mm.

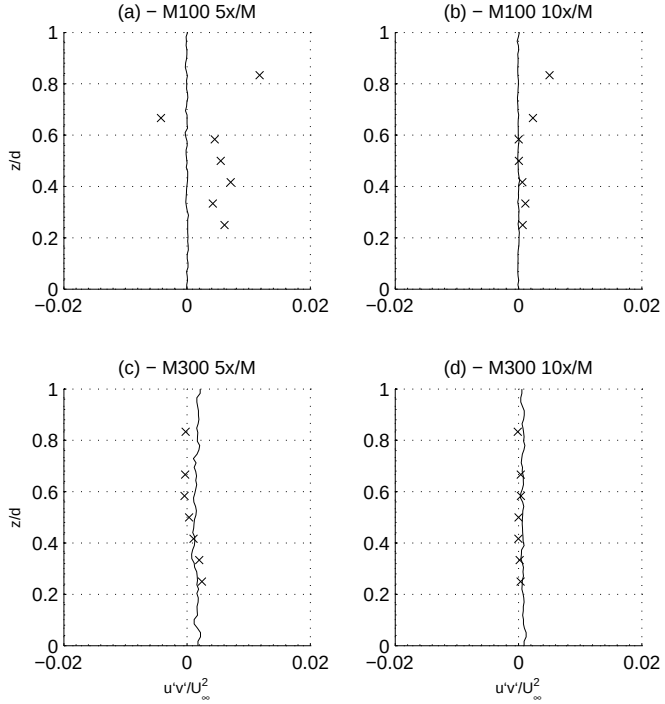

Figure C.4: Profiles of $u'v'$ behind LES gridInlet and experiments for $M = 100$ mm and $M = 300$ mm.

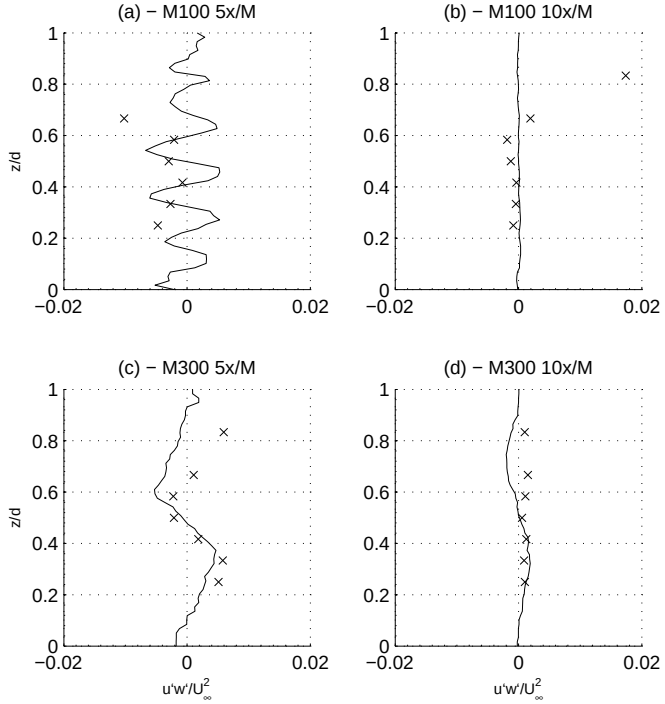

Figure C.5: Profiles of $u'w'$ behind LES gridInlet and experiments for $M = 100$ mm and $M = 300$ mm.

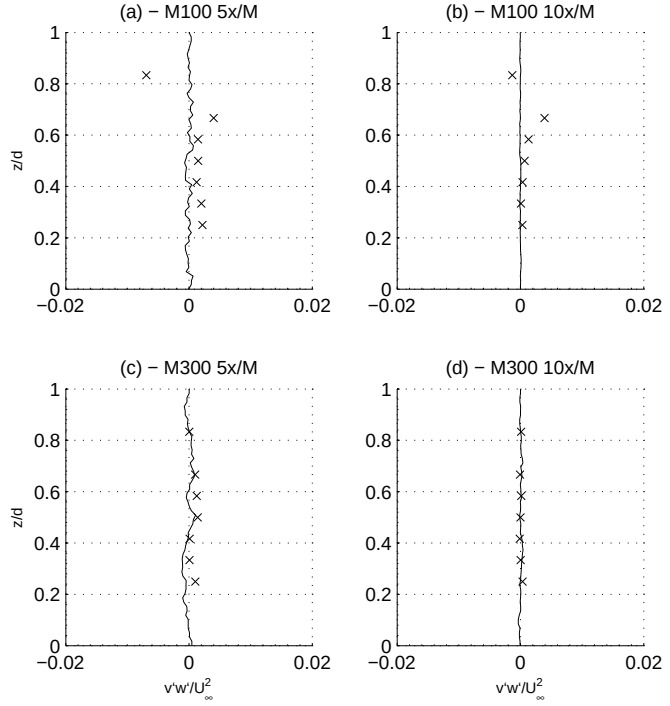

Figure C.6: Profiles of $v'w'$ behind LES gridInlet and experiments for $M = 100$ mm and $M = 300$ mm.

C.2 Reynolds stresses behind actuator disc with different turbulence intensity

The 6 components of Reynolds stress with zero, low intensity and high intensity turbulence.

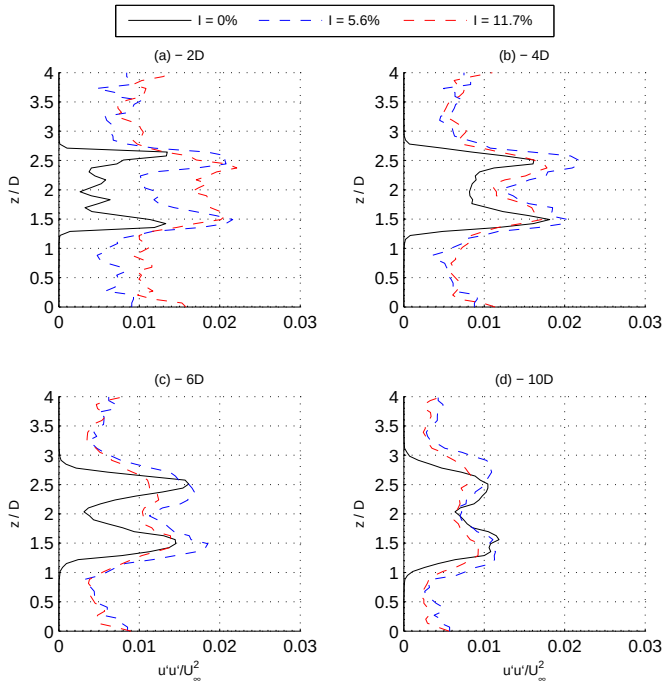

Figure C.7: Velocity fluctuations ($u'u'$) at 2,4,6,10D downstream of an actuator disc with different turbulence intensity.

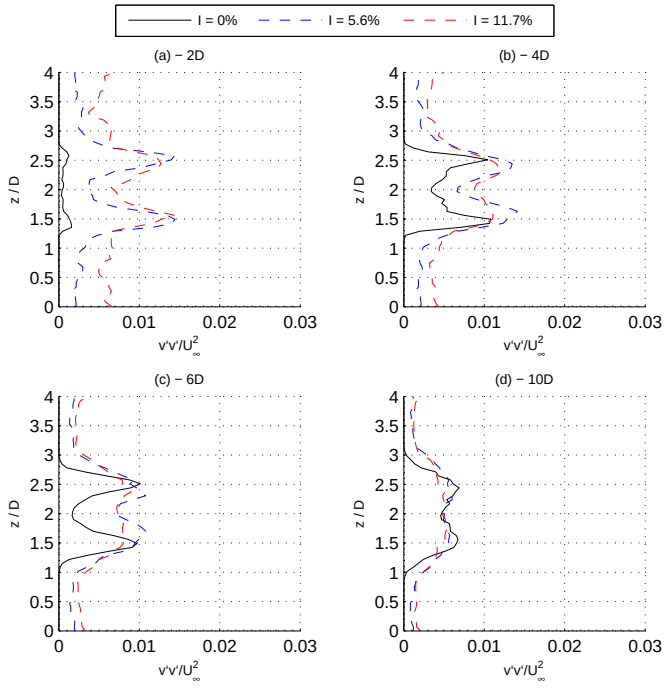

Figure C.8: Velocity fluctuations ($v'v'$) at 2,4,6,10D downstream of an actuator disc with different turbulence intensity.

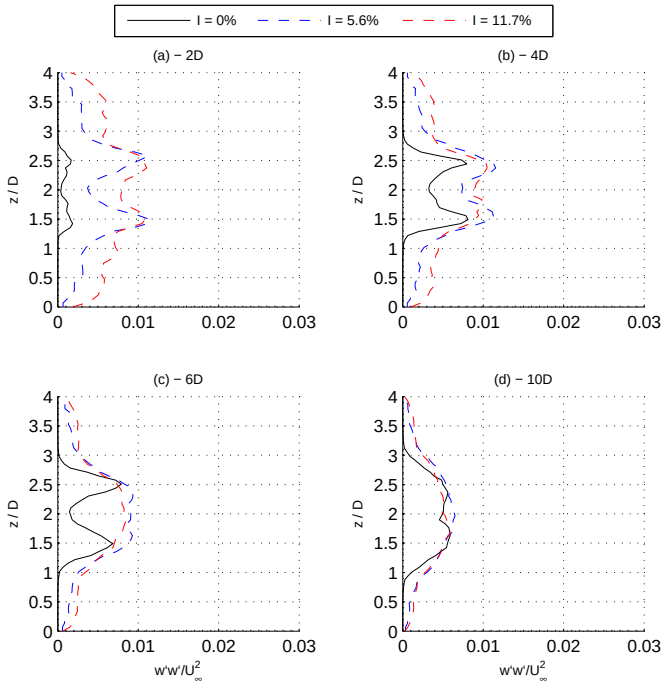

Figure C.9: Velocity fluctuations ($w'w'$) at 2,4,6,10D downstream of an actuator disc with different turbulence intensity.

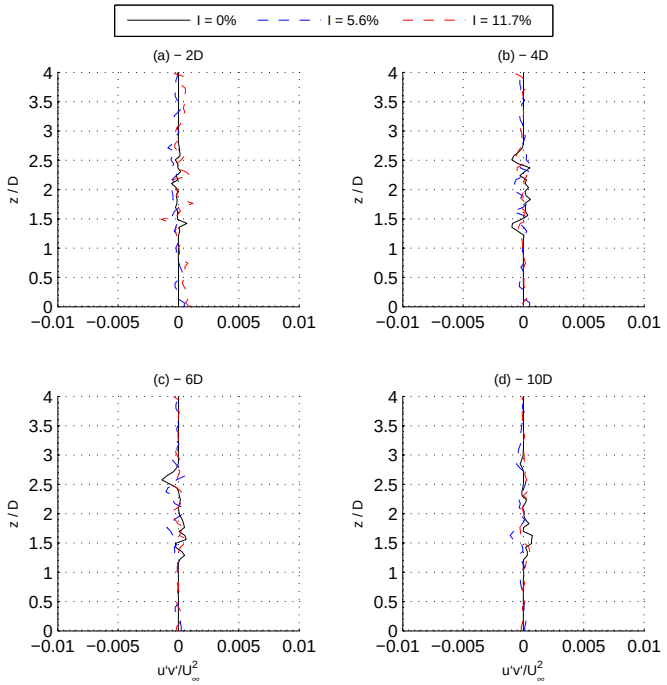

Figure C.10: Velocity fluctuations ($u'v'$) at 2,4,6,10D downstream of an actuator disc with different turbulence intensity.

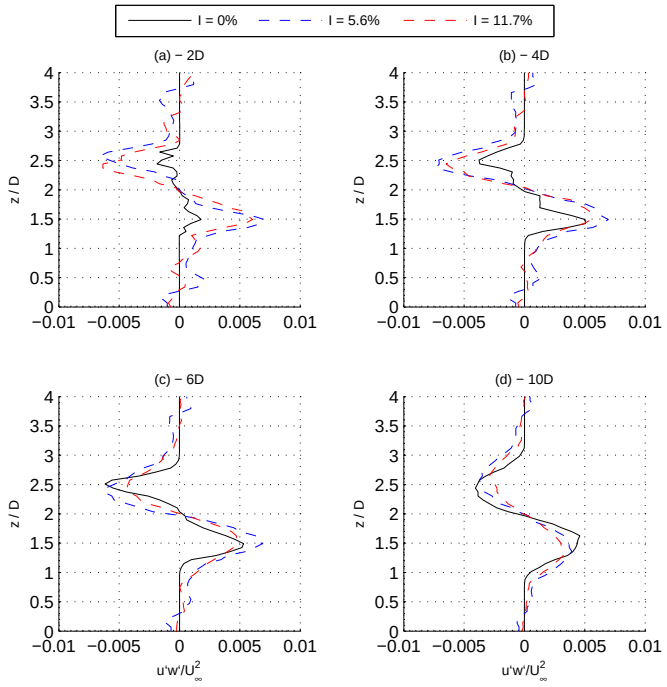

Figure C.11: Velocity fluctuations ($u'w'$) at 2,4,6,10D downstream of an actuator disc with different turbulence intensity.

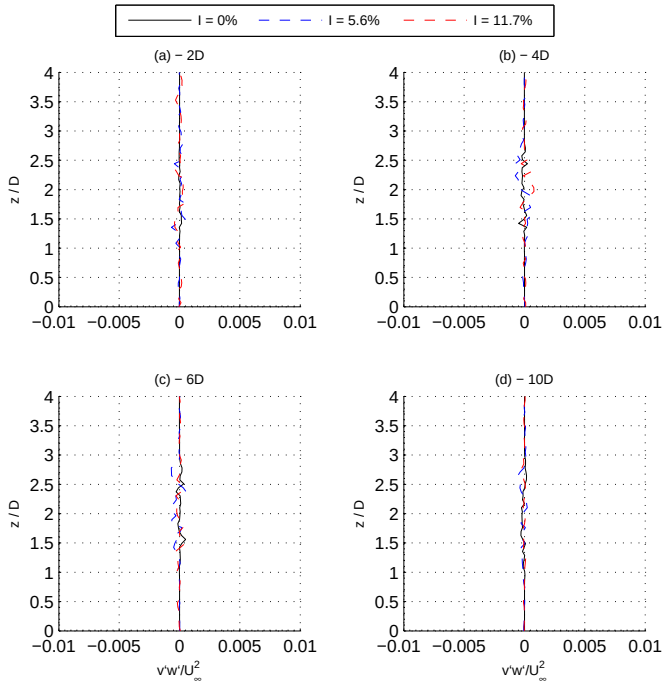

Figure C.12: Velocity fluctuations ($v'w'$) at 2,4,6,10D downstream of an actuator disc with different turbulence intensity.

C.3 Reynolds stresses behind actuator disc with different integral length scale

The 6 components of Reynolds stress for the cases with zero turbulence, small scales and large scale turbulence.

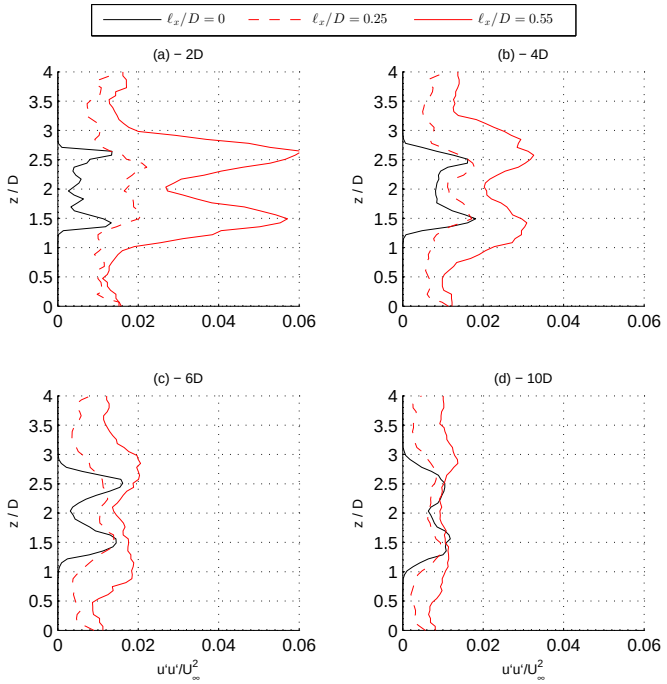

Figure C.13: Velocity fluctuations ($u'u'$) at 2,4,6,10D downstream of an actuator disc with different integral length scales.

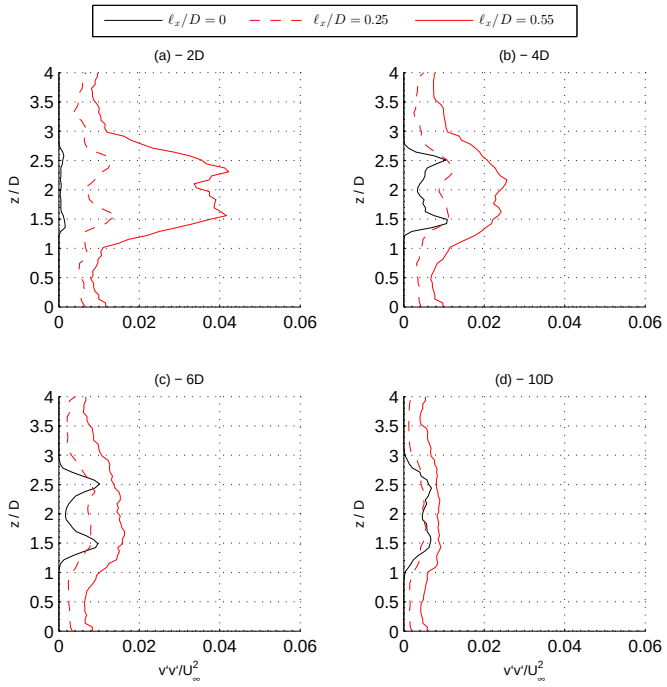

Figure C.14: Velocity fluctuations ($v'v'$) at 2,4,6,10D downstream of an actuator disc with different integral length scales.

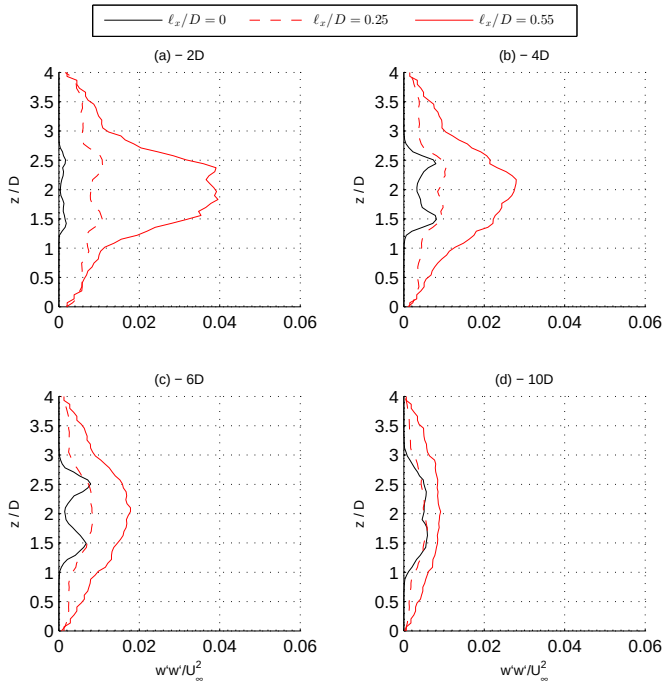

Figure C.15: Velocity fluctuations ($w'w'$) at 2,4,6,10D downstream of an actuator disc with different integral length scales.

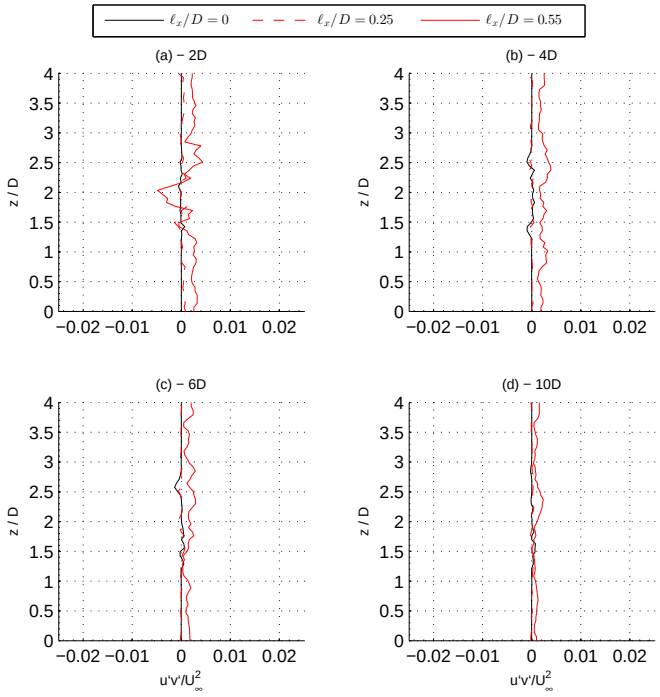

Figure C.16: Velocity fluctuations ($u'v'$) at 2,4,6,10D downstream of an actuator disc with different integral length scales.

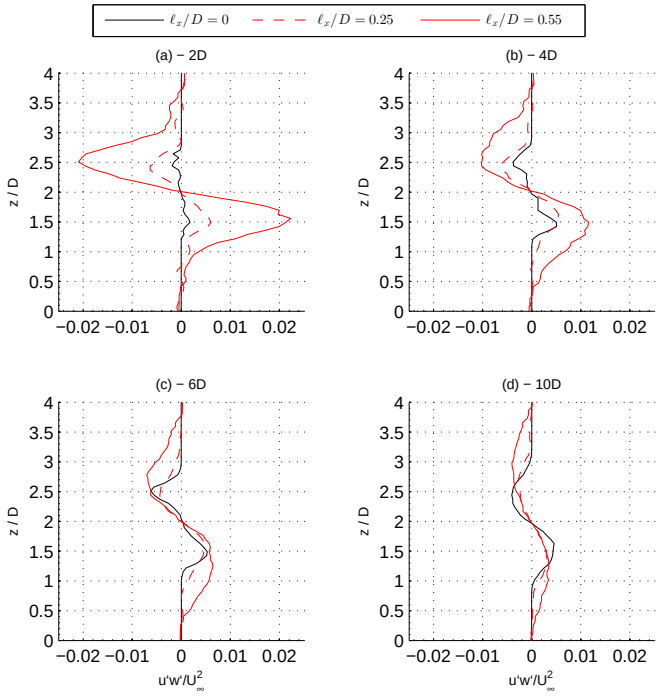

Figure C.17: Velocity fluctuations ($u'w'$) at 2,4,6,10D downstream of an actuator disc with different integral length scales.

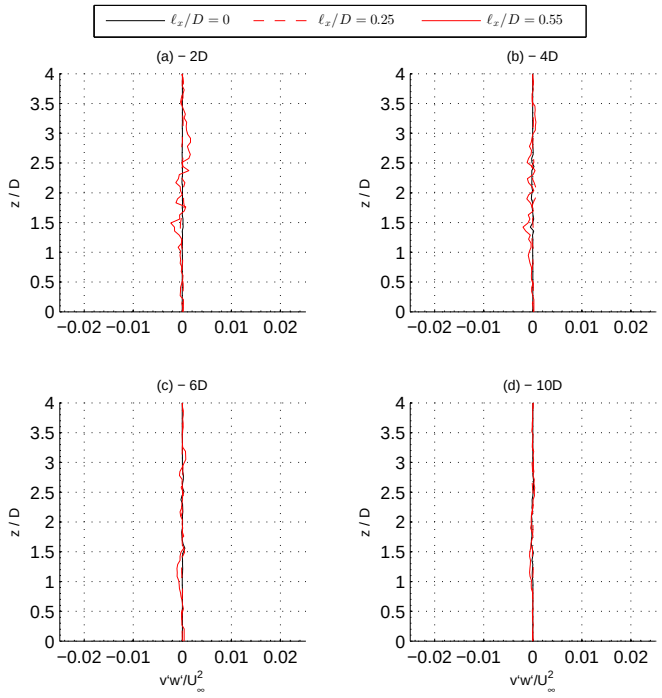

Figure C.18: Velocity fluctuations ($v'w'$) at 2,4,6,10D downstream of an actuator disc with different integral length scales.

References

Ainslie, J. (1986), Wake modelling and the prediction of turbulence properties, *in* 'Proc. 8th BWEA Wind Energy Conf.', Cambridge.

Bahaj, A. S. (2011), 'Generating electricity from the oceans', *Renewable and Sustainable Energy Reviews* **15**(7), 3399–3416.

Bahaj, A. S. (2013), 'Marine current energy conversion: the dawn of a new era in electricity production', *Phil Trans R Soc A* **371**(1985).

Bahaj, A. S. & Myers, L. E. (2003), 'Fundamentals applicable to the utilisation of marine current turbines for energy production', *Renewable Energy* **28**(14), 2205–2211.

Batten, W. M. J., Harrison, M. E. & Bahaj, A. S. (2013), 'Accuracy of the actuator disc-RANS approach for predicting the performance and wake of tidal turbines.', *Phil Trans R Soc A* **371**(1985).

Bearman, P. W. & Morel, T. (1983), 'Effect of free stream turbulence on the flow around bluff bodies', *Progress in Aerospace Sciences* **20**(2-3), 97–123.

Black and Veatch (2005), UK Tidal Stream Energy Resource Assessment, Technical Report 0, Carbon Trust.

Blackmore, T., Batten, W. M. J. & Bahaj, A. S. (2013*a*), 'Inlet grid-generated turbulence for large-eddy simulations', *International Journal of Computational Fluid Dynamics* **27**(6-7), 307–315.

Blackmore, T., Batten, W. M. J. & Bahaj, A. S. (2013*b*), Turbulence generation and its effect in LES approximations of tidal turbines, *in* '10th European Wave and Tidal Energy Conference', Aalborg, Denmark.

Blackmore, T., Batten, W. M. J., Harrison, M. E. & Bahaj, A. S. (2011), The Sensitivity of Actuator-Disc RANS Simulations to Turbulence Length Scale Assumptions, *in* '9th European Wave and Tidal Energy Conference', Southampton.

Blackmore, T., Batten, W. M. J., Műller, G. U. & Bahaj, A. S. (2013), 'Influence of turbulence on the drag of solid discs and turbine simulators in a water current', *Experiments in Fluids* **55**(1), 1637.

Bowden, K. F. (1962), 'Measurements of Turbulence near the sea bed in a tidal current', *Journal of Geophysical Research* **67**(8).

Bowden, K. & Fairbairn, L. (1956), 'Measurements of turbulent fluctuations and Reynolds stresses in a tidal current', *Proceedings of the Royal Society of London.* **237**(1210), 422–438.

Bowden, K. & Howe, M. (1963), 'Observations of turbulence in a tidal current', *Journal of Fluid Mechanics* **17**(2), 271–284.

Burton, T., Sharpe, D., Jenkins, N. & Bossanyi, E. (2001), *Wind Energy Handbook: Aerodynamics of Horizontal-Axis Wind Turbines*, Vol. 2, 2nd edn, John Wiley & Sons, Chichester, UK.

Carati, D., Ghosal, S. & Moin, P. (1995), 'On the representation of backscatter in dynamic localization models', *Physics of Fluids* **7**(3), 606.

Castellani, F. & Vignaroli, A. (2012), 'An application of the actuator disc model for wind turbine wakes calculations', *Applied Energy* .

Cea, L., Puertas, J. & Pena, L. (2007), 'Velocity measurements on highly turbulent free surface flow using ADV', *Experiments in Fluids* **42**(3), 333–348.

Chamorro, L. P. & Porté-Agel, F. (2009), 'A Wind-Tunnel Investigation of Wind-Turbine Wakes: Boundary-Layer Turbulence Effects', *Boundary-Layer Meteorology* **132**(1), 129–149.

Chumakov, S. G. & Rutland, C. J. (2005), 'Dynamic structure subgrid-scale models for large eddy simulation', *Int. J. Numer. Meth. Fluids* **47**(December 2004), 911–923.

Chung, Y. M. & Sung, H. J. (1997), 'Comparative Study of Inflow Conditions for Spatially Evolving Simulation', *AIAA Journal* **35**(2), 269–274.

Churchfield, M. J., Li, Y. & Moriarty, P. J. (2013), 'A large-eddy simulation study of wake propagation and power production in an array of tidal-current turbines.', *Phil Trans R Soc A* **371**(1985).

Comte-bellott, G. & Corrsin, S. (1966), 'The use of a contraction to improve the isotropy of grid-generated turbulence', *Journal of Fluid Mechanics* **25**(4), 657–682.

Craze, D. (1977), On the near wake behind a circular disc, *in* '6th Australasian Hydraulics and Fluid Mechanics Conference', Adelaide, pp. 282–286.

Crespo, A. & Hernandez, J. (1996), 'Turbulence characteristics in wind-turbine wakes', *Jounal of Wind Engineering and Industrial Aerodynamics* **61**, 71–85.

Croft, N., Lin, B., Williams, A., Mason-Jones, A., Fidler, R., Loman, J., Wooldridge, C., Thomas, S., Cook, A., Gallie, R., ODoherty, T., Willis, M., ODoherty, D., Gao,

G., Ahmadian, R., Muhasilovic, M., Masters, I., Horsfall, I., Cross, M., Falconer, R., Fryett, I. & Evans, P. (2010), 'Tidal turbine deployment in the Bristol Channel: a case study', *Proceedings of the ICE - Energy* **163**(3), 93–105.

Davidson, P. (2004), *Turbulence: An introduction for Scientists and Engineers*, Oxford University Press, Oxford.

de Villiers, E. (2006), The Potential of Large Eddy Simulation for the Modeling of Wall Bounded Flows, Doctor of philosophy, Imperial College of Science, Technology and Medicine.

Espana, G., Aubrun, S., Loyer, S. & Devinant, P. (2012), 'Wind tunnel study of the wake meandering downstream of a modelled wind turbine as an effect of large scale turbulent eddies', *Journal of Wind Engineering and Industrial Aerodynamics* **101**, 24–33.

Fathali, M., Klein, M., Broeckhoven, T., Lacor, C. & Baelmans, M. (2008), 'Generation of turbulent inflow and initial conditions based on multi-correlated random fields', *International Journal for Numerical Methods in Fluids* **57**(October 2007), 93–117.

Grant, H. L., Stewart, R. W. & Moilliet, A. (1961), 'Turbulence spectra from a tidal channel', *Journal of Fluid Mechanics* **12**(02), 241.

Harrison, M. E. (2011), The accuracy of the actuator disc-RANS approach for modelling performance and wake characteristics of a horizontal axis tidal stream turbine, Phd, University of Southampton.

Harrison, M. E., Batten, W. M. J., Myers, L. E. & Bahaj, A. S. (2010), 'A comparison between CFD simulations and experiments for predicting the far wake of horizontal axis tidal turbines', *IET Renewable Power Generation* **4**(6), 566–575.

Hughes, T. J. R., Mazzei, L., Oberai, A. a. & Wray, A. a. (2001), 'The multiscale formulation of large eddy simulation: Decay of homogeneous isotropic turbulence', *Physics of Fluids* **13**(2), 505.

Johnstone, R. & Coleman, G. N. (2012), 'The turbulent Ekman boundary layer over an infinite wind-turbine array', *Journal of Wind Engineering and Industrial Aerodynamics* **100**(1), 46–57.

Jonsson, C., Johnson, P. B. & Eames, I. (2011), Energy Extractors in Turbulent Flow: Wake Decay and Implications for Farm Layout, *in* '9th European Wave and Tidal Energy Conference'.

Kawanisi, K. & Yokosi, S. (1994), 'Mean and turbulence characteristics in a tidal river', *Estuarine, Coastal and Shelf Science* **38**, 447–469.

Knight, M. (1926), 'Wind tunnel standardization disk drag', *N.A.C.A. Technical note* **No. 253**.

Kornev, N., Shchukin, E., Taranov, E., Turnow, J. & Hassel, E. (2009), Development and implemention of inflow generator for LES and DNS applications in OpenFoam, *in* 'Open Source CFD international conference 2009', Barcelona.

Krogstad, P.-A. g. & Eriksen, P. l. E. (2013), 'Blind test? calculations of the performance and wake development for a model wind turbine', *Renewable Energy* **50**, 325–333.

Krogstad, P. & Davidson, P. (2009), 'Is grid turbulence Saffman turbulence?', *Journal of Fluid Mechanics* **642**, 373.

Krogstad, P. & Davidson, P. A. (2011), 'Freely decaying, homogeneous turbulence generated by multi-scale grids', *Journal of Fluid Mechanics* **680**, 417–434.

Lu, Y., Lueck, R. G. & Huang, D. (2000), 'Turbulence Characteristics in a Tidal Channel', *Journal of Physical Oceanography* **30**, 855–867.

MacKay, D. J. (2009), *Sustainable energy without the hot air*, UIT Cambridge Ltd.

Macleod, A. J., Barnes, S. & Rados, K. G. (2002), Wake effects in tidal current turbine farms, *in* 'MAREC conference', Newcastle.

Maganga, F., Germain, G., King, J., Pinon, G. & Rivoalen, E. (2010), 'Experimental characterisation of flow effects on marine current turbine behaviour and on its wake properties', *IET Renewable Power Generation* **4**(6), 498.

Malki, R., Williams, A., Croft, T., Togneri, M. & Masters, I. (2013), 'A coupled blade element momentum computational fluid dynamics model for evaluating tidal stream turbine performance', *Applied Mathematical Modelling* **37**(5), 3006–3020.

Mason-Jones, A., O'Doherty, D., Morris, C. & O'Doherty, T. (2013), 'Influence of a velocity profile & support structure on tidal stream turbine performance', *Renewable Energy* **52**, 23–30.

Massey, B. & Ward-Smith, J. (2006), *Mechanics of Fluids*, eighth edn, Taylor and Francis.

Masters, I., Malki, R., Williams, A. J. & Croft, T. N. (2013), 'The influence of flow acceleration on tidal stream turbine wake dynamics: A numerical study using a coupled BEMCFD model', *Applied Mathematical Modelling* **44**, 0–13.

Milne, I. A., Sharma, R. N., Flay, R. G. J. & Bickerton, S. (2013), 'Characteristics of the turbulence in the flow at a tidal stream power site', *Phil Trans R Soc A* .

Mohamed, M. S. & LaRue, J. C. (1990), 'The decay power law in grid-generated turbulence', *Journal of Fluid Mechanics* **219**, 195–214.

Murzyn, F. & Belorgey, M. (2005), 'Experimental investigation of the grid-generated turbulence features in a free surface flow', *Experimental Thermal and Fluid Science* **29**(8), 925–935.

Mycek, P., Gaurier, B., Germain, G., Pinon, G. & Rivoalen, E. (2013), 'Numerical and Experimental Study of the Interaction between two Marine Current Turbines', *International journal of marine energy* **1**(1), 70–83.

Myers, L. E. & Bahaj, A. S. (2010), 'Experimental analysis of the flow field around horizontal axis tidal turbines by use of scale mesh disk rotor simulators', *Ocean Engineering* **37**(2-3), 218–227.

Myers, L., Shah, K. & Galloway, P. (2013), Design , commissioning and performance of a device to vary the turbulence in a recirculating flume, *in* 'EWTEC', Aalborg, Denmark.

Nezu, I. (2005), 'Open-channel flow turbulence and its research prospects in the 21st Century', *Journal of Hydraulic Engineering* **131**(4), 229–246.

Nishino, T. & Willden, R. H. (2012), 'Effects of 3-D channel blockage and turbulent wake mixing on the limit of power extraction by tidal turbines', *International Journal of Heat and Fluid Flow* **37**, 123–135.

OpenCFD (2012), 'OpenFOAM Foundation'.
URL: *www.openfoam.org*

Pope, S. B. (2000), *Turbulent Flows*, Cambridge University Press.

Reese, H., Kato, C. & Carolus, T. H. (2007), 'Large Eddy Simulation of Acoustical Sources in a Low Pressure Axial-Flow Fan Encountering Highly Turbulent Inflow', *Journal of Fluids Engineering* **129**(3), 263.

Rind, E. & Castro, I. P. (2012), 'On the effects of free-stream turbulence on axisymmetric disc wakes', *Experiments in Fluids* **53**(2), 301–318.

Roos, F. & Willmarth, W. (1971), 'Some experimental results on sphere and disk drag', *AIAA journal* **9.2**, 285–291.

Sanderse, B. (2009), Aerodynamics of wind turbine wakes, Technical report, ECN, E-09-016.

Sanderse, B., van der Pijl, S. P. & Koren, B. (2011), 'Review of computational fluid dynamics for wind turbine wake aerodynamics', *Wind Energy* **14**(February), 799–819.

Schubauer, G. B. & Dryden, H. L. (1935), The effect of turbulence on the drag of flat plates, Technical report, NACA-TR-546.

Sezer-uzol, N. & Long, L. N. (2006), 3-D Time-Accurate CFD Simulations of Wind Turbine Rotor Flow Fields, *in* 'AIAA Aerospace sciences meeting', AIAA Paper 2006-0394, pp. 1–23.

Sforza, P., Sheerin, P. & Smorto, M. (1981), 'Three-dimensional wakes of simulated wind turbines', *AIAA Journal* **19**, 1101–1107.

Sicot, C., Devinant, P., Laverne, T., Loyer, S. & Hureau, J. (2006), 'Experimental study of the effect of turbulence on horizontal axis wind turbine aerodynamics', *Wind Energy* **9**(December 2005), 361–370.

Smirnov, a., Shi, S. & Celik, I. (2001), 'Random Flow Generation Technique for Large Eddy Simulations and Particle-Dynamics Modeling', *Journal of Fluids Engineering* **123**(2), 359.

Sun, X. (2008), Numerical and Experimental Investigation of Tidal Current Energy Extraction, Phd, University of Edinburgh.

Sun, X., Chick, J. & Bryden, I. (2008), 'Laboratory-scale simulation of energy extraction from tidal currents', *Renewable Energy* **33**(6), 1267–1274.

Tabor, G. & Baba-Ahmadi, M. (2010), 'Inlet conditions for large eddy simulation: A review', *Computers & Fluids* **39**(4), 553–567.

Taylor, G. (1963), *The scientific papers of Sir Geoffrey Ingram Taylor, in Batchelor G.K. (ED.)*, Cambridge University Press.

Terracol, M. & Sagaut, P. (2003), 'A multilevel-based dynamic approach for subgrid-scale modeling in large-eddy simulation', *Physics of Fluids* **15**(12), 3671.

Thomson, J., Polagye, B., Durgesh, V. & Richmond, M. C. (2012), 'Measurements of Turbulence at Two Tidal Energy Sites in Puget Sound, WA', *IEEE Journal of Oceanic Engineering* **37**(3), 363–374.

Turnock, S. R., Phillips, A. B., Banks, J. & Nicholls-Lee, R. (2011), 'Modelling tidal current turbine wakes using a coupled RANS-BEMT approach as a tool for analysing power capture of arrays of turbines', *Ocean Engineering* **38**(11-12), 1300–1307.

Vermeer, L., Sø rensen, J. & Crespo, A. (2003), 'Wind turbine wake aerodynamics', *Progress in Aerospace Sciences* **39**(6-7), 467–510.

Versteeg, H. & Malalasekera, W. (1995), *An introduction to computational fluid dynamics*, Longman Scientific & Technical.

Wang, L.-P., Chen, S., Brasseur, J. G. & Wyngaard, J. C. (1996), 'Examination of hypotheses in the Kolmogorov refined turbulence theory through', *Journal of Fluid Mechanics* **309**, 113–156.

Whelan, J. I., Graham, J. M. R. & Peiró, J. (2009), 'A free-surface and blockage correction for tidal turbines', *Journal of Fluid Mechanics* **624**, 281.

Wu, Y.-T. & Porte-Agel, F. (2011), 'Large-Eddy Simulation of Wind-Turbine Wakes: Evaluation of Turbine Parametrisations', *Boundary-Layer Meteorology* **138**(3), 345–366.